# Automatische Bildsegmentierung von gesunden und atelektatischen Lungen in computertomographischen Bildern

Dissertationsschrift

zur Erlangung eines doctor rerum medicinalium (Dr. rer. medic.)

der Medizinischen Fakultät Carl Gustav Carus

der Technischen Universität Dresden

vorgelegt von

Luis Maximiliano Cuevas

geb. am 23. April 1972, Buenos Aires, Argentinien

Dresden 2009

1. Gutachter:   Prof. Dr. rer. nat. Edmund Koch,

2. Gutachter:   PD Dr. rer. nat. et Ing.-habil. Volker Hietschold

Tag der mündlichen Prüfung: 15. Juni 2010

Prof. Dr. rer. nat. habil. Henning Morawietz

Vorsitzender der Promotionskommission

# Selbstständigkeitserklärung

Hiermit erkläre ich, Maximiliano Cuevas, dass ich die von mir am heutigen Tag dem Prüfungsausschuß der Universitätsklinikum der TU Dresden eingereichte Dissertation zum Thema

*Automatische Bildsegmentierung von gesunden und atelektatischen Lungen in computertomographischen Bildern*

vollkommen selbstständig verfasst und keine anderen als die angegebenen Quellen und Hilfsmittel benutzt, sowie Zitate kenntlich gemacht habe.

Dresden, den 17. Dezember 2009

# Contents

# List of Figures

# List of Tables

# Chapter 1

# Introduction

Imaging methods have become an invaluable tool for diagnosis and surgery planning in the field of medicine. In earlier years, the representation of graphical data was restricted to two-dimensional images and only a modest quality because of technical limitations. This scenario, though revolutionary at the time, has been rapidly enhanced owing to the technological evolution. Nowadays, the use of three-dimensional dynamic imaging is common practice, allowing the visualization of entire organs while dynamic processes like blood flow or breathing are observed. In particular, computer tomography (CT) has become a standard in pulmonary imaging which allows the analysis of a range of diseases like lung nodules, emphysema and embolism. However, the improved spatial and temporal resolution involves a dramatic increase in the amount of data that has to be stored and processed. This has motivated the development of computer aided diagnostics (CAD) systems that have released the physician from the tedious task of manually delineating the boundary of the structures of interest from such a large number of images, a pre-processing step known as image segmentation. Apart from being impractical, the manual segmentation is prone to high intra- and inter observer variability. Nonetheless, the automatic segmentation of the lungs affected by atelectasis from volume CT data has not been faced until now. Atelectasis is characterized by the absence of air in the collapsed lung parenchyma, thus resulting in an X-ray absorption similar to that of other anatomical

structures in the thorax. Consequently, the segmentation of the lungs with atelectasis poses a challenge because in CT images they have similar texture and gray level as the surrounding tissue and therefore the available graphical information is not sufficient to distinguish the boundary of the lung.

Research studies which aim to explain the distribution of ventilation and alveolar recruitment in the atelectatic lung in order to improve mechanical ventilation strategies heavily rely on the analysis of large number of volume CT data which assure the statistical significance of the results. The latter can be only guaranteed by a tool that automatically segments the lung with atelectasis free from intra- and inter observer subjectiveness, which are known to be associated with manual measurements.

The present work aims to close the existing gap left by the segmentation of atelectatic lungs in volume CT data. A-priori knowledge of anatomical information plays a key role in the achievement of this goal.

## 1.1 State-of-the-art and review of related literature

The design of algorithms for image reconstruction, processing and segmentation is a topic of intense research that has shown an outstanding growth in the last time. Such evolution have been accompanied by the development of computer-aided diagnosis (CAD) systems that emerged as a set of tools for clinical decision making in various fields of medicine. CAD systems related to chest computed tomography offer the automated detection of pulmonary nodules, diagnosis of pulmonary embolism and quantification of emphysema and interstitial lung disease [1, 2, 3, 4, 5, 6, 7, 8, 9, 10, 11, 12, 13]. An algorithm common to all of these tools is the segmentation of the lung [14, 15, 16, 17] followed by dedicated procedures for the identification and classification of intrapulmonary anatomical structures.

However, the high accuracy demanded in clinical diagnostic is only possible with high definition imaging methods where partial-volume effects are minimized. For that reason, high resolution thin-slice CT is nowadays the

preferred standard for optimal performance of CAD systems [6]. A study that compared CAD and experts' performances using 0.75 mm, 2 mm and 4 mm slice thickness, showed that experts outperformed CAD using 4 mm sections, had comparable performance at 2 mm and was inferior at 0.75 mm [4]. This trend of gaining accuracy and reliability by means of improved image definition instead of more complex segmentation algorithms is confirmed by a number of works driven by the desire for automatic recognition and evaluation of pulmonary diseases beyond the performance of the experienced physician [6, 18, 14, 19, 5]. The importance of good quality images is also evidenced in a recent study on lung parenchyma segmentation based on material decomposition [20]. There, the high contrast obtained with this technique is responsible for the accurate and easy delineation of the healthy lung boundary hereby reducing the complexity of the algorithms to simple thresholding and region growing methods.

With regard to thoracic CT, CAD systems are mainly used for detection and characterization of pulmonary nodules [21, 22, 4, 23, 19]. Such systems are able to identify small lesions, measure their diameters, recognize early malignomas and give more precise estimates on chemotherapy response than radiologists alone can do. Nevertheless, current schemes for nodule detection report many false positives and their performance needs to be further improved [24]. Potential limitations of CAD systems include those patients with diffuse interstitial lung disease, pleura effusion and atelectasis for which the nodule detection may either be impaired or not feasible at all [6]. A detailed evaluation of computer aided detection and automated CT volumetry of pulmonary nodes is presented in [6, 18]. The segmentation algorithms mostly used in these systems are conventional thresholding and region growing assisted, in some cases, by *a-priori* information of the size, shape, position and density of tumors in order to reduce the error rate.

Another group of works concentrates on the identification of emphysema [10, 11, 12, 25] and bronchi abnormalities [26] for which a precise segmentation of the airways [27, 28, 29] is necessary. Since the diameter of small bronchi is below the sub-millimeter resolution of modern CT scanners, the beam collimation and slice thickness directly defines how deep the bronchial

tree can be segmented. Besides primitive semi-automatic segmentation methods [30] that prompt the user to set a seed that initiates a region growing, more complex strategies have been proposed. In [11], the seed is automatically placed by identifying the trachea according to its geometrical characteristics and a special region growing algorithm enlarges the bronchial tree by analyzing its cross-sectional image in each plane and verifying the presence of the airway wall. A similar approach is presented in [26] which introduces the edge-radius-symmetry (ERS) transform. This method exploits the known elliptic like symmetry of the airways in a cross-sectional image to score the voxels with additional information other than their gray level only. A rule-based detection of the airways is presented in [31] which considers the size, gray level and pairwise appearance of vessels and airways. This approach has been optimized in [32] where the bronchovascular pairs are identified with relational learning by extending the analyzed parameters to circularity, area ratio between airway and vessel, adjacency between them and proximity to hilum. None of the mentioned methods can be applied without severe modifications when the airway wall and/or adjacent vessels cannot be distinguished from the atelectatic lung tissue. Moreover, the good performance of such CAD systems heavily relies on thin-slice CT images.

Diaphragm segmentation using a 3D Active Appearance Model (AAM) [33] has been introduced in [34]. There, with the help of a training set, a "general" upper layer of the diaphragm is generated, which is adjusted to the specific individual being analyzed according to some characteristics derived automatically from it. However, this is only possible for healthy lungs.

The works cited so far heavily rely on high definition images where the anatomical structures can be easily distinguished from each other and diseases are clearly identifiable based on the gray level of the voxels. In the presence of atelectasis the situation changes and the introduction of anatomical knowledge is necessary to assist the algorithms to overcome the missing graphical information.

A small number of knowledge-based approaches is reported in the literature for the segmentation of the lung. Preliminary studies introduced in [35, 36, 37, 38] aimed to recognize thoracic anatomical structures have been

further refined to meet more specific applications like lung lobe [39] and airways [40] segmentation. These works use explicit anatomical knowledge such as the expected size, shape, and relative positions of objects to guide different algorithms in order to achieve better discrimination between objects of similar attenuation but none of them is in a position of "reconstructing" large indistinguishable boundaries of an anatomical structure. This difficulty has been recognized by Kauczor et.al. in [41]. There, the segmentation of the atelectatic lung is limited to a single transversal slice taken specifically from the region of the heart. The ribs, vertebrae, heart and sternum are used to estimate the boundary of the partially visible lung parenchyma in the dorsal zone. Consequently, non lung tissue like airways and vessels are wrongly included in the segmentation. Based on the mentioned concept and being aware of its shortcomings, a new approach is developed in the present thesis capable of segmenting the whole lung with atelectasis, which excludes the large airways and the aorta from the intrapulmonary volume. This tool is capable of a reliable operation with 5 mm slice thickness, contrary to the requirements of most modern CAD systems optimized for thin-slice CT images.

Since the development of segmentation, classification and registration algorithms itself is not the goal of this work but merely the means to achieve a robust segmentation of the lung, the review of these algorithms is limited to those that have found application in thoracic imaging and will be presented in chapter 3.

## 1.2   Aims of this work

The overall objective pursued in this thesis is to develop a method capable of performing a reliable and robust segmentation of the lung affected by atelectasis.

Since this work is the result of the close cooperation with a research group for mechanical ventilation, the segmentation algorithms were optimized for the CT data gained during the experiments performed which is characterized

by images intensely affected by partial volume effects[1] and artifacts due to probes, tubes and electrodes. Bearing this in mind, the following goals and requirements are distinguished:

- The segmentation algorithms should work both on 1 mm and 5 mm slice thickness CT images.

- The segmentation algorithm should be robust against artifacts due to probes, tubes and electrodes.

- An accurate segmentation should be guaranteed for different PEEP levels.

- Anatomical information should support the segmentation algorithms to identify the non-distinguishable boundary between the collapsed lung and surrounding anatomical structures in the CT image.

- If the existing algorithms are not suitable for dealing with the large variability observed in the shape of the lung due to different degrees of induced atelectasis and PEEP levels, new algorithms need to be designed in order to use the anatomical information previously learned.

- The software should be able to work on different animals that show large dissimilarities. This should be achieved with the adaption of a reduced set of parameters isolated from the algorithms' code.

## 1.3    Chapter overview

Chapter 2 presents the thoracic anatomical structures that will be analyzed throughout this thesis and briefly introduces how they are used and combined to produce the segmentation of the whole lung. A comparison between anatomical atlas images and the corresponding multiplanar reconstruction of volume CT data evidences the difficulty in identifying organs and structures

---

[1]Partial volume effects are observed when multiple tissues contribute to a single pixel or voxel resulting in a blurring of intensity across boundaries.

in the CT cross-sectional images. In addition, the chapter discusses which planes are best suited for the segmentation of each particular structure and the problems that arise in the presence of atelectasis.

The first part of chapter 3 reviews established registration, segmentation and classifications algorithms that have been selected according to the anatomical structure and the characteristics of the image they will work on. In the second part, the novel algorithms designed specifically for this work in order to overcome the difficulties imposed by a high degree of atelectasis are introduced. All algorithms presented in this chapter are building blocks of more complex segmentation procedures described in chapter 4.

Chapter 4 combines a detailed explanation of the segmentation algorithms and the anatomical considerations they rely on for the segmentation of the structures presented in chapter 2. The chapter concludes with the segmentation of the lung from volume CT data.

In chapter 5, a detailed evaluation of the various components of the overall segmentation algorithm is reported. In this chapter, after a brief introduction to well established evaluation methods for segmentation algorithms, others are proposed to yield more insight in the deviation observed between manual and automatic assessment of the lung boundary. Additionally, the impact of errors in the physiological measurements derived from the automatic segmentation has been analyzed, which is of paramount importance for the practical medical use of the algorithm.

Finally, chapter 6 outlines the goals achieved in this thesis and analyzes the optimization potential for further work.

# Chapter 2

# Anatomical considerations

In this chapter, a general overview of the pig thoracic anatomy relevant for this thesis will be presented. More specific topics related to the anatomical structures analyzed by the segmentation algorithms are treated individually in each section of chapter 4 as they are required.

Anatomical knowledge is a key issue in the lung segmentation approach proposed in this work. Information about the position and shape of organs and bones, together with the observed deviation from their characteristical values is indispensable for selecting those anatomical structures that are adequate to derive landmarks and surfaces that delimit the lung. Moreover, some entities that show an important inter and intra individual variability in the cross-sectional image of a certain plane present a moderate deviation from a typical shape in a different sectional plane. These anatomical considerations will be incorporated in the segmentation procedure to reduce the complexity of the algorithms and tune them to the specific anatomical structure they analyze, hence reducing processing time and improving segmentation accuracy.

Since pigs are not a commonly studied species, detailed information of their anatomy is not available. Consequently, most of the information presented in this chapter is limited to a number of measurements and observations performed by the author on a reduced training set of animals (appendix B) and should not be considered a gold standard.
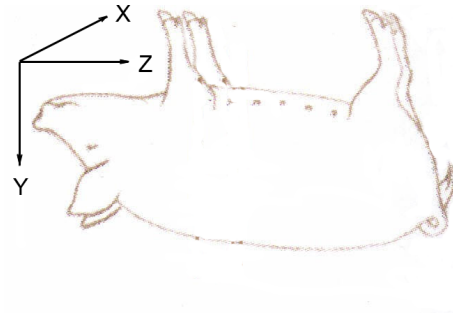
Figure 2.1: Coordinate system adopted throughout this thesis.

Figure 2.1 shows the coordinate system adopted throughout this thesis. Since during the CT sessions the pig lay in supine position, the spine appears at the bottom of the transversal plane image, the right lung on the left side of the image and the left lung on the right.

Figures 2.2, 2.3 and 2.4 show the cross-sectional images of the thorax of a pig. As can be observed, an exact identification of all anatomical structures in the CT image is not feasible. However, healthy lung parenchyma is easily distinguishable from the surrounding tissue due to the high proportion of air it contains. The situation changes completely in the presence of atelectasis. There, gray level and texture of the collapsed lung are very similar to that of the tissue that surrounds it.

## 2.1   Lungs

The lungs are contained in the thoracic cavity together with the bronchi, part of the esophagus and trachea, the major vessels, and the heart. Strictly speaking, the lung parenchyma is made of alveoli wrapped in a mesh of capillaries covering circa 70% of their area. The lung parenchyma is protected by the ribcage which together with the diaphragm and heart defines the border of the lungs.

<table>
<tr><td>(a)</td><td>(b)</td></tr>
</table>
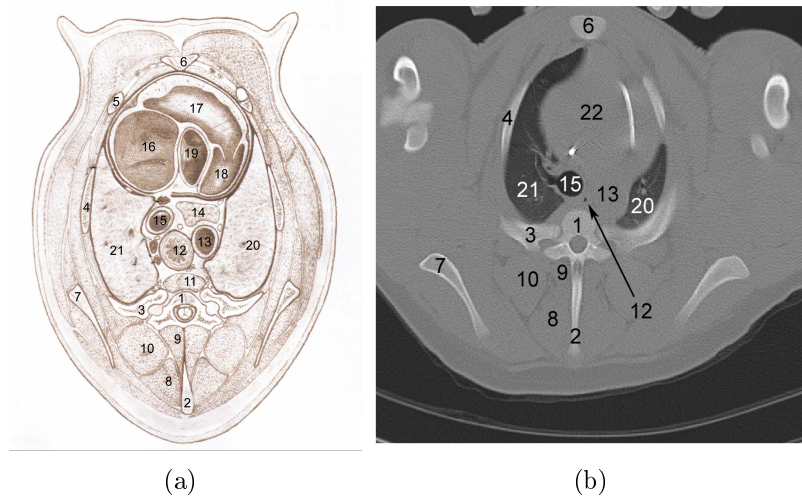
Figure 2.2: Transversal section of a pig. (a) Anatomical atlas (modified after [42]) . (b) CT image. 1 IV Vertebrae thoracicae (thoracic vertebra); 2 Processus spinalis (spinal process); 3-5 Costa (rib); 6 Sternum (sternum); 7 Scapula (scapula); 8 M. spinalis thoracis (spinal-thoracic muscle); 9 Mm multifidi thoracis (multifidus thoracic muscle); 10 M. longissimus thoracis (longissimus thoracic muscle); 11 M. longus colli (longus thoracic muscle); 12 Oesophagus (esophagus); 13 Arcus aorticus (aortic arch); 14 Thymus (thymus); 15 Trachea (trachea); 16 Auriculus dexter (right auricle); 17 Ventriculus dexter (right ventricle); 18 Truncus pulmonalis (pulmonary trunc); 19 Arcus aorticus (aortic arch); 20 Pulmo sinister (left lung); 21 Pulmo dexter (right lung); 22 Car (heart).
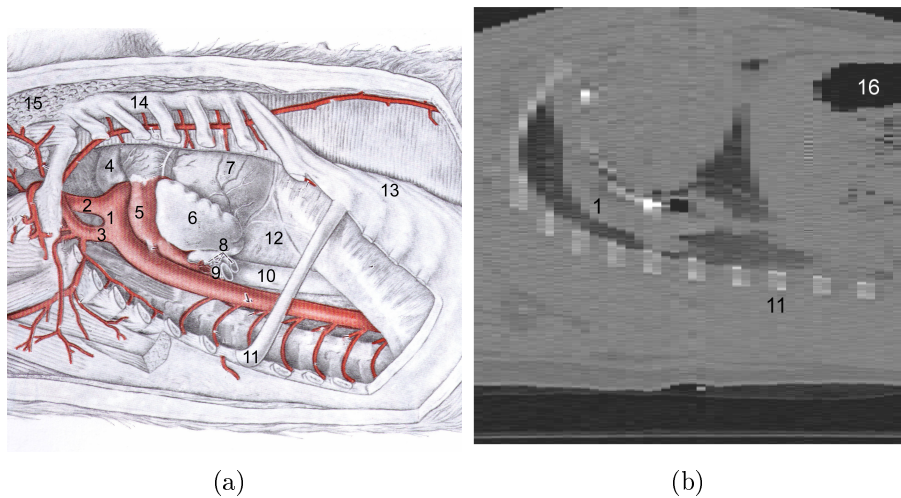
Figure 2.3: Sagital section of a pig. (a) Anatomical atlas (modified after [43]).
(b) CT image (5 mm slice thickness). 1 Arcus aortae (aortic arch); 2 Truncus brachiocephalicus (branchiocephalic trunc); 3 Arteria subclavia sinistra (left subclavian artery); 4 Auricula cordis dextra (right auricle); 5 Truncus pulmonalis (pulmonary trunc); 6 Auricula cordis sinistra (left auricle); 7 Ventriculus cordis sinister (left ventricle); 8 Vv. pulmonales (pulmonary vein); 9 Bronchus principalis (principal bronchus); 10 Oesophagus (esophagus); 11 Costa (rib); 12 Mediastinum (mediastinum); 13 Arcus costalis (costal arch); 14 Sternum (sternum); 15 Mm. pectorales (pectoral muscles); 16 stomachus (stomach).

(a)                                              (b)
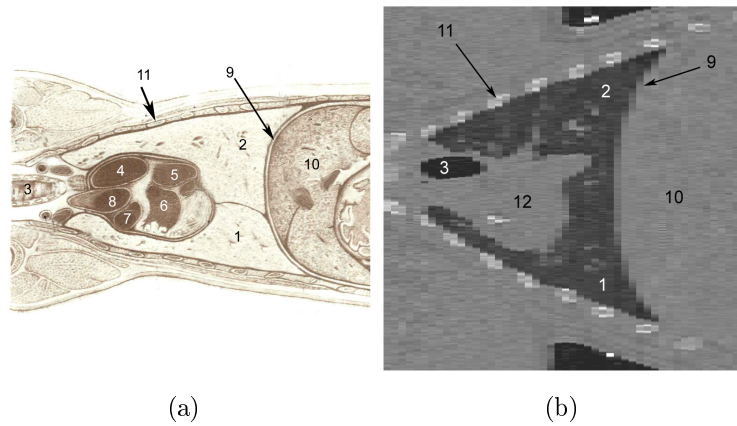
Figure 2.4: Coronal section of a pig. (a) Anatomical atlas (modified after
[42]). (b) CT image (5 mm slice thickness). 1 Pulmo dexter; 2 Pulmo sinister;
3 Trachea; 4 V. cava cranialis (superior vena cava); 5 V. cava caudalis (inferor
vena cava); 6 Auriculus dexter (right auricle); 7 Truncus pulmonalis (pul-
monary trunc); 8 Arcus aorticus (aortic arch); 9 Diaphragma (diaphragm);
10 Hepar (liver); 11 Costa (rib); 12 Car (heart).



(a)                         (b)                         (c)
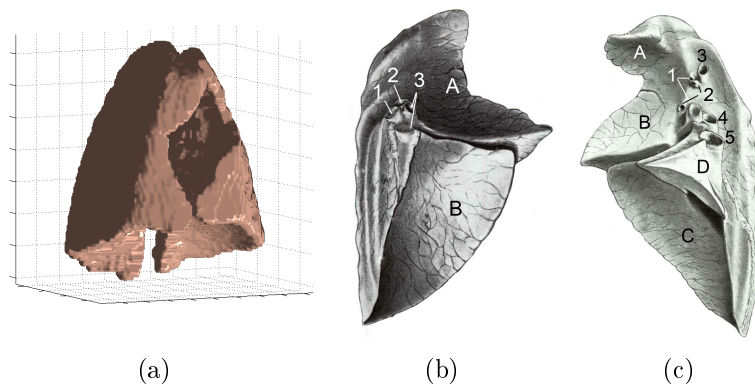
Figure 2.5: Lung examples. (a) 3D reconstruction of the lung of a pig gener-
ated by the segmentation tool presented in chapter 4. (b) Left lung of a pig
(modified after [44]). A Lobus cranealis (superior lobe); B Lobus caudalis (in-
ferior lobe); 1 Bronchus principalis sinister (left principal bronchus); 2 Arteria
pulmonaris (pulmonary artery); 3 Venis pulmonaris (pulmonary vein). (c)
Right lung of a pig (modified after [44]). A Lobus cranealis (superior lobe); B
Lobus medius (middle lobe); C Lobus caudalis (inferior lobe); D Lobus acces-
soriuss (accessory lobe); 1 Arteria pulmonaris (pulmonary artery); 2 Venis
pulmonaris (pulmonary vein); 3 Bronchus trachealis (bronchus trachealis);
4 Bronchus principalis dextra (principal right bronchus); 5 Vena plmonaris
(pulmonary vein).

Airways and vessels that "penetrate" the lung are anatomical structures that are clearly distinguishable from the lung tissue. However, the size of the bronchi above the $16^{th}$ generation and the adjacent vessels become smaller than the resolution of the CT scanner, with its identification being no longer possible. Consequently, lung parenchyma will be referred to as that complex of alveoli, capillaries, small vessels and airways that show as a homogeneous structure in the CT image.

The healthy lung parenchyma is recognizable in the CT image as a homogeneous dark surface, the CT number of which varies typically between -200 and -500 HU [25] depending on the air contents. In the presence of atelectasis, deviations of these values are observed in the collapsed lung tissue due to the lower air contents. There, the lung may present CT numbers as high as 300 HU which do not differ from the surrounding soft tissue.

The shape of the lung is prone to large inter individual variability. Moreover, the lung of an individual changes considerably its size during the breathing cycle and with the PEEP level when the lung is subject to mechanical ventilation. An example of the large variability observed in the animals of the training set is presented in figure 2.6. There, the dependency of the lung size with the pressure is illustrated by means of the distance between landmarks placed on the top of the lung (G), on the top of the diaphragm dome (E) and on the bottom of the lung (L).



(a)          (b)
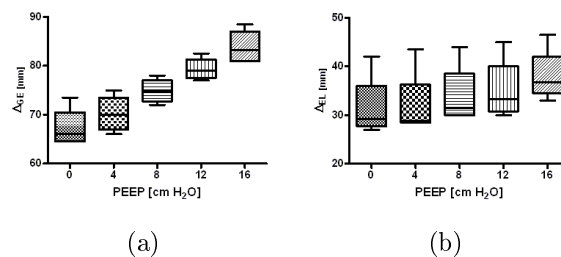
Figure 2.6: Geometrical relationships between lung landmarks for increasing PEEP level measured by end-expiration. (a) Distance between the uppermost (cranial) points of the lung $G$ and diaphragm $E$. (b) Distance between $E$ and the lowest point of the lung $L$.

## 2.2 Ribcage

As observed in figures 2.2, 2.3 and 2.4, the ribs delimit the lung in the dorsal region. In this zone, the ribs are separated from the lung parenchyma through the pleura, a thin membrane that is hardly resolved by the CT scanner. As will be shown in section 4.5, the points where the ribs are in contact with the pleura provide landmarks that define unambiguously the dorsal surface of the lung.

Two additional properties of the ribs make them specially attractive for delimiting the lung. Their CT number, above 150 HU, is higher than that of the soft tissue of all other anatomical structures, including atelectatic lung parenchyma, thus allowing a reliable identification and segmentation of these bones independently of the atelectatis level. The second property is related to the breathing. During the tidal cycle, the ribcage expands and contracts thus contributing to the breathing carried out mainly by the diaphragm. This movement is imposed on the lungs, consequently, although no rigid union exists between lung and ribs[1], the distance between them remains unaltered during the tidal cycle.

The cross-sectional image of the ribs in the transversal plane shows remarkable differences regarding their shape and position. As can be observed in figure 2.2, the ribs near the vertebrae are dissimilar to the ribs near the sternum. Their location depends on the position of the transversal frame analyzed, thus, a rib that is next to the spine "moves" towards the sternum as the considered transversal frame descends from cranial to basal zone. Conversely, in the sagittal plane (figure 2.3), most of the ribs lay approximately on the same line and their shape resembles an ellipse[2]. These properties are preserved throughout all sagittal planes of an animal except in the region of the costo-vertebral articulation. Moreover, inter individual variability presents

---

[1]The parietal pleura (attached to the chest wall) is separated from the visceral pleura (which cover the lung, blood vessels, bronchi and nerves) by a pleural fluid that lubricates both surfaces allowing the two layers to slide against each other while breathing. However, the capillar gap built by the pleural fluid avoids that both layers can be detached due to external forces.

[2]Due to the low resolution of the CT slices shown in figure 2.3, this anatomical characteristic is not clearly observable.

minimal deviation of the mentioned characteristics from their typical values. Hence, the sagittal cross-sectional image of the ribs will be selected for their segmentation (section 4.5.1).

## 2.3   Airways

The respiratory tract begins below the larynx with the trachea, the largest airway. The trachea branches into the right and left bronchi which lead to the two lungs. The bronchi branch many times into smaller airways, ending in the bronchioles, with a diameter of approximately 0.5 mm. The bifurcation of the trachea into the bronchi is known as carina. This point is specially attractive as a landmark due to its easy identification. Observed in successive frames of the transversal plane, the shape of the trachea evolves from a circle into an ellipse which finally divides into two circles[3] (the bronchi) that veer away from the center in the left and right directions. This characteristic is minimally affected by inter individual variability. Furthermore, this distinctive geometry of the airways in the vicinity of the carina is also observed in many other species [44]. Bearing in mind these features, the carina will define a coordinate system which the position of most anatomical structures involved in the lung segmentation will be referred to.

The bronchial tree of the pig slightly differs from that of the human. It presents a ramification on the right side of the trachea, the bronchus trachealis, that leads to the superior lobe (lobus cranealis) of the right lung, as illustrated in figure 2.7.

The large airways are held open during breathing by rings of cartilage which are reliably identifyable in the CT image. This semi-flexible soft tissue possesses a characteristical CT number that distinguishes the wall of the airways from both the air in its interior as well as the surrounding healthy lung parenchyma. Based on this property, it is feasible to segment the bronchi in thin-slice CT images [10, 27]. However, when the lung is collapsed, the situation changes. Since lung tissue affected by atelectasis presents a similar

---

[3]With this description it is suggested that the shape of the trachea and bronchi cross-sectional image resembles a circle or an ellipse.
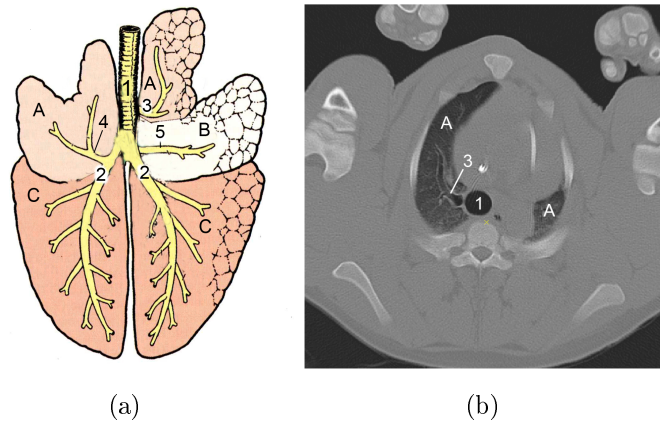
Figure 2.7: Pig airways. (a) Anatomical atlas (modified after [44]). (b) Detail of the bronchus trachealis. A Lobus cranialis (superior lobe); B Lobus medius (middle lobe); C Lobus caudalis (inferior lobe); 1 Trachea (trachea); 2 Bronchus principalis (principal pronchus); 3 Bronchus trachealis (bronchus trachealis); 4 Bronchus lobaris cranialis (superior lobe bronchus); 5 Bronchus lobaris medius (middle lobe bronchus).

gray level to the wall of the airways, the segmentation algorithm must rely entirely on the degree of darkness of the pixels in the interior of the airways, a feature that is independent of the degree of the disease. The CT number inside the airways is lower than -900 HU, the lowest observable in the thoracic CT in normal conditions. However, if the lung is subject to mechanical ventilation, high pressure may produce regions with a CT number even as low as -1000 HU in the hyper-ventilated zones. Taking this into account, the identification and segmentation of the airways needs to be supported by a shape analysis in order to distinguish between hyper-ventilated lung parenchyma and bronchial tree. As mentioned before, the upper airways can be represented accurately with a circle or ellipse in the transversal plane, therefore, this sectional image will be selected for the identification of the trachea and carina and for the segmentation of the principal bronchi.

## 2.4 Diaphragm

The thoracic diaphragm separates the thoracic, or chest cavity, from the abdominal cavity. This muscle is attached to the sternum, the lumbar vertebrae, and the lower ribs. Three openings in the diaphragm allow passage of the aorta, esophagus, nerves, veins and the lymphatic and thoracic ducts.

During breathing, the diaphragm keeps in close contact with the base of the lung. Therefore, the upper surface of the diaphragm provides excellent landmarks for the segmentation of the base of the lung during the whole tidal cycle. In healthy conditions, due to the high contrast between the lung tissue and the diaphragm, the border between them is clearly visible in the CT image. Indeed, in this case, the base of the lungs can be accurately segmented analyzing the gray level of the lung itself without participation of the diaphragm. This property does not hold in the case of atelectatic lungs. There, the CT number of the diaphragm, circa 100 HU, is similar to that of the collapsed lung tissue. Nonetheless, in this situation, a model of the diaphragm dome will provide the mentioned landmarks in order to define the base of the lung (section 4.6).

Figure 2.8 shows the lung and diaphragm, among other anatomical structures, under the effect of different PEEP levels. There, it can be observed that the sagittal plane is suitable to estimate the junction between the base of the lung and the diaphragm. In this plane, the border between the muscle and the lung, always visible in the ventral zone, can be extrapolated, with help of a model, towards the dorsal zone where this edge becomes invisible due to atelectasis.

The transversal section of the diaphragm shows large variability with the pressure and with the position of the transversal plane considered, making it difficult to establish a general model that describes accurately the mentioned edge in all trasnversal slices.

In the dorsal region, the lung is completely collapsed and the atelectatic tissue cannot be distinguished from the diaphragm. Consequently the images of the coronal plane near the vertebral column do not provide any graphical information at all.

(a)　　　　　　　　(b)　　　　　　　　(c)

(d)　　　　　　　　(e)　　　　　　　　(f)
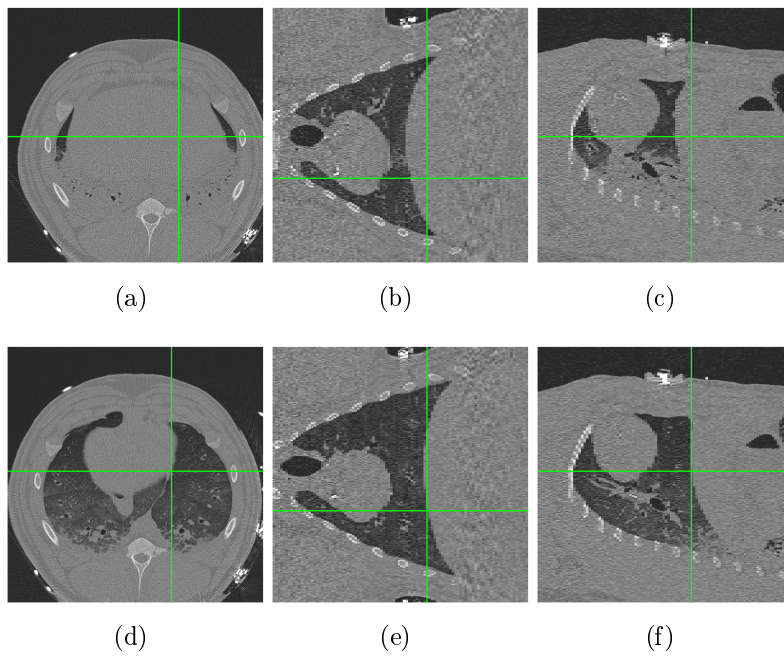
Figure 2.8: Effect of the lung pressure on the diaphragm shape. The top row illustrates from left to right the transversal, coronal and sagittal planes for 0 cm $H_2O$. Bottom: idem for 12 cm $H_2O$.

## 2.5   Vessels

Veins and arteries present an important anatomical characteristic in the cross-sectional image normal to their symmetry axis, namely, they resemble a quasi perfect circle. Since in the thorax the largest vessels descend from the heart in careneo-caudal direction, this characteristic is observed in the transversal plane. However, this property is not sufficient for their identification considering that the vessels filled with blood have the same gray level in the CT image as the soft tissue of the diaphragm, heart and atelectatic lung by which they are surrounded. Additional anatomical properties introduced below and treated more intensively in section 4.7, relate the position of the aorta to the vertebrae and ribs, thus providing more information which allow its segmentation even in an atelectatic lung.

### Thoracic aorta

The thoracic aorta of the pigs runs parallel to the backbone describing a sinusoidal movement around it. In the cranial region it lies to the left of the vertebral column, as it descends it approaches the median line, passes in front of the spine, continues to the right and at its termination tends to the center again. This characteristical form of the aorta, shown in figure 2.9 has been observed in the pigs of the training set (see appendix B.1) and differs slightly from the human aorta anatomy [45]. The diameter of the aorta remains nearly constant along all transversal frames of the thorax and its diameter can be derived from that of the trachea with an error smaller than 5 mm (figure 2.10).
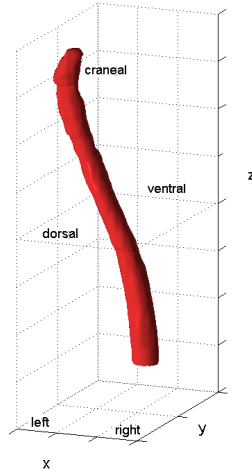
Figure 2.9: Example of 3D reconstruction of the thoracic aorta.
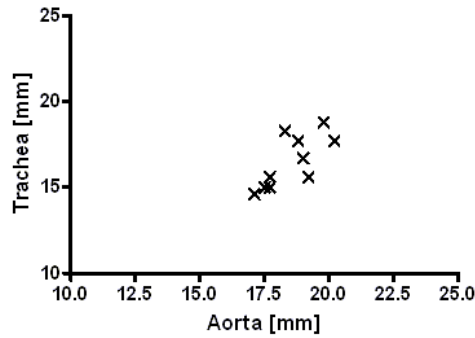


Figure 2.10: Comparisson between the aorta and trachea diameter (based on the training set B.1).

## Vena cava and vessels adjacent to bronchi

As shown in figure 2.11, adjacent to each bronchus runs an artery and a vein [26, 32]. They are arranged in a typical pattern where the centers of the vein, bronchus and artery are aligned with the bronchus always in the middle. Although this informal anatomical observation has not been used in the present work for the segmentation of such vessels, it is one of the building sites that remain open for the optimization of the segmentation algorithm.

(a)             (b)
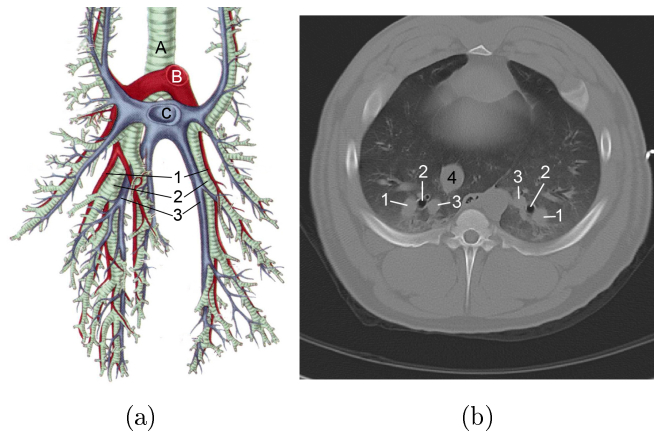
Figure 2.11: Pulmonary vessels adjacent to the bronchi. (a) atlas image (after [44]). (b) CT image. A Trachea (trachea); B Truncus pulmonaris (pulmonary trunk); C Venis pulmonaris (pulmonary veins); 1 Arteria (artery); 2 Bronchus (bronchus); 3 Vena (vein); 4 Vena Cava (vena cava).

The vena cava (figure 2.11 (b)), shows anatomical properties (not formally studied in the present thesis) simmilar to the arteria aorta which may be employed for its segmentation in future works.

# Chapter 3

# Image Analysis and Segmentation

This chapter will introduce the theoretic fundamentals of the algorithms employed in this work for the segmentation of the lung and related anatomical structures. The first part of the chapter briefly describes established methods of image segmentation, classification and registration. The second part, presents a number of algorithm that have been developed and optimized specifically for segmentation of atelectatic lungs.

## 3.1   Segmentation

Image segmentation is defined as the partitioning of an image into non-overlapping regions which are homogeneous with respect to some characteristic such as intensity or texture [46, 47]. Formally, the segmentation can be described as the following mapping

$$Seg : I(X) \rightarrow S(X)$$

that assigns to each pixel with coordinates $X$ of the image $I$ one segment $S_k$ in the set $S$. Thus, satisfying

$$I = \cup S_k \quad with\, 1 < k < K$$

where $S_k \cap S_j = 0$ for $k \neq j$.

This means that, ideally, the segmentation procedure partitions a medical image into its distinct anatomical structures.

A a wide palette of segmentation algorithms has been developed in an effort to improve their performance depending on the requirements of the specific application, imaging modality, etc. Noise, motion and partial volume effects produce imaging artifacts which have a significant impact on the segmentation results. Although researchers look tireless for an ubiquitous segmentation algorithm, there is not a general approach that yields acceptable results for every medical image. Methods that have a more universal character can be applied to a variety of data at the cost of sacrificing quality. Conversely, methods that are specialized to a particular application achieve better results by considering *a-priory* information.

Usually, the dimensionality[1] selected coincides with the dimension of the image domain. However, in order to reduce the memory requirements, computational complexity or to simplify the implementation of the algorithm, 2D methods are applied sequentially to the slices of a volume data. A comparative studio of segmentation algorithms for the segmentation of CT lung images is presented in [48].

### 3.1.1 Thresholding

Thresholding is the separation of objects or regions of an image based on pixel gray levels above or below a threshold value. A mathematical definition of thresholding is given by

$$S_k(X) = \begin{cases} S_o & if \ I(X) > Threshold \\ S_b & if \ I(X) < Threshold \end{cases}$$

where $S_o$ and $S_b$ are the object and background segmentation respectively[2].

---

[1]Dimensionality refers to whether a segmentation algorithm operates in a 2D or 3D image domain.

[2]This definition assumes that the gray level of the object is higher than the selected threshold. The inverse is also valid like in the case of the healthy lung parenchyma which gray level is lower than the background.

The value of the threshold can be automatically determined based on the gray level hystogram of the image, or manually set if previous knowledge of the object and background intensities is available. Thresholding is a classical method to segment an image where different structures have contrasting intensities. This procedure is very sensible to the presence of noise, therefore, it is usually applied after preprocessing the image with a filter. Due to its simplicity, this technique offers low computational time and produce satisfactory results for certain imaging modalities with low noise like computer tomography. This justifies that thresholding shares the scenario of the lung segmentation [22, 41] with other more sophisticated algorithms. Variations on classical thresholding have been proposed for medical image segmentation [49].

### 3.1.2 Region growing

The simplest region-growing algorithm is known as pixel aggregation [50] method. In this approach, regions consist of spatially connected pixels that fall within a specified gray-level deviation from the starting or seed pixel. Beginning with the seed pixel, the *n-connectivity* (see figure 3.1) defines which pixels are analyzed and appended to the region, provided that they meet a certain homogeneity criterion. This process repeats iteratively with the neighbor pixels of each newly incorporated pixel, thus enlarging the region until no more pixels can be grouped.

Based on this concept, the airways (section 4.4), stomach (section 4.8) and ribs (section 4.5.1) will be segmented by analyzing the connectivity of 2D regions, instead of pixels, between adjacent slices.

Region growing algorithm have been successfully used in nodule detection of mammograms [51], [52], thoracic CT Scans [19] and tracheobronchial tree segmentation [29].

Like in thresholding, region growing is also sensitive to noise, causing extracted regions to have holes. Conversely, partial volume effects can cause separate regions to become connected. An extensive and comparative study on seeded region growing can be found in [53].

24

|  |  |  |
|:--:|:--:|:--:|
| (a) | (b) | (c) |
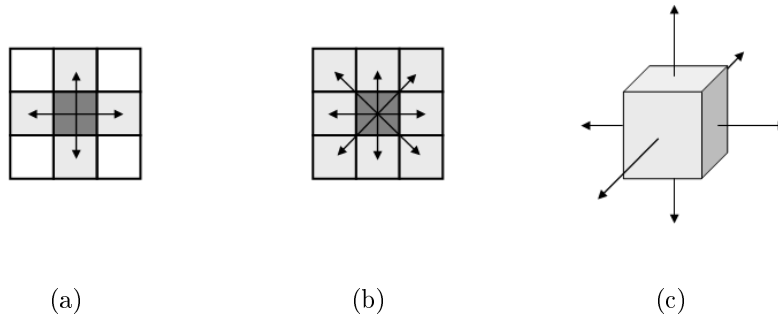
Figure 3.1: Connectivity definition in an image. (a) 4-connected: pixels are connected if their edges touch. (b) 8-connected: pixels are connected if their edges or corners touch. (c) Three-Dimensional Connectivity 6-connected: voxels are connected if their faces touch.

### 3.1.3 Template matching

Template matching identifies in an image those regions that match a template image. The geometry of the object to be segmented must be previously known in order to define a template or convolutional kernel. The simplest approach performs the convolution between image and kernel which shows a maximum where the template best matches the image. Different methods have been developed to reduce the computing time or enhance accuracy like filtering in the frequency domain of the image, working with an image pyramid[3] [54, 55]. More sophisticated algorithms are employed to deal with translation, scale and image rotation problems [56].

In the field of medical image processing, template matching is used for the automated detection of pulmonary nodules [23] or bronchial abnormalities [26], among others [57].

The segmentation of the thoracic aorta in section 4.7 is based on this technique.

---

[3]An image pyramid is obtained by repeatedly filtering and sub-sampling the original image in order to generate a sequence of reduced resolution images

## 3.2 Registration

The object of image registration is to bring one image (*target image*) into alignment with another image (*reference image*) by applying a spatial transformation to the input image. Classical registration methods are limited to the use of linear (also called rigid) transformations, which are a combination of translation, rotation, global scaling and shearing. Linear transformations are global by nature, and thus unable to model local deformations usually observed in biomedical images.

Non-rigid registration, by contrast, is free from the limitations mentioned above and allows elastic deformations. In recent years there has been a growing interest in the field of elastic deformation and a wide variety of different approaches have been developed to accurately describe the deformations required for the registration of biomedical images. Considering that this theme is not the principal concern of the current thesis but useful as a tool for the estimation of the base of the lung (section 4.6), a brief introduction to the most relevant methods will be given.

One strategy consists on modeling anatomical structures by biomechanical models of tissue [58, 59]. They take topological and physical properties of the modeled object into account, and are thus able to predict the deformation according to external forces and boundary conditions. A drawback of this approach is the exact determination of the biomechanical parameters which in turn show important deviations from standard values due to inter and intra individual variability, additionally affected by temperature and age of the individual among others factors [60]. However, recent works have shown a promising future of this concept, steadily increasing the quality of the biological models [61, 62]. The interested reader can consult the following literature for additional information [63, 64, 65].

Another group of non-rigid registration methods are based on anatomical landmarks. Simply speaking, a landmark is a distinctive reference point of an image. Thus, by identifying the landmarks of the source image and their corresponding (homologous) landmarks of the target image it is possible to compute an elastic transformation that puts them in correspondence. Thin-

plate spline (TPS) [66], elastic body spline (EBP) [67] and finite elements [68, 69] are some of the most relevant mathematical bases of interpolation methods.

### Anatomical Atlas

Anatomical atlases are built with a collection of biomedical images which have been segmented and labelled by experts. The standard atlas-guided approach treats segmentation as a registration problem thus finding a one-to-one transformation that maps a pre-segmented atlas image to the target image [70]. This process is often referred to as "atlas warping". Both rigid and non-rigid deformation are used to perform the warping. However, elastic registration is usually preferred for a better match of the anatomical structures. Atlas-guided approaches have been mainly applied in MR brain imaging [71, 72] but they find also their use in the lung lobe segmentation of CT images [17] and segmentation of 3D cardiac MR images [73].

Based on this concept, the base of the lung defined by the junction between diaphragm and ribs, referred to as "lung edge" (LE) (section 4.6.2) has been manually segmented and stored. This simplified atlas will be used to estimate the non visible LE of lungs affected by atelectasis. For that the LE curve taken from the atlas is subject to rigid and elastic transformation to perform a landmark based registration.

## 3.3 Analysis of shape

Since several organs and anatomical structures possess characteristical shapes that, in normal cases, do not deviate much from the average, the analysis of shape provides a strategy to identify and classify them. Moreover, changes of the typical geometry of anatomical structures caused by a disease process can be evaluated to distinguish between malignant and benign conditions [74, 75]. Shapes are defined by contours which are the result of a segmentation operation. However, the analysis of shape seldom operates on the contour

itself. Instead, features are derived from them, called shape factors, which describe different properties of the contours, as will be shown below.

Alternatively, shapes may be described with a binary or bi-level image as well, which implies a considerable increase in the memory requirements.

### 3.3.1 Contours

Contour is defined as the edge or border of a 2D region that results from the segmentation of an image. The simplest representation of a contour is an ordered set of the pixel coordinates along the contour. The dimensionality of a contour can be reduced from 2 to 1 if the distance from each pixel to the contour centroid is stored instead of the absolute $(x,y)$ coordinates. A more efficient representation method is the *chain coding* proposed by Freeman [76] also known as the Freeman chain code. This technique specifies the $(x,y)$ coordinates of a starting point on the contour, the direction of traversal (clockwise or counter-clockwise), and a code to indicate the direction of the movement to reach the next contour point on a discrete grid. Besides an efficient representation, chain code provides advantages with regard to rotation, translation and scaling [77].

Considering the compact representation of contours to define shapes compared to binary images, the anatomical structures segmented in this work are stored as contours. Consequently, most of the algorithms have been designed to operate with contours as well.

### 3.3.2 Shape factors

Shape factors (also known as shape descriptors) summarize properties embedded in a contour using a small number of parameters.

#### Compactness

Compactness is defined as the ratio of the perimeter P and the area A of a contour. It is a measure of the "efficiency" of a contour to contain a given area.

$$Co = \frac{P^2}{A}$$

In order to normalize and restrict the range of this parameter to [0,1], as well as to obtain increasing values with increasing complexity of the shape, this definition is modified as

$$Cf = 1 - \frac{4\pi A}{P^2}$$

The compactness coefficient has been applied to the shape analysis of mammographic calcification [78] and the classification of benign versus malignant breast masses [79].

## Moments

The same concepts used in mathematics to define moments of the probability density function (PDF) have been extended to the analysis of images and contours [80]. Given a M×N digital image I, the regular moments $m_{p,q}$ of order $(p + q)$ are defined as

$$m_{p,q} = \sum_{x=0}^{M-1} \sum_{y=0}^{N-1} (x)^p \cdot (y)^q \cdot I(x,y) \tag{3.1}$$

where x and y are the coordinates of the pixels of I, and I(x,y) their intensity or gray level. If the moments of a contour are computed, only the contour pixels are used with intensity set to 1 and the internal pixels set to 0.

The central moments of an M×N digital image I are defined as

$$\mu_{p,q} = \sum_{x=0}^{M-1} \sum_{y=0}^{N-1} (x - \overline{x})^p \cdot (y - \overline{y})^q \cdot I(x,y) \tag{3.2}$$

where $\overline{x} = \frac{m_{1,0}}{m_{0,0}}$ and $\overline{y} = \frac{m_{0,1}}{m_{0,0}}$

The first order moment $m_{1,1}$ will be used in the segmentation of the thoracic aorta (section 4.7) to estimate the position of its center.

**Ellipse approximation**

The cross-sectional image of some anatomical structures like airways, vessels and even ribs can be accurately described by an ellipse. In order to do so, the center, major and minor radii and rotation are derived from the contour with the help of the principle component analysis (PCA):

First, the center of mass of the object is computed to define the ellipse center. Then the covariance matrix of the contour is built with the coordinates of its points relative to the ellipse center. The major and minor radii are derived from the eigenvalues $\lambda$ as shown in equation 3.3, and the rotation angle is extracted from the eigenvectors. Additionally, the circularity $\eta$ of the ellipse is computed with equation 3.4, with 0 being that of a perfect circle.

$$R_i = \sqrt{2\lambda_i} \tag{3.3}$$

$$\eta = 1 - \sqrt{\frac{\lambda_1}{\lambda_2}} = 1 - \frac{R_1}{R_2} \tag{3.4}$$

In sections 4.5.2 and 4.4, the ellipse approximation of pre-segmented contours plays a main role in the classification and validation of ribs and airways.

## 3.4   Classification

Generally speaking, classification is the process of assigning elements of a set to the class they belong to, according to their features. When working with images, classifiers operate on different entities like pixels (or voxels), contours, 2D regions, or volume data. Consequently the nature of the features evaluated by the classifier depend on the domain of the data to be classified. Classification is a subject of permanent research that covers a wide palette of approaches and fields of application. A comprehensive survey of image classification can be found in [81]. The tool chosen for the classification of contours in the present work are classification trees. Although they do not count among the most used methods, some of their characteristics make them appropriate for the classification of contours as will be explained below.

### 3.4.1 Classification trees

Since classification trees (also known as decision trees) were first introduced by Breiman [82], they have been used in diverse fields like medicine [83, 84, 85], pattern recognition [86] and speech processing [87] among others [88, 89]. They are an attractive alternative to other classification methods like neural networks, when understanding the classification process is more important than the accuracy of the classification itself. Additionally, classification trees can be manually built, thus allowing a specialist to incorporate his/her expertise in the classification process in order to improve results. This issue gains significance when a reduced training set is available.

Basically, classification trees are described by a series of questions assigned to the nodes of a binary tree (figure 3.2). In each node, a single feature (predictor) is evaluated and if the condition is met, the classification process continues one level below with the node reached by the right branch, otherwise node on the left is chosen. This process begins at the root node and descends through the tree until a terminal node is reached, indicating the assigned class.

A detailed explanation of the training algorithm is out of the scope of this thesis, therefore only a brief introduction to the concept will be given.

Like in other supervised training methods, each element of the training set must be labeled with the class it belongs to. The algorithm then systematically tries to split the set into two parts, examining one predictor at a time. The goal is to attain a set of labels as homogeneous as possible in each partition, i.e. the split which maximizes the reduction in impurity is chosen. This process is known as "binary recursive partitioning". Beginning at the root with the whole training set, this splitting or partitioning is then applied to each of the new partitions, thereby growing the tree. The process continues until all terminal nodes are pure or contain no more cases than a specified minimum fraction of the sizes of one or more classes.

A reduced training set, noisy data and outliers in general may result in over-fitting, therefore the tree must be pruned until it reaches its "right" size. Pruning is the process of removing nodes and branches that fail to generalize,
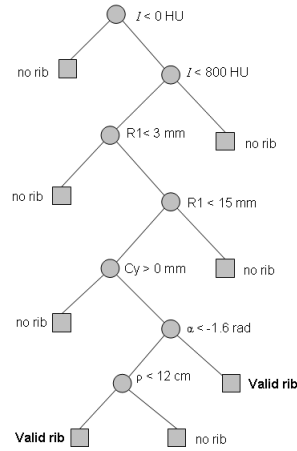
Figure 3.2: Classification tree example used to classify contours into valid ribs and no ribs. The predictors evaluated in each node are I, R1, Cy, $\alpha$ and $\rho$.

thus improving the performance of the decision tree when it is applied to real data. Many approaches have been proposed for pruning like cross-validation and statistical tests. For more information refer to [82].

The penalty for wrong classification can be optionally introduced with a cost matrix C. There, $c(i,j)$ is the cost of classifying an element into class $i$ if its true class is $j$. Consequently C = 0 if i = j.

Classification trees are used in the present work for the classification of contours into such diverse anatomical structures like ribs (section 4.5.2), bronchi, trachea and carina (section 4.4).

## 3.5    Dedicated algorithms

The algorithms described below have been developed specifically to meet the requirements imposed by the segmentation of the lung in the conditions that concern the performed experiments. However, their comprehension is not indispensable to understand the chapter 4 where the segmentation of the lung is introduced. The reader is encouraged to proceed with the next chapter

and consult the algorithms description when necessary. It may facilitate their understanding in the context they are employed.

Although the concepts behind the algorithms are simple and can be explained using simple words, they are formulated with pseudo-code to guarantee an accurate description.

### 3.5.1 Contour Overlap Algorithm

Given two sets of contours referred to as *target* and *seed* set, the *contour overlap* algorithm analyzes the contours belonging to the *target* set and identifies those that overlap with at least $N$ pixels of some contour in the *seed* set.

---
**Algorithm 1** Contour Overlap
---
1: **procedure** CONTOUROVERLAP($Seed, Target, ThreshOvr, Mode$)
2:     **for all** $C_s \in Seed$ **do**
3:         **for all** $C_t \in Target$ **do**
4:             **if** $C_t \in ValidContours$ **then continue**
5:             **end if**
6:             $OverlappingMask \leftarrow$ MASK($C_s$) & MASK($C_t$)
7:             **if** AREA($OverlappingMask$) $> ThreshOvr$ **then**
8:                 $ValidC \leftarrow ValidC \cup Ct$
9:             **end if**
10:         **end for**
11:         **if** $Mode =$Upper **then**
12:             $OverlappingC \leftarrow$ UPPER($ValidC$) $\cup OverlappingC$
13:         **else if** $Mode =$Biggest **then**
14:             $OverlappingC \leftarrow$ BIGGEST($ValidC$) $\cup OverlappingC$
15:         **else if** $Mode =$All **then**
16:             $OverlappingC \leftarrow ValidC \cup OverlappingC$
17:         **end if**
18:     **end for** **return** $OverlappingC$
19: **end procedure**
---

In brief, the for loop starting in line 3 evaluates all contours *Ct* extracted from the set of contours *Target* against each contour *Cs* extracted from the set of contours *Seed* (line 2). In line 6, the function MASK creates a mask from a contour $C$, i.e. it makes a binary image where the pixels inside the

contour are set to 1 and the rest are set to 0. Afterward, a pixel wise
AND operation is performed between the masks of *Ct* and *Cs* to create
*OverlapingMask*. Put simply, a mask is computed with those pixels inside
*Cs* that overlap with the pixels inside *Ct*. If the number of pixels set to 1 in
*OverlapingMask* is higher than *ThreshOvr*, *Ct* is added to the set of validated
contours *ValidC* (lines 7 to 9). Lines 4 and 5 prevent a contour *Ct* that has
been already validated from being analyzed twice. Finally, according to the
mode of operation, the algorithm can select among all *Cts* that overlap a *Cs*:
only one *Ct* (the one with the largest area: lines 13 and 14, or the one which
has the lowest Y coordinate: lines 11 and 12), or all of them (lines 15 and
16). The selected contours join the *OverlappingC* set which is returned as
the output result of the algorithm.

### 3.5.2   Robust Fit Algorithm

The following robust fit algorithm has been designed to fit data with outliers
and is one of the original contributions of this work. Contrary to weighted
robust fit algorithms which ponders each data point according to its distance
to the previous estimation of the fitting curve, the present approach removes
the outliers from the data set to be fitted in order to ignore completely their
influence in the fitting function.

**Algorithm 2** Robust Fit

```
 1: procedure ROBUST FIT(Dataset, Niter, Residual, Model)
 2:     E ← ∞
 3:     Iteration ← 0
 4:     while Iteration < Niter and E > Residual do
 5:         i ← 0
 6:         Error ← ∅
 7:         for all p ∈ Dataset do
 8:             TestSet ← Dataset \ pᵢ
 9:             Fit ← LEASTSQUARESFIT(Model,TestSet)
10:             Errorᵢ ← (Fit − TestSet)²
11:             i ← i + 1
12:         end for
13:         j ← argᵢmin Error(i)
14:         E ← Error(j)
15:         Dataset ← Dataset \ pⱼ
16:         Iteration ← Iteration + 1
17:     end while
18: return Fit
19: end procedure
```

This algorithm is based on the following assumption: Let $D$ be a data set made of $N$ elements, where the $i^{th}$ element is an outlier. Then, there are $N$ subsets $T$ of $D$ built with ($N$-1) elements of $D$, i.e. each subset $T$ excludes an element of $D$ in turn. The fit mean squared error computed by fitting the subset a $Ti$ (the one that excludes the outlier) is the smallest among the errors of all subsets.

This concept can be extended to a set of data with more than one outlier and is implemented in the robust fit algorithm shown above. Input arguments are the $Data$ set to be fitted, a $Model$, the maximum number of iterations $Niter$, and the allowed $Residual$ [4].

During each iteration (lines 4 and 16), one element from the data set $D$ will be removed (line 15): the outlier that has the worst effect on the fit. This outlier is identified in a loop (lines 7 to 12). In each pass of the loop, a test set $T$ is created from $D$ excluding the element $i$ (line 8). Then, a

---

[4]The residual is defined as the mean squared error of the difference between the observed value and the fitted value.

least squares fit algorithm fits *Model* with the elements of $T$ (line 9) and the corresponding fit error is stored (line 10). The loop finishes after all subsets of the current data set $D$ have been explored.

Afterwards, the element $i$ for which the fit error *Error* is minimal is identified (line 13) and removed from $D$ (line 15). At this point one outlier has been identified and removed from the data set that will be processed in the next iteration. The process is repeated until the mean squared error of the difference between observed and fitted data is lower than the allowed *Residual* or until the maximal number of iterations *Niter* have been compleated . Then the remaining elements of $D$ are fitted with the *Model* function and returned.

The complexity of this algorithm, $O(Niter \cdot SIZE(Dataset))$, makes it unsuitable for a large data size. If this is not the case (as in the present study) the data is better fitted with the proposed approach than using other robust algorithms tested so far.

### 3.5.3 Volume Growing Algorithm

Since the volume growing algorithm is the core of both the Bronchial tree tracking and the Stomach segmentation, it will be explained in the context of these applications in order to facilitate its comprehension.

---

**Algorithm 3** Volume Growing

---
 1: **procedure** Volume Growing($CTdata, StartIdx, ROI, StrEl, Thres$)
 2:     $i \leftarrow StartIdx$
 3:     $StartSlice \leftarrow CTdata(i)$
 4:     $StartSliceROI \leftarrow StartSlice \,\&\, ROI$
 5:     $Seed \leftarrow \text{Seg}(StartSliceROI\,,Threshold\,)$
 6:     $n \leftarrow 1$
 7:     **while** $n > 0$ **do**
 8:         $i \leftarrow i - 1$
 9:         $TestSlice \leftarrow \text{Seg}(CTdata(i)\,,Threshold\,)$
10:         $Overlap \leftarrow TestSlice \,\&\, Seed$
11:         $n \leftarrow \text{Area}(Overlap)$
12:         **if** $n > 0$ **then**
13:             $Seed \leftarrow Overlap \oplus StrEl$
14:             $OutVolume(i) \leftarrow Seed$
15:         **end if**
16:     **end while**
17: **return** $(OutVolume, i - 1)$
18: **end procedure**

---

As will be explained in greater detail in section 4.6.2, the goal of the bronchial tree tracking algorithm is the identification of the lowest end (recognizable in the CT image) of the bronchial tree in a lung with atelectasis, or, when the atelectasis is not visible (either because the lung is healthy or due to high PEEP levels) to find the lowest point of the base of the lung.

In brief: the algorithm processes all transversal frames sequentially downwards beginning below the carina. The frames are analyzed pairwise, i.e. the airways of two contiguous frames (the upper and lower frame) are segmented and the connectivity (overlap) of the segments between both frames is used to track the bronchi.

Input arguments are *CTdata*: the 3D CT dataset, *StartIdx*: the index of the transversal frame where the tracking starts, *ROI*: the 2D region of interest (ROI) where the airways are segmented, *StrEl*: the structuring element used for the dilation operation, *Thres*: the threshold level used for the airways segmentation.

Lines 2 to 5 segment[5] in the *StartSlice* the airways (and lung parenchyma) with a gray level below *Thres* inside the *ROI*. The segmented data is called *Seed* (line 5) in analogy to region growing algorithms, as it will be used to analyze the connectivity with the voxels below *Thres* of the next transversal frame (*TestSlice*)(line 9).

It is worth noting that the diameter of the bronchi becomes smaller than 3 pixels (considering the pixel size of $0.5 \times 0.5$ mm) as the transversal plane approaches the base of the lung, and the voxels of those bronchi that do not descend vertically are misaligned between contiguous frames. Therefore, the voxels of the *Seed* do not overlap with the *TestSlice* and the tracking would be broken. To remedy this problem the *Overlap* area is enlarged by performing a dilation of their segments with the structuring element *StrEl*. As a consequence, the voxels of the enlarged *Overlap* are connected with the voxels of the *TestSlice*, assuring the further tracking of those bronchi that descend obliquely. The last takes place in line 10, where the overlap between the voxels of the *TestSlice* with the *Seed* is computed. If the area resulting from the overlap is at least one voxel, the *TestSlice* is used as *Seed* (lines 11 to 14) for the next iteration, and stored in the resulting segmentation volume. This procedure is repeated (lines 7 and 16) until no connection between the voxels of *Seed* and *TestSlice* is verified (line 7). Finally, the segmented volume and the last frame where the presence of the airways (or lung parenchyma) was observed is returned (line 16).

The value assigned to the mentioned parameters for the bronchial tree tracking are specified in appendix A.2.

The behavior of the algorithm when used to segment the dark regions of the stomach (section 4.8) remains the same as to the following points:

- the transversal frames are analyzed upwards beginning at the lowest frame where the stomach has been detected.

- ROI, threshold, and structuring element are set according to the requirements of the stomach segmentation as detailed in appendix A.3.

---

[5]The segmentation is performed by a simple threshold based algorithm referred to as SEG.

### 3.5.4 Modify Contour Algorithm

This algorithm modifies a contour by replacing the portion comprised between two points, $j$ and $k$, by a curve. The points $j$ and $k$ are the nearest points of the contour to $p1$ and $p2$, the start and end points of the curve respectively. The mode of operation (upper/lower) decides whether the upper or the lower portion of the contour is kept. A graphical example of the *ModifyContour* algorithm applied to the contour of a lung affected by atelectasis is shown in figure 3.3.
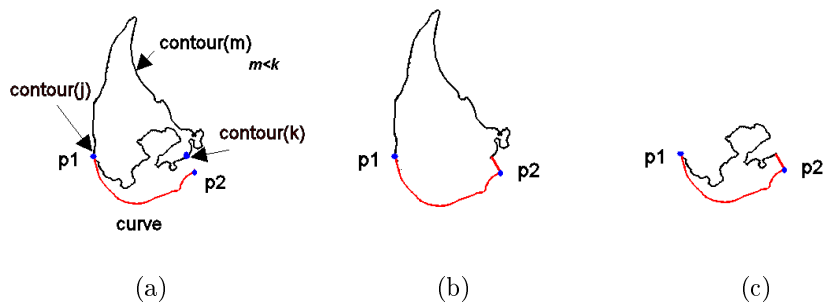


Figure 3.3: ModifyContour examples. (a) lung contour affected by atelectasis and bones profile curve. p1 and p2 are the start and end points of the curve. (b,c) Resulting contour after having modified the lung contour with the curve under the (b) upper mode and (c) lower mode operation.

The input arguments of the algorithm are a contour (*Contour*), a curve (*Curve*) and the mode of operation (*mode*). The *Contour* is defined as an ordered set of points the first element *Contour(0)* of which is the uppermost point of the contour and its sense of circulation is defined to be clockwise. The *Curve* is also defined as an ordered set of points where $p1$ is the starting point of the curve, on the left of the end point $p2$. Lines 2 and 3 store the corresponding coordinates of the contour points in $x$ and $y$. The number of elements of the *Curve* is stored in $n$ by means of the function LENGTH (line 4). The distances from each point of the contour to $p1$ and $d2$ are computed in the for loop in the lines 7 to 10 and stored in $d1$ and $d2$ respectively. Line 11 identifies the position ($j$) of that point of the *Contour* which lies nearest

to *p1*. This is done by looking for the index (argument) of the element that minimizes the distance *d1*. The same applies to *k*, in line 12, considering the distances *d2* of each point of the contour relative to the end of the curve *p2*.

---

**Algorithm 4** Modify Contour

---

1: **procedure** ModifyContour(*Contour*, *Curve*, mode)
2:     $x \leftarrow Contour_x$
3:     $y \leftarrow Contour_y$
4:     $n \leftarrow$ Length(*Curve*)
5:     $p1 \leftarrow Curve(0)$
6:     $p2 \leftarrow Curve(n)$
7:     **for** $i \leftarrow 0, n$ **do**
8:         $d1(i) \leftarrow (x(i) - p1_x)^2 + (y(i) - p1_y)^2$
9:         $d2(i) \leftarrow (x(i) - p2_x)^2 + (y(i) - p2_y)^2$
10:    **end for**
11:    $j \leftarrow arg_i min\ d1(i)$
12:    $k \leftarrow arg_i min\ d2(i)$
13:    **if** $mode =$ upper **then**
14:        NewContour = Concatenate(*Contour*$(m)_{j<m<k}$ , *Curve'*)
15:    **end if**
16:    **if** $mode =$ lower **then**
17:        NewContour = Concatenate(*Contour*$(m)_{k<m<j}$ , *Curve*)
18:    **end if**
19: **return** *NewContour*
20: **end procedure**

---

Taking into account the clockwise sense of circulation of the *Contour*, and being $p1_x < p2_x$, it can be verified that, if the curve lays below the contour, then is $k < j$. Therefore, comparing the index of the contour points with $j$ and $k$ it can be determined if they belong to the upper or the lower portion of the Contour, i.e. contour points with an index smaller than k and greater than j define the portion that lies above the points p1 and p2, and those contour points with indices between k and j define the lower portion of the contour.

Depending on the mode of operation (*mode*) the algorithm concatenates the upper portion of the contour (lines 13 to 15 *Contour*$(m)_{j<m<k}$) or the lower portion of the contour (lines 16 to 18 *Contour*$(m)_{k<m<j}$) with the

curve. It is worth noting that the *Curve* has previously been reversed in line 14 (denoted by *Curve'*) in order for the resulting contour (*NewContour*) to be an ordered set with clockwise circulation.

# Chapter 4

# A knowledge-based approach for the automatic lung segmentation

The human perception of an image is a complex process that cannot be entirely described by means of rules or statistical approaches. Nevertheless, experiments performed on psycho-perception of images have revealed important aspects that have been incorporated in this work to improve the quality of the segmentation. Some of the most important findings [90] related to "human segmentation" are:

- The use of *a-priori* knowledge improves the image interpretation.

- Segmentation and classification are combined into a single process during the perception of an image.

These two considerations have inspired the design of the segmentation procedure developed in this work. The structures which are easier to identify (based on previously acquired anatomical knowledge) are segmented and classified first, thus reducing the complexity of the further segmentation problem. At the same time, the information gained from the structures already classified is used to improve the results of the remaining segmentation and classification steps.

As explained in chapter 3, image segmentation consists of the partitioning of an image into regions with similar properties which are further classified

as object or background. According to this definition, segmentation methods based on texture, gray level, or intensity gradient currently used to segment lungs [22, 14, 16, 91, 25, 48, 19, 11, 15, 13] would not be able to recognize the lung with atelectasis in a CT image as a unity. Rather, they would split it into multiple regions along with their different characteristics. On the other hand, the ability of a human being to recognize and manually segment the lung is highly influenced by his/her previous anatomical knowledge not only of the lung but of the whole thorax and the "common properties" used to segment an image are not restricted merely to the analysis of intensity and texture. Those regions in the image where the lung does not show any difference from the surrounding tissue do not provide information that can be used by an expert to find the limits of the pulmonary parenchyma, therefore, it must be "guessed" on the basis of the position of other organs, bones or anatomical structures that can be easily recognized. Taking this into account, a strategy aimed at using as much anatomical information as possible is followed.

A typical difficulty in the segmentation of biological images lies in the variability of the anatomical structures among different individuals. Many different approaches have been developed in the last years to face this problem like elastic deformation and registration [92, 93, 94, 95, 96], statistical atlas [17, 97, 93], a combination of both [98], among others, but none of them is suitable for dealing with the additional variability factor due to different degrees of induced atelectasis that concern the current study. The identification of features in the images that remain unaltered or quasi invariant despite of the inter and intra individual variability and different degrees of atelectasis is one of the core issues of this thesis. This allows the finding of reliable landmarks that are explicit in the images leading to a segmentation of the lung that equals, in some of its regions, the accuracy achieved by an expert.

## 4.1 Overview of the segmentation algorithm

The method proposed in this work to segment the lung can be regarded as a complementary segmentation approach, meaning that the lung itself is

not segmented but rather the anatomical structures that bound it, in order to identify and delimit the lung parenchyma. This process is illustrated in figure 4.1 and explained in the rest of this chapter. In section 4.3, the body segmentation is developed. The body defines the ROI that will be processed in the following segmentation steps. Section 4.4 introduces the segmentation of the airways and the carina identification. The position of the carina will define the origin of a reference system employed by a number of algorithms which analyze the relative position and shape information of bones and other anatomical structures in order to classify them. In section 4.5 the ribs and vertebrae are identified and with the help of this information, the pleura, i.e. the limit of the lungs in the dorsal region is segmented. Section 4.6 presents a model to estimate the diaphragm dome, defining the base of the lung. Section 4.7 describes the aorta segmentation and section 4.8 explains the identification of the stomach. Finally, section 4.9 presents an algorithm for the segmentation of the lung, combining the results obtained from the segmentation of the individual anatomical structures previously mentioned.
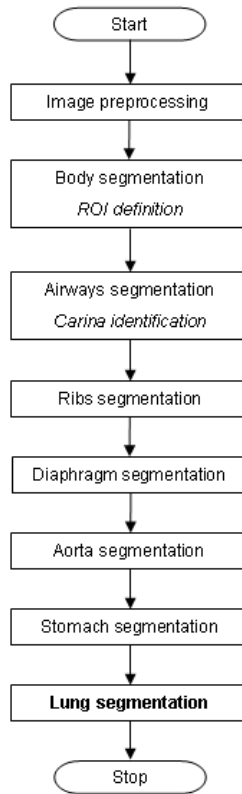
Figure 4.1: Lung segmentation flow chart. This pipeline model illustrates the hierarchy of the individual anatomical structures segmentation, indicating that each step employs the results of the preceding one. The procedure concludes with the lung segmentation which combines the information gained along the descending chain.

## 4.2 Image data and preprocessing

The image data consists of helical computed tomography (CT) scans of the chest organized as a stack of axial slices defining a 3D volume array or rectangular grid of voxels that include the thorax from the trachea to below the diaphragm, thus covering the entire lungs. The pixel size ranges from 0.47 × 0.47 to 0.51 × 0.51 mm$^2$ and the slice thickness is either 1 mm or 5 mm. The data set images are provided by the scanner in DICOM format and each volume scan contains a stack of contiguous slices.

The radiograph attenuation of each pixel is expressed in Hounsfield units (HU):

$$HU = \frac{\mu - \mu_{H_2O}}{\mu_{H_2O}} * 1000$$

where $\mu$ is the linear attenuation coefficient of the material and $\mu_{H_2O}$ is the linear attenuation coefficient of water.

This scale arbitrarily assigns a value of 1000 HU to bone (complete absorption), a value of -1000 HU to air (no absorption), and a value of 0 HU to water.

The image preprocessing resembles that proposed in [41]. Each transversal plane image is smoothed with a 2D median filter ($7 \times 7$ pixels) in order to prevent the noise from producing undesired artifacts (see figure 4.2). At the same time, it smooths the edge of the lung and other anatomical structures leading to better segmentation results. The filtered slices are stored for further processing by the multiple algorithms that contribute to the final lung segmentation.



(a)                                    (b)
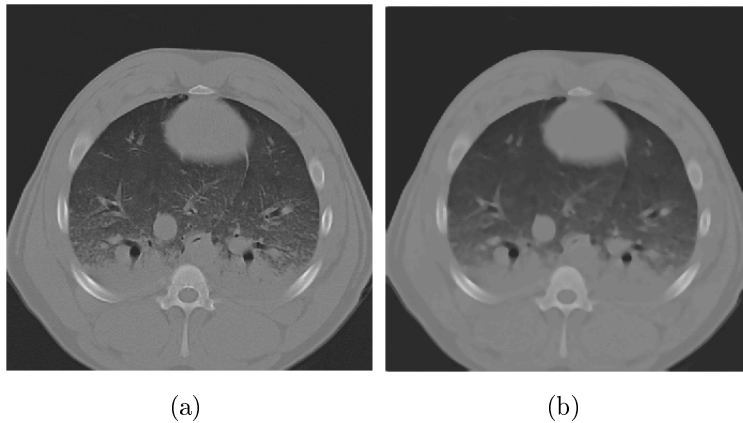
Figure 4.2: CT image preprocessing. (a) Original CT image. (b) Filtered image.

## 4.3 Body segmentation

The body is segmented in the transversal plane by a 2D slice by slice threshold-based algorithm (see figure 4.3). A bi-level[1] image is created from the slice being analyzed by setting those voxels to 1 with a value above -300 HU (this value has been empirically determined to involve soft tissue and cortical bone in the segmentation) and clearing the rest. The result of this operation is shown in figure 4.3 (a). There the body segmentation (white pixels) includes holes[2] corresponding to the anatomical structures with high contents of air, like some regions of the lungs and airways, with a value below -300 HU. These holes are further removed by a simple flood-fill operation (figure 4.3 (b)). At this point, all pixels inside the body are set to 1 and the surrounding (air) pixels are set to 0. Finally, the contour that delimits background (air) from foreground (body) is stored, defining the ROI that will be processed along the following segmentation steps and the bi-level image is discarded in order to reduce the memory requirements.

The goal of this first stage towards the lung segmentation is to reduce both the processing time and potential errors by preventing the algorithms to explore and process regions of the image outside the ROI. Figure 4.3(c) illustrates the ROI applied to the filtered CT image.

---

[1] A bi-level image is defined as a logical array containing only 0s and 1s, interpreted as black and white, respectively.

[2] A hole is defined as a set of background pixels that cannot be reached by filling in the background from the edge of the image.
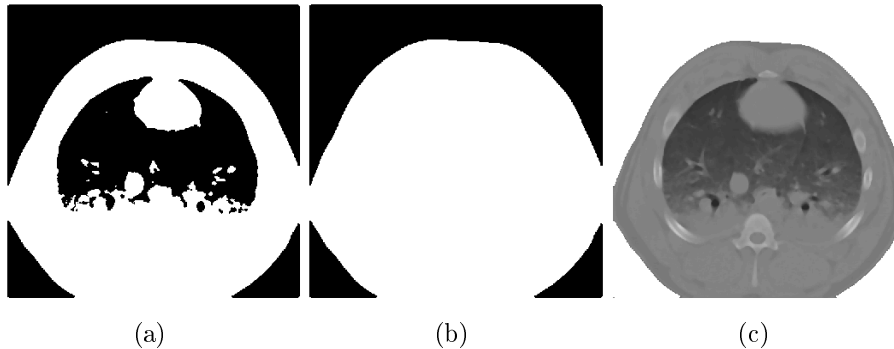
Figure 4.3: CT image definition of the ROI. (a) Mask of the body with holes. (b) Mask of the body after holes have been filled in. (c) ROI of the filtered image.

## 4.4 Airways segmentation

The airways are the first thoracic anatomical structure segmented as mentioned in section 4.1. They possess the important property of remaining unaltered with the atelectasis, thus providing valuable information independently of the stadium of the disease. Due to their characteristic gray level (below -900 HU), the lowest observable in the thoracic CT, the identification of the airways is relatively simple. They are usually segmented with region growing algorithms [11, 28, 26, 27], getting satisfactory results up to the $6^{th}$ bronchi generation. However, these methods require thin-slice CT images and are not optimized for atelectatic lungs, therefore, they are not suited for some of the experiments that this study is concerned with.

In this section, an algorithm to segment the trachea and primary bronchi independently of the atelectasis degree is presented. With the help of this approach, also applicable to a 5 mm slice thickness, it is possible to identify the position of the carina in the airways. Moreover, the artifacts produced by the presence of the endotracheal tube (ETT) have been taken into account during the design of the algorithm, in order to reach a robust segmentation of the upper airways despite of the presence of the ETT.

A specially attractive landmark is the carina. This point, where the trachea divides into the right and left primary bronchi, is always clearly

visible in CT scans. Additionally, it shows only a moderate inter individual variability and is intimately related to the lung anatomy. This is why the carina position will be chosen as the origin of a reference coordinate system that will be used for several segmentation steps of the anatomical structures that provide additional information for the lung segmentation.

Although the following approach cannot be regarded as a region growing algorithm, it is based on the connectivity between 2D regions (contours) of adjacent layers, thus enlarging the airways volume beginning with the first contour identified as trachea (seed) and growing downwards up to the end of the primary bronchi. Contrary to classical region growing, the criterion employed to enlarge the volume is not limited to the analysis of gray level. Instead, shape and position features extracted from the contours of each slice are considered. Those contours that originate from the airways meet the requirements expected to contribute to the volume growing. Other contours that stem from non-airways parenchyma like hyperventilated zones of the lungs and the esophagus, which have a similar gray level to that of the airways, are excluded from the segmentation as their features do not match that of the trachea and bronchi.
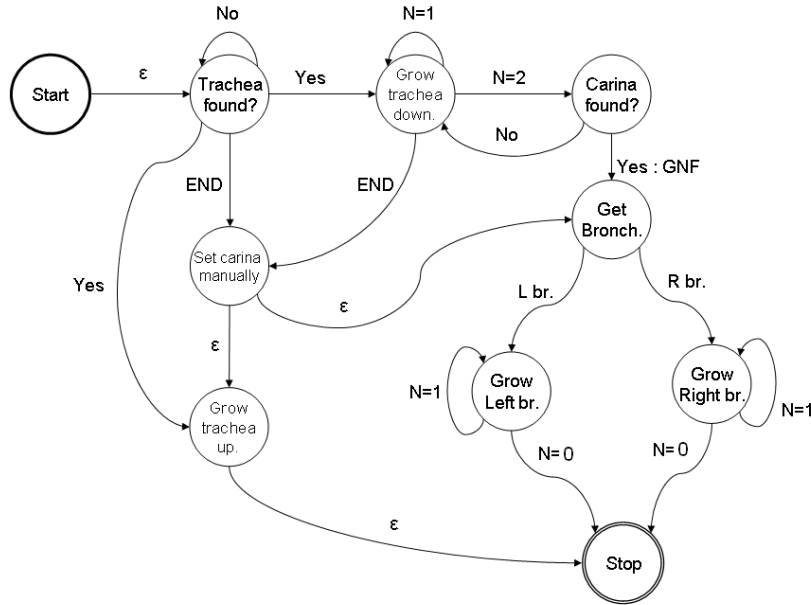
Figure 4.4: Finite state automaton used for the segmentation of the airways.

More specifically, a thresholding algorithm pre-segments all regions below -900 HU of each filtered slice of the volume CT data. The result of this operation is a set of contours in each frame, that delimit the regions identified as "air". The following step validates slice by slice the contours pre-segmented before they are appended to the set which defines the airways volume. Based on the shape and position of each contour, 3 classification trees classify them into trachea (figure 4.5 (a)), carina (figure 4.6 (a)), bronchi (4.7 (a)), or none of them. Those contours that fulfill the expected requirements contribute to the growing of the airways. Otherwise, they are rejected. Starting from the uppermost transversal frame, the trachea is identified. Ideally, in the transversal sectional CT image, the trachea looks like a black disk the diameter of which remains quasi constant from the larynx up to the carina. Based on this hypothesis it can be recognized considering merely its area [11]. However, observations based on the animals of the training set (appendix B.1) indicate that the identification of the trachea of a pig based on this single feature may fail, especially when the trachea is intubated. The mentioned deviations from the ideal case require the evaluation of features that provide

the segmentation algorithm with additional information. Consequently, each contour is fitted with an ellipse characterized by its major and minor radius (r1,r2), the rotation angle between the main axis and the X axis ($\alpha$), the root mean squared error of the radial distance between each point of the contour and the ellipse (normalized with the ellipse radius at the respective points) (RMSE), and the displacement of the ellipse-center between adjacent slices ($\Delta Cx$, $\Delta Cy$).

Since the shape and number of the airway contours depend on the position of the transversal slice considered, a finite state machine (FSM) [99] shown in figure 4.4 controls the validation and appending process. This automaton decides which classification tree must be employed to identify the trachea, carina or bronchi contour according to the frame position, as will be explained below.

The process starts at the uppermost transversal frame of the CT volume data (*Start* state) with the search of the trachea. After having extracted this frame, the FSM changes to the state labelled *Trachea found?* where it continues analyzing the subsequent frames downwards (edge *No*) as long as no contour is classified as trachea by the classification tree illustrated in figure 4.5 (a). If the last frame of the volume CT data is reached and the trachea could not be detected, it must be manually identified (edge *END* that leads to the *Set carina manually* state).

When the trachea has been found, the FSM changes (edge *Yes*) to two states simultaneously which tracks and segments the trachea upwards (state *Grow Trachea up*) and downwards (state *Grow Trachea downwards*). In this state, the contours of adjacent slices that overlap are appended to the trachea segmentation (edge *N=1*) if the following condition is fulfilled: only one contour of the lower frame must overlap the contour of the upper frame (this is described by the notation *N=1*). If 2 contours of the lower frame are overlapped by a single contour of the upper frame (*N=2*), the FSM changes to the state *Carina found?*. The presence of the 2 contours may be due to one of the following reasons: *a*) The trachea has been completely segmented and the upper frame being analyzed corresponds to the carina, therefore, the 2 contours of the lower frame are the left and right primary bronchi. *b*) The

51
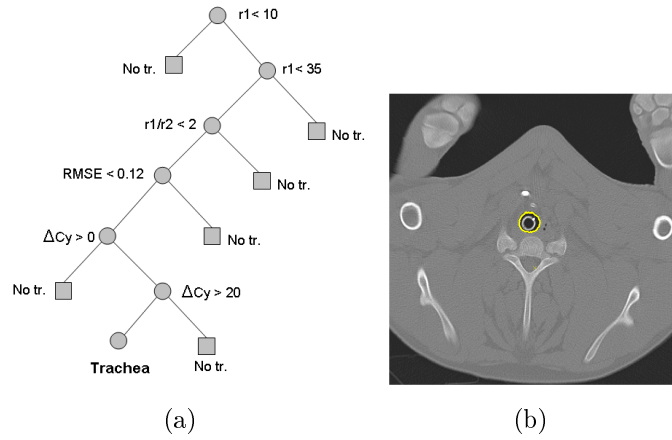
Figure 4.5: Trachea validation. (a) Classification tree used to classify the trachea. (b) Trachea segmentation 8.5 cm above the carina. The gray circle inside the trachea is the ETT.

carina has not been reached, one contour in the lower frame corresponds to the trachea and the other one is the bronchus trachealis[3] (figure 4.7 (b)). This analysis is performed in the state *Carina found?* using the anatomical knowledge contained in the classification trees shown in figures 4.6 (a) and 4.7 (a). If the alternative *b* is detected, the FSM returns to the state *Grow Trachea* and continues with the trachea segmentation as explained before. If the carina was found, its coordinates are registered and the FSM transits through the edge *Yes* to the *Get Bronchi* state where the contour of the left *(L br)* and right *(R br)* primary bronchi are identified as 2 independent seeds to enlarge these bronchi downwards (transition to states *Grow Left bronchus* and *Grow Right bronchus*). The procedure stops when the bronchus contour of the upper slice does not overlap any contour of the slice below it (N=0).

The state *Grow Trachea upwards* processes sequentially the frames upwards beginning from the carina if the previous state was *Set carina manually* (or the first valid trachea contour if the previous state was *Trachea found*). The contours of the upper adjacent slice are appended to the trachea independently of its shape in order to ignore the artifacts due to the ventilator.

---

[3]This bronchus is a singularity of the pig anatomy not observed in humans.
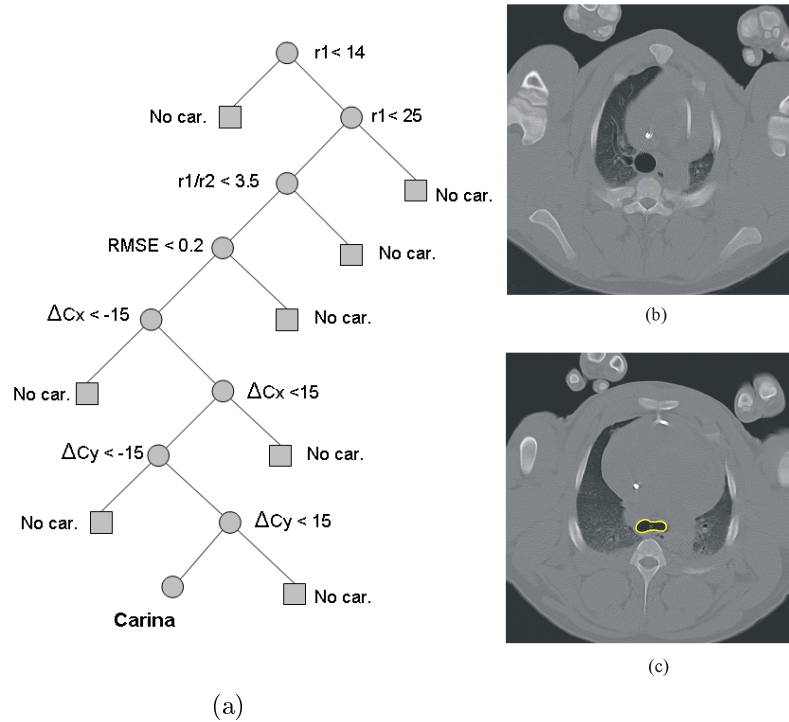
Figure 4.6: Carina validation. (a) Classification tree used to classify the carina. (b) Trachea and bronchus trachealis. (c) Carina segmentation.

Consequently, the trachea "grows" in cranial direction until no more overlap between adjacent frames is detected.

When the airways segmentation concludes, and the position of the carina has been identified, the mentioned reference system with origin in the carina is established.

The analysis of the overlapping contours is performed by the *Contour Overlap* algorithm (appendix 3.5.1) the parameters of which are set according to the state of the FSM where the overlap is examined. For a detailed description of the values assigned to parameters of the mentioned algorithm, please refer to appendix A.1.
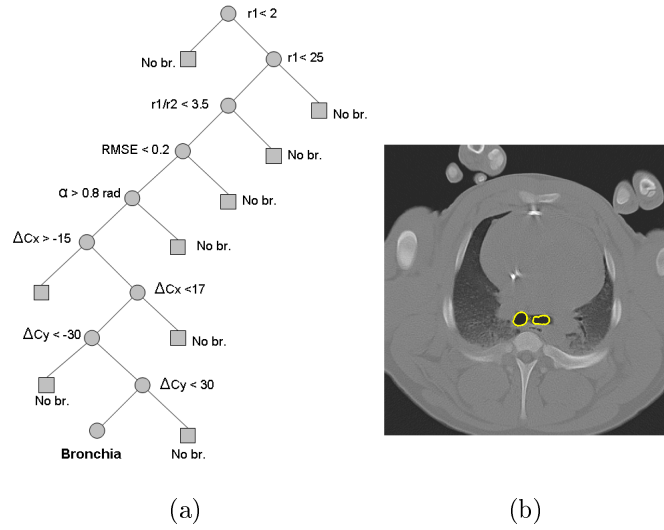
Figure 4.7: Bronchi validation. (a) Classification tree used to classify the right and left primary bronchi. (b) Primary bronchi segmentation.

## 4.5 Bone landmarks

In chapter 2 the anatomical position of the lungs related to the ribs has been described. As has been shown there, that in the dorsal (dependent) zone of the thorax the lung parenchyma is separated from the ribs by the pleura, a thin membrane the dimension of which is comparable to the pixel size of the CT image. Thus, the points where the ribs are in contact with the pleura are potentially excellent landmarks for delimiting the lung.

If CT volume data of the whole thorax is not available, a set of landmarks taken from the visible areas of the lung and the bones can be extracted from the transversal plane of the CT image as proposed by [41]. This method can be summarized as follows: the bones are segmented and classified according to their anatomical position into sternum, right ribs, left ribs and vertebrae. They define the landmarks that, together with the lung landmarks (figure 4.8 (b)), are interpolated with a Bezier curve (spline) which is in turn the contour that encloses the lungs. If in the analyzed slice the articulation between the vertebra and the rib is not visible, additional interpolation landmarks need to be estimated to assure that the segmentation follows the border of the lung. Finally, the heart is identified and removed from the contour obtaining

the definitive segmentation of the lungs. This approach has the advantage that the lungs can be segmented from a single slice (transversal plane) taken from the region of the heart, but it is not applicable in the apical and in the basal region. It also ignores vessels and airways, therefore, they are included in the lung parenchyma as shown in figure 4.8 (c).



(a)            (b)            (c)
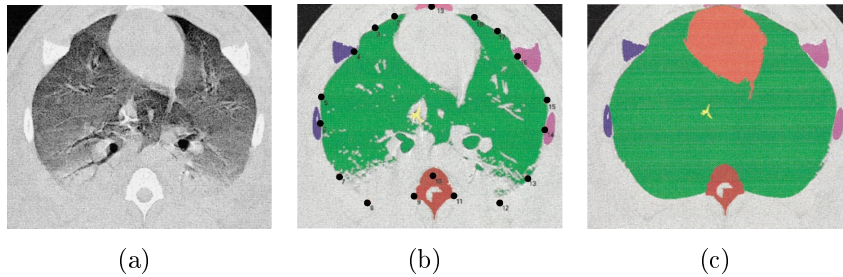
Figure 4.8: Bones landmarks and lung segmentation. (a) CT image of the animal after ARDS lavage. (b) Recognition of lung areas (green) after threshold segmentation between -1024 and 275 HU. The black points in the image show the position of the bones and lung - landmarks. (c) Final segmentation of the lung (green) after suplementation of the lung areas identified in (b) with the area defined by the Bezier curve (landmark interpolation). The heart (red) is segmented by a thresholding algorithm (HU range from -175 to 275). (after [41]).

When 3D CT data is available, it is also possible to extract the bones-landmarks (specifically the ribs-landmarks) from the sagittal plane yielding a segmentation of the dorsal zone of the lung that is extremely accurate and may be even better than the one reached by an expert who is merely guided by the transversal plane CT image. This results from the capability of the algorithm to process information existing in the 3D data that is not accessible when a single slice has to be used for the manual segmentation. This approach which is one of the main contributions of this work is described in the following section.

## 4.5.1    Ribs segmentation and landmarks extraction

The method employed to segment the ribs is analog to that introduced in section 4.4. The contours of the bones pre-segmented in the sagittal planes by
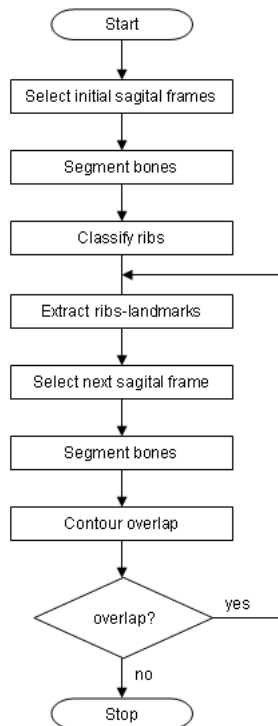
Figure 4.9: Image processing steps followed to segment the ribs and extract the ribs-landmarks.

a thresholding algorithm are appended to enlarge the ribs volume beginning with the seed ribs contours, which are distinguished from the contours of other structures by a classification tree. This procedure is illustrated in the flow chart shown in figure 4.9.

The image processing starts by selecting two sagittal plane images at about 5 cm to the right (figure 4.10(a)) and 5 cm to the left (figure 4.10(c)) to the carina (figure 4.10(b)), referred to as *right and left initial frames*. The choice of these particular slices was motivated by the properties mentioned below[4] which are more prominent in the selected position than in other sagittal frames.

1. The ribs used to produce landmarks (referred to as *valid ribs*) are quite similar to each other.

---

[4]These properties result from observations made by the author with respect to the volume CT data of the animals used as training set

2. Ribs (and other artifacts) that are inadequate to derive landmarks from (referred to as *no rib*) are quite different from the valid ribs.

3. At least 10 valid ribs per frame can be reliably identified according to their gray level, size and position. The extraction of these features is straightforward allowing fast computation.

Following from points 1. and 2., the *valid ribs* build a dense cluster in the feature space (figure 4.11) that is easily distinguished from the *no ribs* class. Therefore, the difficulty faced by the classification algorithm is very low resulting in a misclassification near 0.

These characteristics disappear gradually as the sagittal plane frame approaches the backbone (figure 4.12).

In the initial frames, a thresholding algorithm pre-segments the bones (and other structures) with a gray level over 150 HU. Usually the interior of the bones (medulla) shows darker than their border, resulting in a "double" segmentation, i.e. one contour delimits the bone and another one, inside, delimits the medulla. To avoid this problem, a flood-fill operation equalizes the gray level of each rib with that of its border.

The entities pre-segmented in the previous step undergo a classification algorithm (4.5.2) that validates those ribs that will be used to define landmarks and rejects other ribs and structures that are not desired (figure 4.13 (b)). The results of the image processing at this point are shown in figure 4.10(d, f).

Having identified the valid ribs in the initial frames, a loop starts as shown in the flow chart (figure 4.9) that analyzes sequentially all frames to the right and to the left of the left initial frame in order to identify valid ribs by means of the *Contour Overlap* algorithm (section 3.5.1) and extracts landmarks until a stop condition is met.

The same procedure is repeated with the right initial frame and the frames at both of its sides.

In each frame that is evaluated, the regions with gray level above 150 HU are pre-segmented by a thresholding algorithm resulting in a set of contours that corresponds to valid ribs and other undesired structures. In each
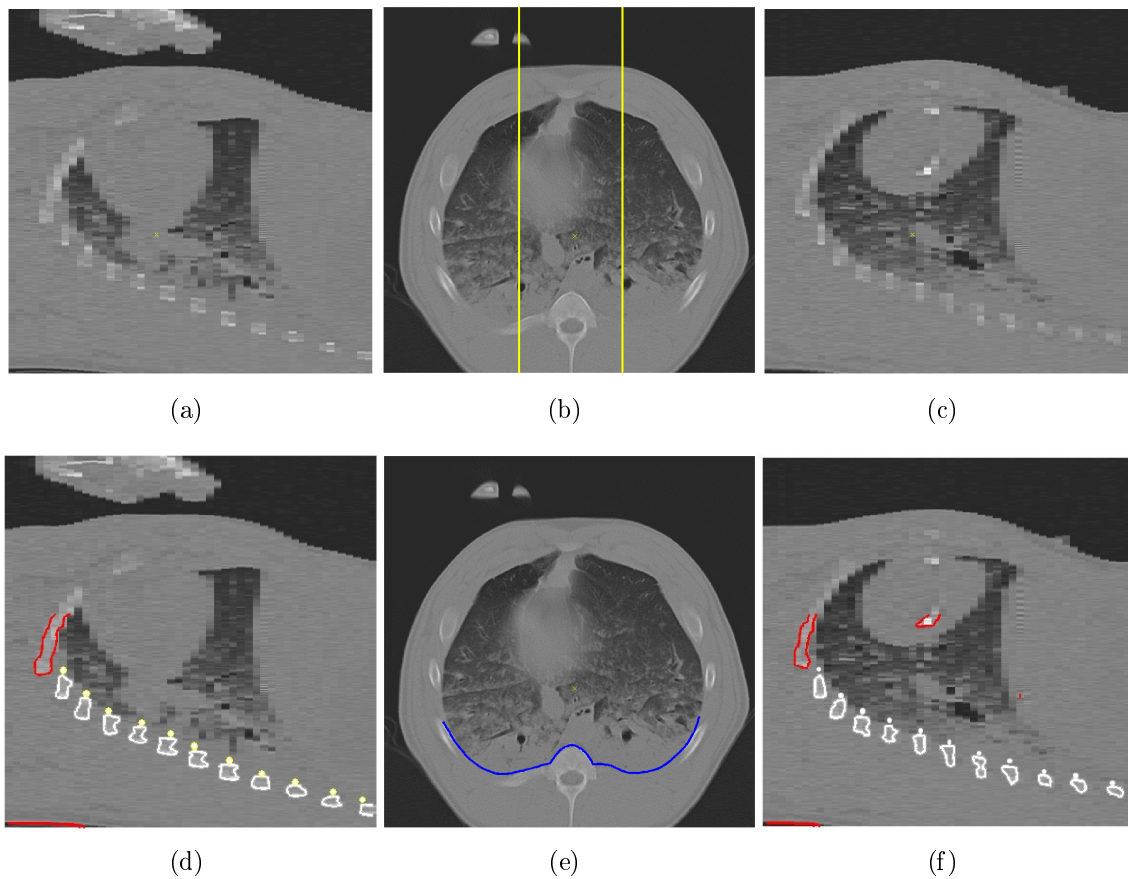
Figure 4.10: Example of the images used as initial frame for the segmentation of the ribs. (a) Sagittal plane that corresponds to the left line of (b). (b) Transversal plane below the carina. The vertical lines indicate the sagittal planes selected to start with the ribs segmentation. (c) Sagittal plane that corresponds to the right line of (b). (d) Ribs segmented from (a) used as seed for the contour overlap algorithm. The points above the ribs are landmarks. (e) Ribs landmarks interpolated in the transversal plane complemented with the vertebra segmentation. (f) Ribs segmented from (c).
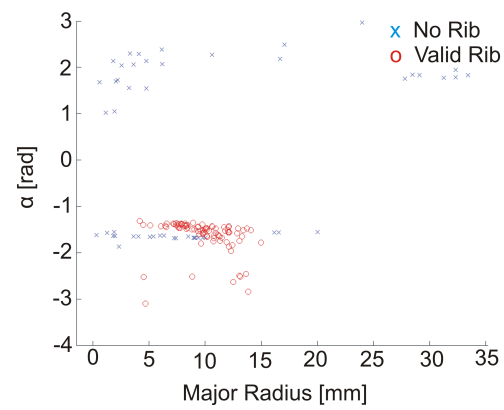
(a)
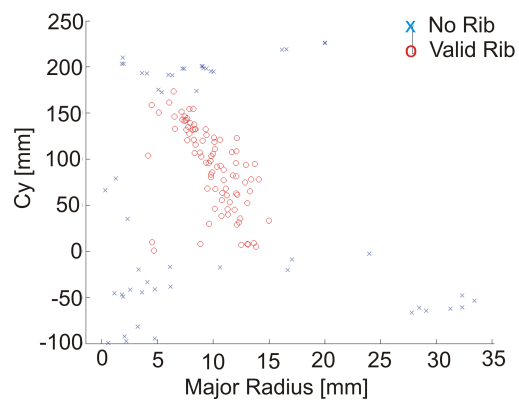


(b)

Figure 4.11: 2D projections of the 4D feature space used for rib classification. The valid rib class builds a dense cluster even when based on only 2 features.

iteration, two contiguous frames are examined: the current frame containing valid ribs that are already known and the next frame where the valid ribs will be searched .

Specifically, starting at the position of the left initial frame in the first pass of the loop, the next frame to the right is extracted. The valid ribs classified in the initial frame are used as seed for the Contour Overlap algorithm[5] to validate the bones segmented in the next frame. The ribs validated in this step, i.e. the valid ribs, will be used as seed for the following iteration to validate the bones segmented in the following sagittal plane. This loop continues until a sagittal plane is reached where no more ribs are validated as no overlap is observed, meaning the stop condition was reached.

Each valid rib found in each sagittal plane defines one landmark the position of which is the (X,Y,Z) coordinate of the highest[6] point of the rib contour (figure 4.10(d)).

The procedure described above is analog to a region growing algorithm[7] but applied to contours instead of pixels, in the sense that the region grows appending contours that overlap along neighboring frames.

Although the ribs are basically segmented with a 2D thresholding algorithm, the whole segmentation approach uses 3D information to enhance the robustness and accuracy of the final result.

It is worth noting that when the sagittal plane being analyzed approaches the backbone, the shape of the ribs changes (costo-vertebral articulation) and it can be segmented with 2 contours where only the upper one is useful for the landmark definition. It is also possible, due to image artifacts, that two contours in a frame overlap a seed contour in the previous frame, which produces undesired results. To prevent such problems, the Contour Overlap algorithm is set up to return only one upper contour in the above mentioned case (figure 4.12).

---

[5]The contour of the ribs segmented in the next frame that overlap with the contours of the valid ribs found in the current frame are validated, the rest are discarded.

[6]Considering that the body lies in supine position, the highest point of a rib section in the sagittal plane is the nearest to the sternum.

[7]Region growing is a procedure that groups pixels into regions. The simplest approach is pixel aggregation, which starts with a seed pixel and grows a region by appending spatially connected pixels that meet a certain homogeneity criterion.
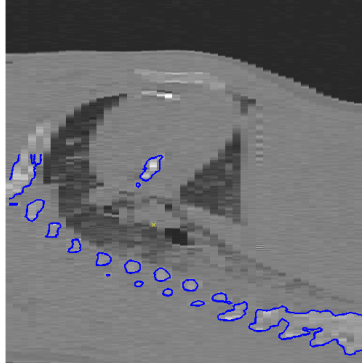
Figure 4.12: Example of a sagittal plane near the backbone.

After the rib segmentation is finished, there are at least 500 3D landmarks[8] available for each lung to build an interpolating surface that corresponds to the boundary between the dependent zone of the lung and the ribs. This approach leads to a very robust segmentation that relies on the large amount of landmarks that can be reliably identified. If some ribs are not segmented because the algorithm fails, there is still enough redundancy to interpolate a surface that accurately matches the lung limit. One profile of this surface, complemented with the segmentation of the vertebra (see 4.5.3), is shown in figure 4.10 (e).

## 4.5.2 Ribs classification algorithm

The segmentation of the bones of the initial frame (figure 4.13 (b)) produces a set of contours, some of them originating from the ribs that will provide landmarks (*valid rib*) and others coming from artifacts like probes or bones that have to be ignored (*no rib*). For the classification of the contours into valid rib and no rib, the classification tree shown in figure 4.13 (a) has been employed. Beforehand, features based on the gray level, size and position relative to the *carina coordinate system*[9] need to be derived from each contour. These features are the predictor values of the tree:

---

[8]They result from the identification of circa 10 valid ribs per sagittal frame multiplied by 50 frames that are analyzed for each lung.

[9]The origin of the coordinate system used as reference to measure distance and angle of the features, is set to the (z,y) coordinate of the carina.
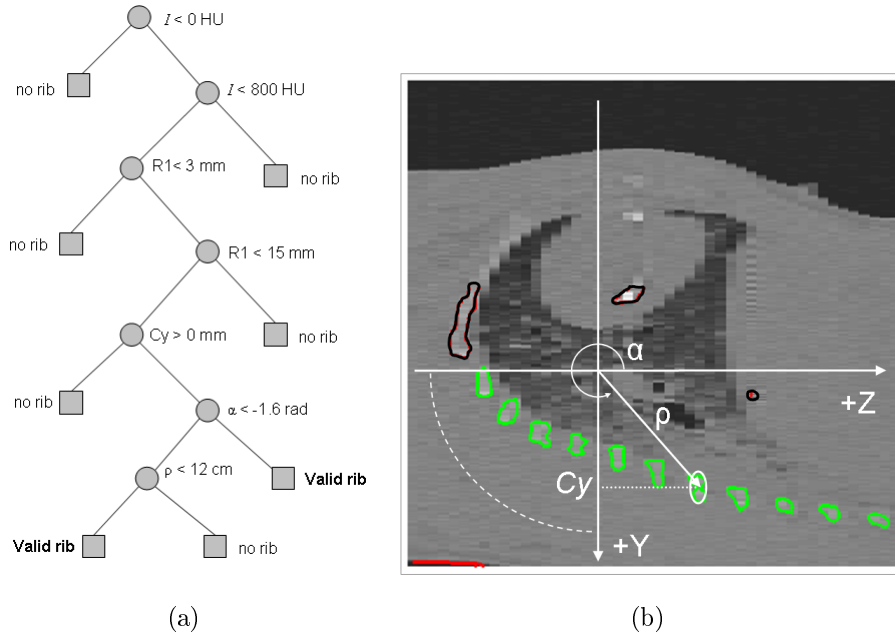
Figure 4.13: Ribs classification. (a) Classification tree employed to classify the ribs. The predicted categorical values are the two classes we are interested in, namely *valid rib* and *no rib*. The features derived from each segment are the predictor values of the tree. (b) $\alpha, \rho$ and $Cy$ are some of the features extracted from the initial frame (sagittal plane) to classify the ribs. The dashed line shows the distance to the carina equal to 12 cm.

- $\alpha$ and $\rho$ : angle (measured counterclockwise from the z axe) and radius of the vector that points to the center of the ellipse which best fits the contour.

- $R_1$: major radius of the ellipse that best fits the contour.

- $I$: mean value of the voxels gray level inside a contour (expressed in HU)[10].

The mentioned features are derived from the 2D sagittal plane image and all distances and angles are measured in this plane as well.

---

[10]The mean gray level of a segment is computed from the original image (no filtering) in order to avoid the influence of those pixels outside the contour that may be used by the filter.

The classification tree has been constructed with Matlab based on [82] using a training set of 10 pigs ( see appendix B.1) taking into account that the cost of classifying a *no rib* segment as a *valid rib* is much higher than the cost of the inverse. In fact, if a valid rib is not recognized, the impact on the final result on the lung segmentation is likely to be negligible because there is enough redundancy, coming from the large number of valid ribs that are correctly classified. In contrast, if one *no rib* segment were misclassified, this would severely distort the shape of the lung because the landmark interpolation must fit an "outlier" that is not part of the rib cage (e.g. like the searcher inserted in the alimentary canal).

The performance of the classification tree has been measured with a test set of 10 animals (see appendix B.2), that differs from the training set. The results show a misclassification rate of 4% for *valid ribs*, i.e. 4% of valid ribs have been classified as *no rib*, and 0% for *no rib*.

### 4.5.3   Vertebrae segmentation and landmarks extraction

The vertebra segmentation is straightforward as no classification is necessary. The image processing consists of four steps repeated for each transversal frame of the volume data as described below and exemplified in figure 4.14. It is worth noting that for this segmentation process no 3D information was used. This is because the task of identifying the upper contour of each vertebra can be performed accurately with 2D information.

First, a ROI defined by the position of the costo-vertebral articulations is extracted from the transversal plane (figure 4.14(a)). Second, a thresholding algorithm generates the contours of all regions which gray level lays over 150 HU (figure 4.14(b)). Third, an auxiliary rectangular contour is created in the bottom of the ROI that overlaps with the vertebra (dashed line rectangle in the lower part of figure 4.14(c)). Finally, the Contour Overlap algorithm (section 3.5.1) identifies the biggest contour that overlaps the auxiliary contour, which is the portion of the vertebra (figure 4.14(d)) we are interested in. This contour complements the profile defined by the ribs in the transversal plane (figure 4.10 (e)).

After the vertebrae have been segmented, a contour per frame has been identified. Each contour defines one *vertebra landmark* which position is the (X,Y,Z) coordinates of the uppermost point of the contour (figure 4.10 (e)).



|       |       |       |       |
| :---: | :---: | :---: | :---: |
| (a)   | (b)   | (c)   | (d)   |
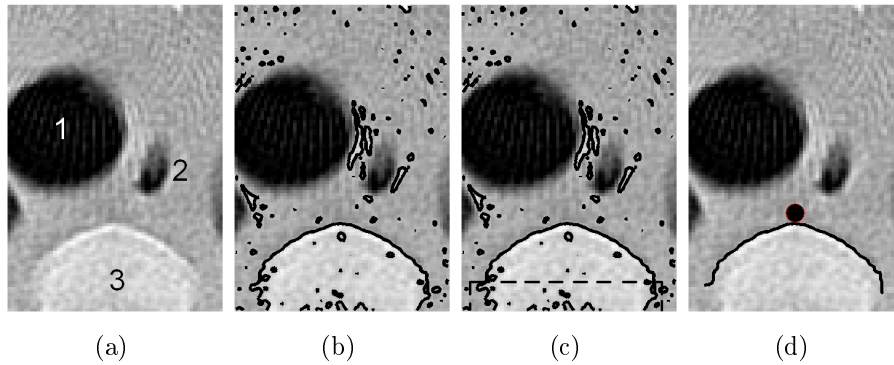
Figure 4.14: Vertebra segmentation sequence. In the image (transversal plane) the trachea (1), esophagus (2) and one portion of a vertebra (3) can be seen.

The anatomical structures employed at this stage of the lung segmentation procedure are common to all vertebrates though probably a specie-specific classification tree should be generated from an appropriate training set.

## 4.6 Diaphragm segmentation

In this section, a procedure for the segmentation of the base of the lung which relies on an anatomical model of the upper surface of the diaphragm will be introduced. The thoracic diaphragm, hereby referred to as "diaphragm", delimits the base of the lungs and separates them from the abdominal cavity.

The CT number of this muscle is approximately 100 HU and can be easily distinguished from the lungs when they are filled with air but it is not clearly discriminable from the atelectatic lung parenchyma. Therefore, anatomical information previously learned must be considered to overcome the missing graphical information in the CT images, thus allowing the segmentation algorithm to produce reliable results.

64

Beichel presents a 3D Active Appearance Model (AAM) approach for the segmentation of the top layer of the diaphragm dome. Although this approach has been applied to human lungs without atelectasis, it shows some deficiencies when it comes to fully match the dome surface in local regions [34].

The segmentation algorithm presented in this section is based on a 2D approach that estimates the base of the lung (BL) in each sagittal plane by interpolating 4 landmarks of the diaphragm: A, B, C and D (figure 4.15 (a)) derived from each sagittal image. Two of them (A and B) are reliably extracted from the ventral zone of the lung. The position of C can not be identified in the CT image of an atelectatic lung, and consequently is assessed using anatomical information previously learned from the training set. Landmark D is positioned by the diaphragm model according to the coordinates of B and C. Further details about the landmarks and the interpolating curve are given in sections 4.6.1 to 4.6.4.

The selection of the sagittal plane and the 4 landmarks to develop a model of the upper surface of the diaphragm valid for PEEP levels below 16 cm $H_2O$, for the whole breath cycle and for different degrees of atelectasis was motivated by the following observations (figure 4.15):

1. The cross-sectional image of the BL in the sagittal plane is a curve that can be modeled by the interpolation of 4 points with a cubic spline [100]. The model needed to define the BL in the transversal or coronal plane is more complex and requires more interpolating points (figure 4.16).

2. The intra individual variation of the BL along the sagittal planes of the lung is reduced, therefore the BL can be accurately described with the same model independently of the position of the sagittal plane. This property does not hold for the transversal and the coronal planes however.

3. The atelectasis is only visible for PEEP levels below 16 cm $H_2O$ in the dependent zone of the lung (when the animal lies in supine position). Therefore in the ventral region the high contrast between the dark vox-

els of the lung parenchyma and the surrounding tissue provides enough information for its segmentation independently of the lung pressure.

4. If the PEEP level is higher than 16 cm $H_2O$, the atelectasis is not visible in the CT image and the whole lung can be reliably segmented with a thresholding algorithm without the need of a model. Therefore, this pressure defines the highest pressure for which the model needs to be valid.

5. The lower border of the lung in each sagittal plane, identified with the landmark C, bounds with the ribs and the diaphragm. Therefore, the Y coordinate of C is given by the respective Y coordinate of the ribs which has been previously segmented with high accuracy.
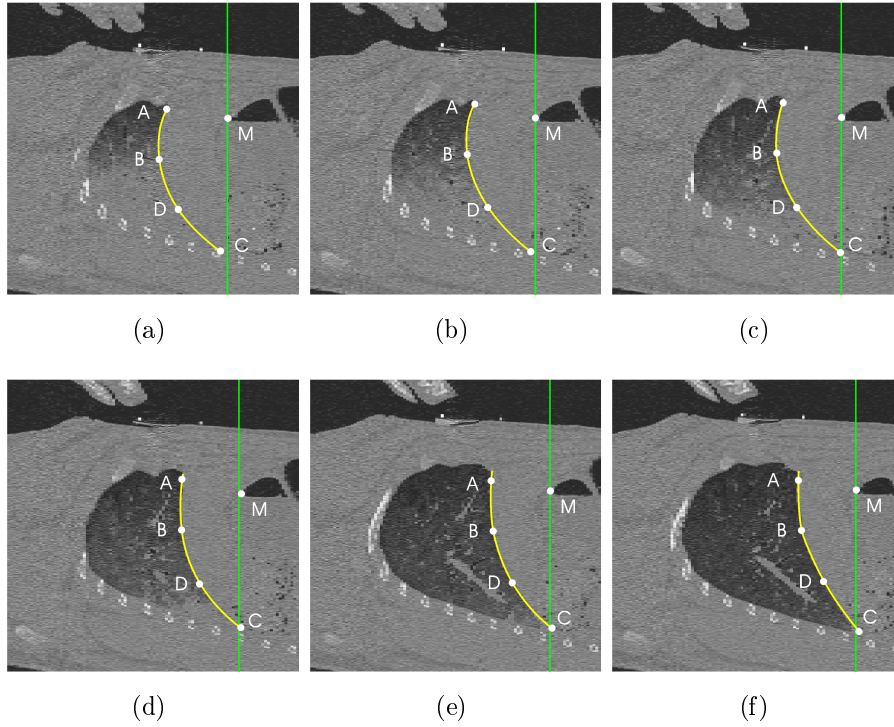
Figure 4.15: Manual segmentation of the BL in the sagittal plane for different PEEP levels. Images taken during end inspiration of a lung with atelectasis. (a-f): 0, 4, 8, 12, 16, 20 cm $H_2O$ PEEP level. Witch increasing pressure, the shape of the BL changes and the atelectasis becomes invisible. The dependency of D with the pressure is given by the position of landmarks B and C. Landmark M identifies the top of the stomach.

### 4.6.1 Ventral landmarks A and B

The Y coordinates of A and B, $A_y$ and $B_y$, are set to -4 cm and 0 cm respectively, measured in the reference coordinates system with origin in the carina (figure 4.16(b)). The Z coordinate of both landmarks is obtained directly from the CT image on the BL and segmented by means of a thresholding algorithm. The Y coordinate of B remains unaltered for all sagittal planes. The same holds for A, except for those frames where the cross-sectional image of the lung is below[11] -4 cm (figure 4.16(b)). In this case, the ventral

---

[11]Considering that the animal lies in supine position, the term below refers to higher Y coordinates.

junction of the lung with the ribs (near the sternum) determines $A_y$. The Y coordinates of these landmarks have been chosen in the mentioned position for the following reasons:

1. Placing the landmarks too close to each other increases the fitting error. Considering that the slice thickness can be 5 mm, the "quantification error" of the Z coordinate of A and B is relatively big, therefore, this effect is minimized by selecting their Y coordinate as distant as possible.

2. A and B must be derived from a (visible) region of the lung that is not affected by atelectasis, which corresponds to the ventral zone above the coronal plane defined by the Z coordinate of the carina[12].

3. Keeping the distance between all landmarks approximately equal, independently of the sagittal frame being analyzed yields an interpolation that changes smoothly from slice to slice. This behavior can be observed in figure 4.16 (a) and (b).



(a)           (b)
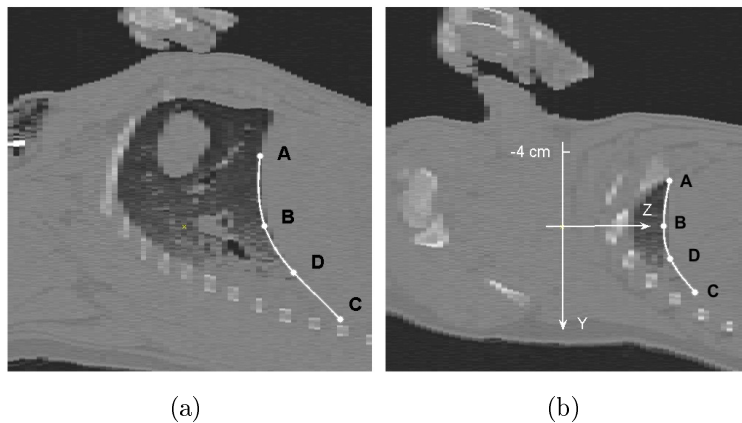
Figure 4.16: Example of the automatic BL segmentation and positioning of landmarks A, B, C and D. (a) Sagittal plane near the heart center, about 3.5 cm to the left of the spine. (b) Sagittal plane on the left of the heart, about 8 cm to the left of the spine. In this cross-sectional image, landmark A lies below -4 cm, and its Y coordinate is set to the ventral junction of the lung with the ribs.

---

[12]Extreme cases of induced atelectasis have been observed where the ventral zone of the lung above the coronal plane defined by the Z coordinate of the carina was affected by the lavage. In such exceptional situations, this approach is not applicable.

## 4.6.2   Dorsal landmark C

The lowest point of the lung in each sagittal plane is identified with landmark C and the curve resulting after connecting the C points of all frames is referred to as the lung-edge (LE) curve (figure 4.17 (a)). In atelectatic lungs subject to low PEEP levels, the position of C (and consequently the LE curve) cannot be immediately identified in the CT image. Therefore, a standarized or reference LE curve has been built beforehand with the training set. However, the size and shape of this reference curve does not describe accurately the LE curve of the atelectatic lung being analyzed. In consequence, it must be adjusted to this lung in order to provide the coordinates of landmark C in each sagittal plane.

More specifically, the landmarks J, K, R, L (see below) of a particular lung determine the position of the corresponding control points of the reference LE curve[13], which in turn adjusts its shape to this lung. For that purpose, the reference curve is subject to a linear deformation in coordinates X and Z, and an elastic deformation in Y according to the rib cage.

Figure 4.17 (b) shows a reference LE curve created with the LE curves of the training set (appendix B.1), which were manually segmented. After identification of the corresponding landmarks J, K, R, L, the curves have been co-registered, resampled in order for all of them to have the same number of points, and finally averaged.

Landmarks J and K (figure 4.17 (b)) are the extreme left and right points of the lung, i.e. the points where the lungs reach their maximal width. They can be recognized independently of the atelectasis degree, as they lie above the Y coordinate of the carina, in the ventral region that is always visible.

Landmarks L and R are the lowest points of the left and right lung. They cannot be identified in the atelectatic lung parenchyma, therefore, additional anatomical information is used to estimate their position. The bronchial tree, an anatomical structure visible in the CT image independently of the

---

[13]The control points of the LE curve are derived from their corresponding landmarks identified in the training set of images.
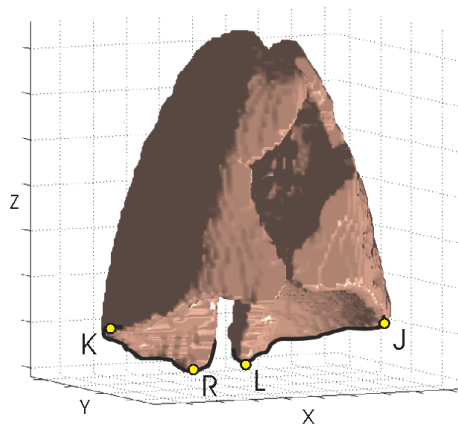
(a)
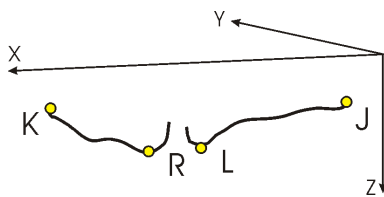


(b)
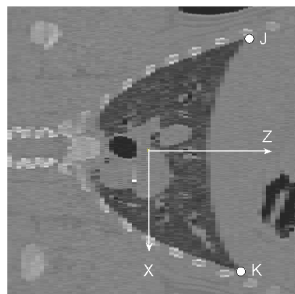


(c)

Figure 4.17: Example of LE curve. (a) The black line shows the LE curve and landmarks J, K, L, R of a particular animal. (b) Reference LE curve and control points J, K, L, R. After elastic deformation, this curve defines the position of landmarks C in each frame. (c) J and K landmarks identified in the coronal plane.
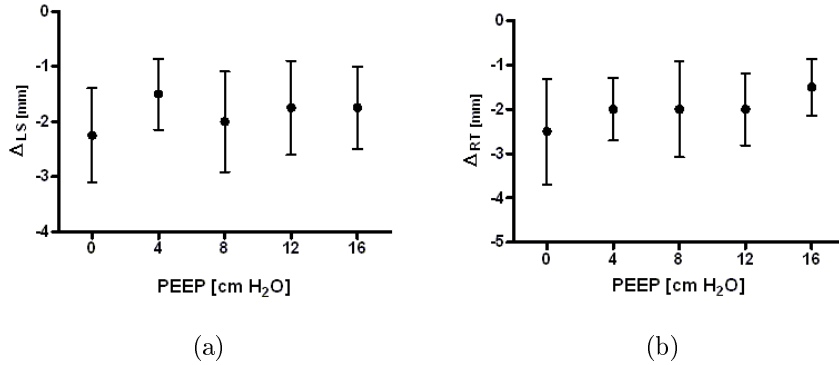
Figure 4.18: Estimation of the lowest point of the lung with the help of the bronchial tree. (a) Distance between the lowest point of the left lung $S$ and the lowest end of the left half of the bronchial tree $L$. (b) Idem right lung. The low interindividual variability (below 2 mm) observed confirms landmark $S$ and $T$ as the best estimators of $L$ and $R$. The measurements were performed on 1 mm slice thickness.

degree of atelectasis, provides the information required to assess the position of these landmarks.

As illustrated in figure 4.18, the lowest visible point of the left and right bronchial tree (S and T) show a high correlation with L and R respectively, therefore, an algorithm capable of tracking the airways downwards in the dorsal basal region beyond the $12^{th}$ generation is necessary.

**Bronchial Tree Tracking**

Many approaches have been developed to segment the tracheo-bronchial tree in thin-slice CT [27, 29, 11] that achieve high accuracy, but none of them reaches the $12^{th}$ generation. Moreover, they are not designed to work properly on lungs with atelectasis. However, the identification of S and T does not demand an accurate segmentation of the bronchi, but simply an algorithm capable of following the airways downwards until their deepest extreme. A simple but efficient approach to find the mentioned S and T landmarks is presented in section 3.5.3. The *Bronchial Tree Tracking* algorithm processes the transversal planes of the 3D CT data sequentially beginning with a slice

71

about 45 mm below the carina (figure 4.19 (a)) and returns the frame index where the lower end of the bronchi us was detected (figure 4.19 (c)). A detailed description of the parameter setting of the algorithm can be found in appendix A.2.



|       |       |       |
|:-----:|:-----:|:-----:|
| (a)   | (b)   | (c)   |
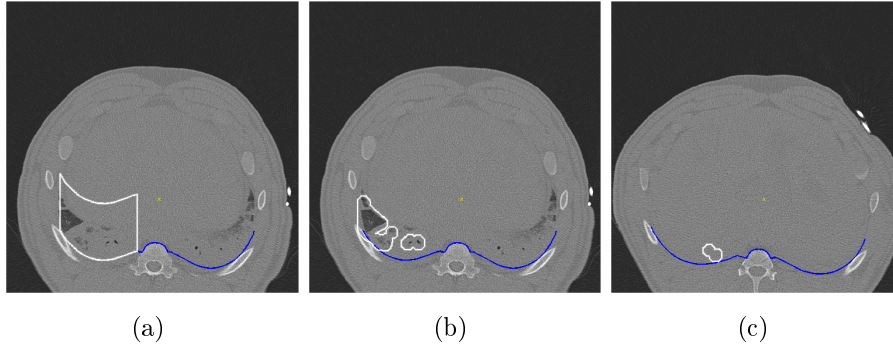
Figure 4.19: Bronchial tree tracking example in the right lung. (a) Start transversal slice selected for the tracking (circa 4.5 cm below the carina). The right ROI is defined by the ribs. (b) Seed resulting from the segmentation of the voxels inside the ROI below -300 HU after dilation. (c) Last slice where the bronchus has been detected (15 cm below the carina).

In a 5 mm slice thickness CT image it has been observed due to partial-volume effects that the small bronchi near the lung base are "merged" with the lung parenchyma with atelectasis about 2 cm before their inferior extreme. Therefore, the tracking algorithm must affect the found position of S and T by a correction term of 2 cm when it detects a slice thickness of 5 mm.

### 4.6.3 Landmark D

The position of landmark D is estimated by the diaphragm model based on the coordinates of B and C (equations 4.1 and 4.2).

$$D_y(p) = \frac{B_y(p) + C_y(p)}{2} \tag{4.1}$$

$$D_z(p) = \alpha \cdot (B_z(p) + C_z(p)) - \beta \tag{4.2}$$

With $\alpha = 0.48$ and $\beta = 7.4$ mm, where the subindices $y$ and $z$ identify the corresponding coordinates of the landmarks B, C and D, which in turn introduce the dependency of D with the pressure $p$ in the model.

The values of $\alpha$ and $\beta$ have been found empirically in order to adjust the curvature of the interpolating curve employed for the automatic segmentation of the diaphragm (figure 4.16) to the manually segmented base of the lung (figure 4.15).

### 4.6.4   Landmarks interpolation

Having positioned the four landmarks A, B, C and D in the sagittal plane, they are interpolated in the same plane with a cubic spline (polynomial form) with knot sequence $\{A, B, D, C\}$. The not-a-knot end condition is used, thus forcing the first and second polynomial piece of the interpolant to coincide, as well as the second-to-last and the last polynomial piece. Four landmarks have been chosen for the interpolation because this is the minimal number of knots required to fit accurately the BL in the sagittal plane.

**Drawbacks of the model:** This approach is applicable for those cases when the atelectasis affects the lung below the coronal plane defined by the Y coordinate of the carina. Otherwise it is not possible to identify the landmark B.

The LE curve has been "learned" from the lungs of the training set. Although it is elastically deformed to match the particular characteristics of the lung being analyzed, the position of C derived from the LE is subject to errors due to large inter individual variability that degrade the diaphragm segmentation results.

## 4.7   Thoracic Aorta segmentation

This section introduces an algorithm to segment the thoracic aorta (half of the descending aorta above the diaphragm) in CT images of atelectatic lungs. The procedure relies on anatomical characteristics that relate the

position and size of the artery to that of the vertebrae, carina and trachea, accurately segmented in earlier steps.

In the transversal plane CT image, the aorta filled with blood looks like an homogeneous gray disk. Since this property is minimally affected by the inter and intra individual variability, segmenting the vessel with the template matching algorithm using as convolution mask (template) a disk is a suitable approach. However, the high degree of atelectasis in the dorsal region produces large areas, in this zone of the image, with homogeneous gray level that impede the algorithm to precisely determine the position of the artery. To overcome this difficulty, the region where the template matching should operate is restricted by a ROI to the area where the aorta is likely to be found. The size and position of this ROI is controlled by anatomical information previously acquired from the training set, as will be shown below.

Following the mentioned strategy, although gray level and texture of the aorta do not provide relevant information as they are hard to distinguish from the soft tissue of the diaphragm, heart and lung with atelectasis which usually surround the artery, small regions of the lungs and esophagus filled with air provide those darker pixels around the vessel that will be used to estimate the position of its center[14].

The anatomical observations listed below are derived from the animals of the training set. They provide the basis for defining the ROI in each transversal frame as well as for correcting potential segmentation errors later on.

1. The projection of the aorta on the coronal plane, i.e. its X coordinate, related to the vertebra landmarks shows a sinusoidal shape which is better described by a $4^{th}$ order polynomial (figure 4.20). Deviations between different animals have been observed but the "oscillating" nature of the shape is always present.

2. The aorta lies contiguous to the spine and ribs near the costo-vertebral articulation.

---

[14]Throughout this section, the center of the circle described by the aorta wall in a cross-sectional image of the transversal plane is referred to as the center of the aorta.

3. The diameter of the aorta correlates with the diameter of the trachea.

Figure 4.20 shows the X position of the aorta relative to the X coordinates of the vertebra landmark (ordinate) and relative to the Z coordinate of the carina (abscissa). For clarity, only 3 curves are plotted. (note that the size of all pigs was similar).
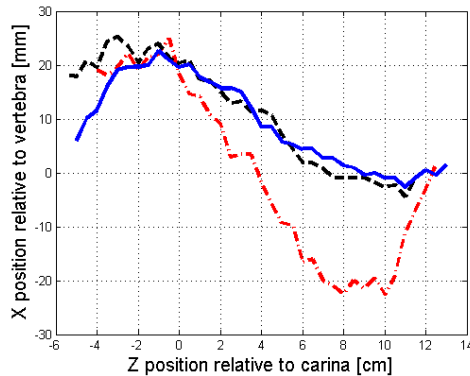


Figure 4.20: Examples of the aorta center relative to the vertebra position (ordinate) and carina (abscissa) measured in the transversal CT images.

## 4.7.1 Segmentation algorithm

Having described the anatomical considerations involved in the aorta segmentation, the algorithm that uses them in order to assess the position and diameter of the artery in the volume CT data it will be explained. Figure 4.21 illustrates the flow chart of the segmentation procedure.

The template matching algorithm operates in the transversal plane and requires the shape of the aorta in this plane as convolution mask. This is defined as the "ideal" cross-sectional image of the aorta, consisting of a square background (pixels set to 0) with a disk centered on it (pixels set to 1) as shown in figure 4.22. Since the actual diameter of the aorta, i.e. the diameter of the disk, is unknown, it is derived from the trachea[15] in the first step of the segmentation algorithm. This diameter is referred to as TD.

---

[15]The contours of the trachea in each frame have been previously stored by the airways segmentation algorithm and its diameter is indirectly estimated from its area.
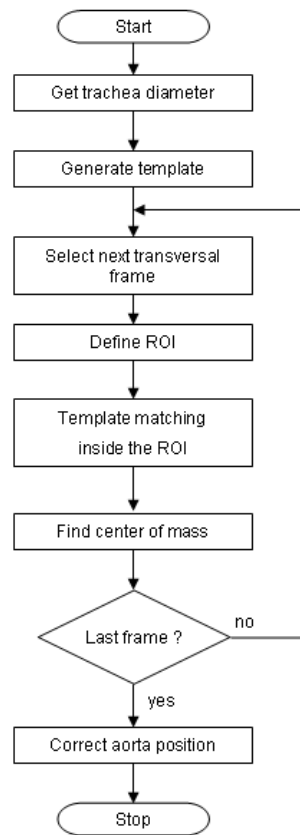
Figure 4.21: Aorta segmentation flow chart.
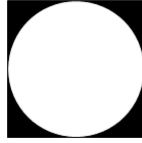
Figure 4.22: Convolution mask used to filter the ROI. The black pixels outside the disk are set to 0, the white pixels inside are set to 1.

At this point a loop starts that processes each transversal frame and searches the aorta inside a ROI (figure 4.25(a,b,c)) which is dynamically defined as follows: the lower border is given by the rib landmarks interpolated in the transversal plane (figure 4.10 (e)). The upper border replicates the lower border but is shifted TD upwards, the left and right borders are taken from the maximum deviations of the aorta center, relative to the vertebra position, observed during the previously taken measurements (figure 4.20 (a)) augmented TD/2 in both directions.

The convolution of the template with the ROI of the CT image produces a new filtered image (figure 4.25(d,e,f)) from which the center of the aorta will be estimated. Assuming that the gray level of the pixels inside the aorta is higher than the gray level of the remaining pixels of the ROI and that the real diameter of the aorta is exactly the diameter of the template disk, the filtered image can be expected to reach a maximum in the center of the aorta, where the ROI best correlates with the convolution mask. Unfortunately, in reality this is not always the case. Indeed, the gray level of some few pixels outside the aorta is lower than that of the pixels inside the aorta and the mentioned diameters are not exactly the same (recall that the actual diameter is unknown), therefore, the filtered image has a broad region of maxima[16] where the center of the aorta is not definite. Hence, the "center of mass" of this region must be determined and its coordinates will be considered to be the center of the aorta.

---

[16]The absolute maximum inside this region does not coincide with the center of the aorta due to noise in the filtered image.

The region of maxima is extracted from the filtered image by keeping only those pixels with a gray level above 99% of the absolute maximum gray level (figure 4.23(b)).
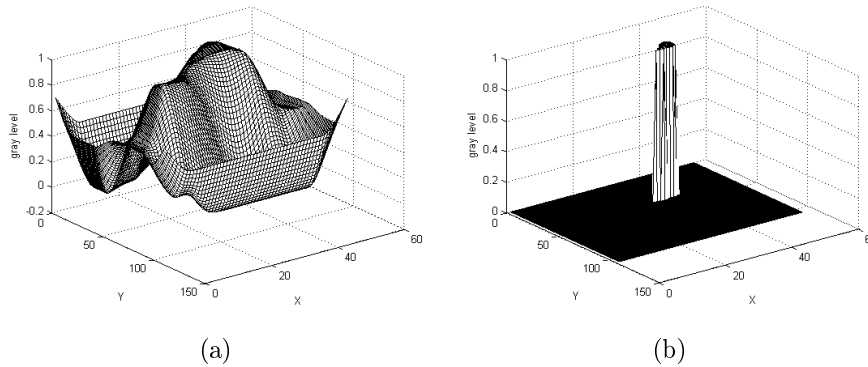


Figure 4.23: Extraction of the region of maxima. (a) Filtered image. (b) Region of maxima.

A drawback of this approach is that the presence of bright pixels outside the aorta but inside the ROI may displace the maxima of the filtered image from the actual center of the aorta. Probe heads inserted in the esophagus are an example of this (figure 4.24(a)). The mentioned problem arises in few slices and can not be predicted (probes are not always used in all experiments and their location is unknown). Figure 4.24(b) illustrates an example of the X coordinate of the aorta for each frame computed with the center of mass of the region of maxima. The influence of the probe head in the displacement of the aorta center can be observed in the slices between -2 and -4 cm above the carina. They appear like outliers of the actual X position.

(a)             (b)
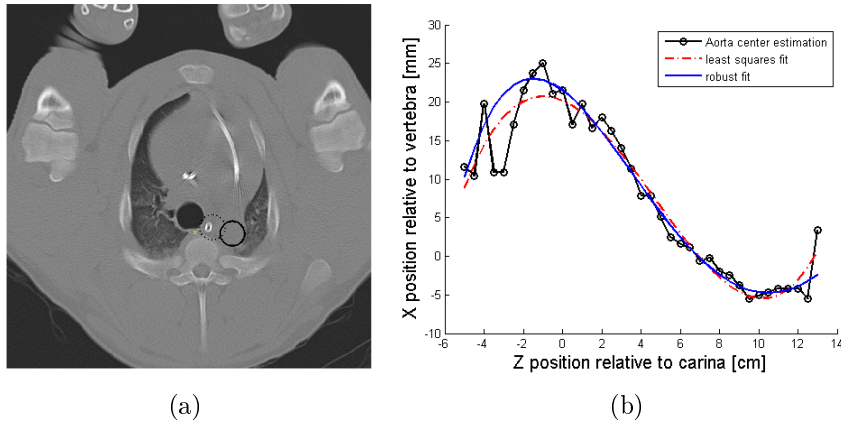
Figure 4.24: Aorta center correction. (a) The extremely high gray level of the probe head in the esophagus produces the maxima in the filtered image outside the aorta, leading to a wrong aorta positioning (dotted line circle). The solid line circle shows the corrected position of the aorta after the robust fit. (b) Aorta center relative to carina and vertebra. The outliers are ignored by the robust fit algorithm (solid line). The dashed line shows the fit using an ordinary least-squares regression. The outlier (-3, 11), i.e. 3 cm above the carina and 11 mm to the left of the vertebra corresponds to the dotted line circle shown in (a).

## Segmentation Refinement

The last step in the aorta segmentation is the identification and correction of the erroneous aorta center estimations. Taking into account that the position of the aorta changes smoothly from slice to slice, and considering points 1. and 2. made under the anatomical observations, the X coordinate of the aorta is corrected by a robust fit algorithm (section 3.5.2) which employs a $4^{th}$ order polynomial to identify and remove outliers, keeping and fitting only those assessments of the aorta center that are anatomically meaningful (figure 4.24).
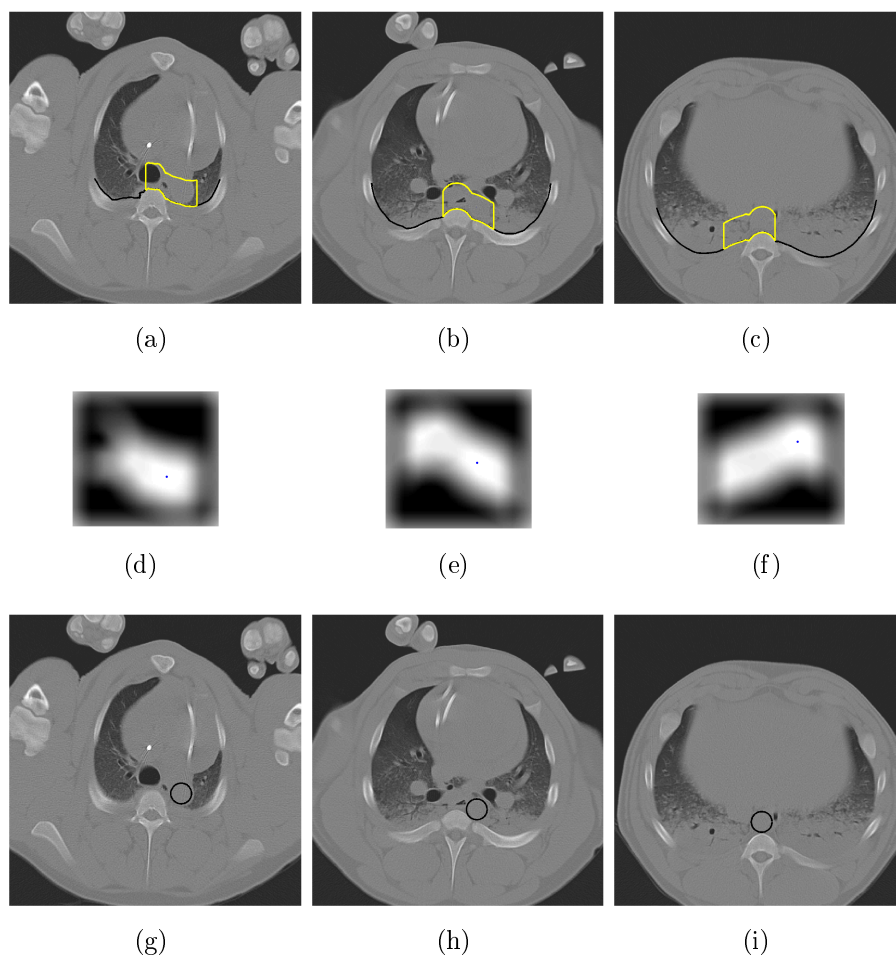
Figure 4.25: Aorta segmentation. Top row: 2D-ROI in the transversal plane where the aorta will be looked for. Middle row: convolution of the CT image inside the ROI with the filter template. Bottom row: Aorta segmentation. Left column: apical region; the border between the aorta and the heart above it is not visible. Middle column: helium region: the dorsal zone of the lung with atelectasis, the aorta and the diaphragm above it have almost the same gray level and texture. The esophagus (seen as a dark spot in the middle of the ROI) bounds the aorta on the right. Right column: justa diaphragm region; small regions of the lungs filled with air, darker than the aorta, are used to find its position.

The values assigned to the parameters of the robust fit algorithm are detailed in appendix A.4.

Based on the second property of the model, the Y coordinate of the aorta is adjusted if necessary. In this case, the ROI defines the upper and lower limits allowed. Centered in the current Y coordinate and the corrected X coordinate, a circle with diameter TD is positioned in the current frame. If this circle is not completely contained in the ROI, (i.e. the contour of the ROI cuts across the circle) the Y position must be modified as much as necessary until the circle lies inside the ROI, satisfying the observation that the aorta is expected to lie contiguously to the spine and ribs near the costo-vertebral articulation.

This concludes the aorta segmentation process.

A preliminary approach intended to smooth the changes of the aorta center along adjacent frames using 3D interpolation have shown erroneous results as it ignores the constraints established by the anatomical observations. It has been observed in some cases that the artery was placed below the limits of the bones.

## 4.8   Stomach segmentation

Although the stomach is placed in the ventral cavity below the diaphragm, in some animals this organ is visible in the transversal CT images that correspond to the base of the lung. Since some dark regions of the stomach have CT numbers similar to the healthy lung parenchyma, they need to be identified and excluded from the lung segmentation.

Figure 4.26 illustrates a portion of the stomach that appears like a black region in the transversal, sagittal and coronal plane.

<div align="center">(a)          (b)          (c)</div>
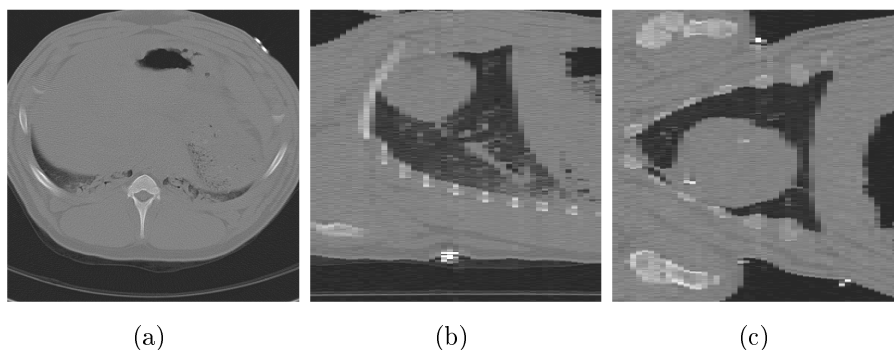
Figure 4.26: Presence of the stomach in the zone of the lung base. (a) Transversal plane. (b) Sagittal plane. (c) Coronal plane.

As the stomach does not delimit the lungs its precise segmentation is not required. Instead, only those regions of the stomach filled with gas have to be recognized. In order to do so, no further anatomical information than its approximate position and CT number is needed.

The approach followed to identify the black regions of the stomach is based on the *volume growing* algorithm (section 3.5.3), the same which has been employed for the bronchial tree tracking (section 4.6.2). The procedure starts with the last transversal frame of the volume data. There, a rectangular ROI is defined which contains the whole transversal plane above the carina, thus assuring that the dark regions of the stomach will be included in the 2D ROI. This algorithm scans the transversal frames upwards appending the mentioned dark areas to the 3D segmentation of the stomach if the connectivity between them is verified. Finally, the identified volume is stored for further use in the last step of the lung segmentation.

Detailed information of the parameter settings of the volume growing algorithm for the stomach segmentation is given in appendix A.3.

## 4.9   Lung segmentation

Having analyzed the anatomical structures related to the lung, it is now feasible to proceed with the lung segmentation.

Since the cross-sectional image of the lung in the transversal plane changes considerably from the top to the bottom of the thorax, and different anatomical structures participate in the composition of the lung shape depending on the frame being analyzed, four zones of the lung have been defined in order to facilitate the operation of the segmentation procedure and improve its results. These zones are: (I) cranial, (II) apical superior, (III) apical inferior and (IV) caudal.

The algorithm begins with the identification of the lung parenchyma not affected by the atelectasis as shown in figure 4.28. This is done with the help of a thresholding segmentation as introduced in [22, 41]. Although the lung parenchyma is characterized by a CT number between -200 and -500 HU [25], it has been preferred to ignore the lower limit (-500 HU) for its segmentation in order to avoid excluding the hyperventilated zones with gray level below -500 HU when the lungs are subject to PEEP levels above 4 cm $H_2O$. This has the negative side effect that the regions identified contain the airways and stomach (with CT numbers lower than -500 HU). Therefore, they must be removed from the final segmentation of the lung, as will be shown later on.

The rest of this section describes the characteristics of the atelectatic lung in each zone, the information provided by the anatomical structures already segmented and the way it is managed by the segmentation algorithm to compose the edge of the lung in each transversal frame.

### Craneal zone (I)

The craneal zone (figure 4.27 (a)-I, (b,c)) is comprised between the uppermost point of the lung and the transversal plane circa 7 cm above the carina. In this zone, two important observations can be made: a) The contour of the lung is not defined by the ribs and vertebrae in the dorsal region. b) The atelectasis is almost imperceptible because the liquid drains to lower zones
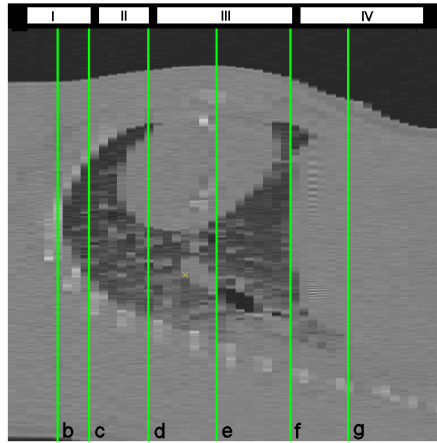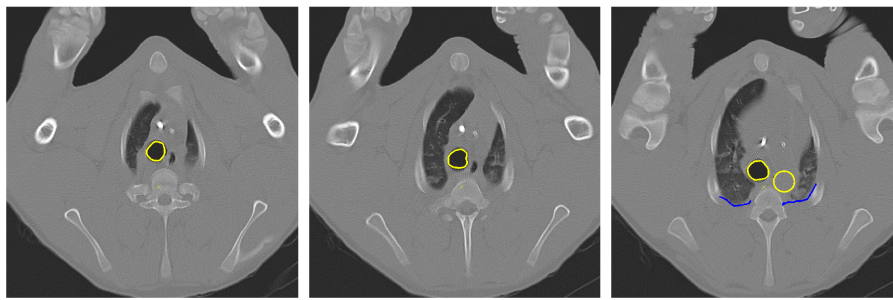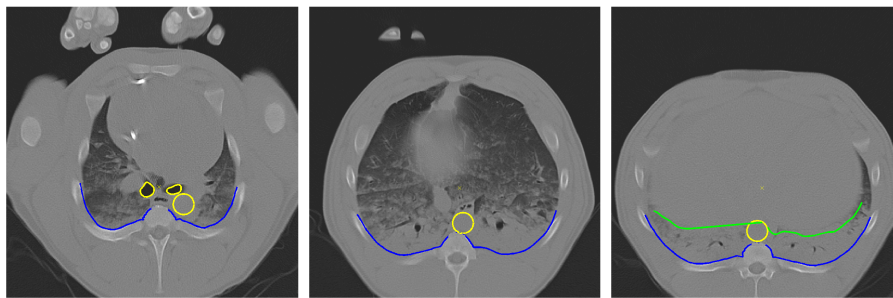
Figure 4.27: Zone-dependent lung segmentation. (a) Craneal (I), apical superior (II), apical inferior (III), caudal (IV). The transversal frames (b) to (g) correspond to the vertical lines of the sagittal view (a).

due to the gravity force. Therefore, the segmentation of the lung in this zone achieved by a thresholding algorithm operating on the gray level of the CT image describes the lung edge more accurately than the ribs.

## Apical superior zone (II)

The apical superior zone (figure 4.27 (a)-II, (d)) comprises the region between the transversal planes situated at 7 cm and 2.5 cm above the carina approximately. In this zone, the dependent region of the lung, partially affected by the atelectasis, is limited by the ribs. The already segmented lung parenchyma visible in the CT image is therefore extended downwards up to the ribs curve with the algorithm *ModifyContour* (section 3.5.4). The result of this operation is a lung contour that incorporates lung parenchyma not identifiable in the CT image, but, depending on the position of the transversal plane, parts of the aorta (section 4.7) may be included in the lung segmentation as well, which have to be removed later on.

## Apical inferior zone (III)

The apical inferior zone (figure 4.27 (a)-III, (e,f)) comprises the region between the transversal planes situated 2.5 cm above the carina and the uppermost point of the diaphragm. As the transversal section of the lung approaches the diaphragm, the impact of the atelectasis becomes more noticeable in the dorsal zone. Like in zone II, the bone profiles therefore provide the border of the lungs in the dependent region. Additionally, a portion of the vertebra contour is appended to the ribs curve to better match the lung anatomy as shown in figure 4.27 (e, f, g). Then the contour of the lung parenchyma identified in the CT image is extended downwards up to the ribs-vertebra curve by *ModifyContour* and, in a last step, the aorta is excluded from the lung segmentation.

The vena cava and other vessels parallel to the bronchi also ought to be removed from the lung segmentation. However, they have not been considered in this work and consequently constitute the main error source (as will be shown in chapter 5).
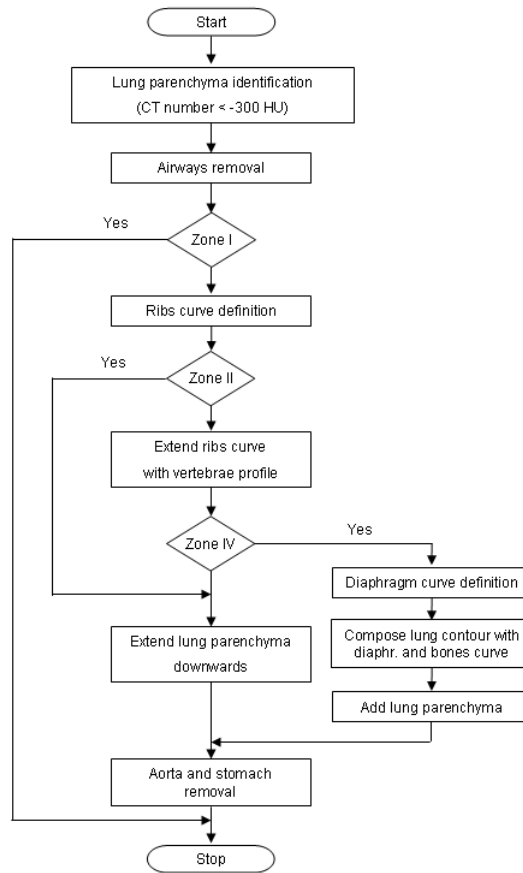
Figure 4.28: Lung segmentation procedure.

## Caudal zone (IV)

The caudal zone (figure 4.27 (a)-IV, (g)) lies below the transversal plane defined by the uppermost point of the diaphragm. Typically, this zone is strongly affected by the atelectasis and the small "spots" of lung parenchyma identified in the CT image can not be used to define the ventral border of the lung. Therefore, this is assessed by the diaphragm dome (section 4.6). As shown in the left branch of the flow chart (figure 4.28) the upper and lower edge of the lung are defined by the diaphragm and ribs curve respectively, which are connected to each other to define a contour. The area of this contour is complemented with the lung parenchyma previously identified in order to define the lung segmentation in each transversal frame.

The flow chart illustrated in figure 4.28 summarizes the segmentation procedure according to the zone where the transversal frame is situated. Although the lung is 2D segmented with a slice by slice approach, 3D information has been considered during the analysis of the anatomical structures involved in the lung segmentation (sections 4.4 to 4.8), thus improving the quality of the final result.

# Chapter 5

# Algorithms evaluation

In this chapter, the results of performance tests of the segmentation algorithm presented in this thesis are reported, after a brief outline of the methods used for the evaluation. A full description of the last topic is beyond the scope of this work and the interested reader can refer to [101, 102] for additional details.

The evaluation of the segmentation algorithms is not only important for the selection of the most appropriate approach for a given application but also for tuning the parameters of the algorithm to optimize its performance. However, the problem of objective evaluation of the segmentation quality is far from being solved. From the medical point of view, the quality of a segmentation algorithm can be evaluated according to subjective criteria which are not embedded in the metrics relevant for image segmentation theory. Therefore, in the following sections the impact of the segmentation errors in the physiological measurements derived from the automatic segmentation of the lung will be considered together with conventional approaches for the assessment of goodness of segmentation.

## 5.1  Evaluation of image segmentation

Evaluation methods are mainly divided into two groups: analytical methods and empirical methods [102]. The first intrinsically examine the segmenta-

tion algorithm by analyzing its principles and properties [103, 104]. Empirical methods, on the other hand, indirectly judge the segmentation algorithm by applying it to test images and measuring the quality of the segmentation results. Empirical methods are further classified into goodness methods and discrepancy methods (also known as supervised evaluation). Empirical goodness methods evaluate the different algorithms by computing a goodness measure based on the segmented image and they do not rely on a reference segmentation. Entropy [103], colour uniformity [104], region shape [49], intraregion contrast [105], intraregion uniformity [106] among others are some examples of goodness measures. Empirical discrepancy methods measure the disparity between an automatically segmented image and a reference segmentation, also called gold standard, both derived from the same source image. However, reference (manual) segmentations do not guarantee a perfect truth model since an operator's performance can be flawed. A study aimed at assessing the relative accuracy of subjective brain volume evaluation analyzed twice by the same radiologist (before and after a time lap of 3 months), showed a difference of up to 4.9 %, and 87.8 % overlapping. A comparison between different radiologists reported a similarity of the result between 64 and 87 % [93]. An effort to overcome this drawback have led to the development of physical phantoms [107] and computational phantoms [108] but these are merely simplified models that do not replicate the richness of detail and inter individual variability observed in the real objects of study.

The methods adopted for the evaluation in the present work of lung segmentation algorithms belong to the group of empirical discrepancy methods. Besides the well established Dice coefficient [109], additional evaluation coefficients are introduced by the author to provide a better insight into the characteristics of the segmentation errors produced by the algorithm.

The Dice coefficient measures the similarity between the regions defined by the automatic $S_A$ and reference $S_R$ segmentations. It is defined as twice the number of the overlapped pixels (intersection) between both regions divided by the sum of the number of pixels of each region.

$$C_{Dice} = \frac{2 \cdot \mid S_R \cap S_A \mid}{\mid S_R \mid + \mid S_A \mid} \qquad (5.1)$$

This coefficient provides an intuitive measure of the segmentation quality between 0 (no match at all) and 1 (perfect match). However, it does not distinguish between errors due to over segmentation (i.e. the automatic segmentation includes pixels that are not part of the reference segmentation) and under segmentation (i.e. some pixels present in the reference segmentation have been excluded from the automatic segmentation). The identification of over and under segmentation and their localization in the lung is of great interest from the medical point of view in order to assess the gravity of the errors implicated in the computation of the lung ventilation.

For example, when the base of the lung is completely invisible in the CT image due to atelectasis, over and under segmentation are not critical as long as the size of the automatically segmented area is similar to the size of the reference segmented area. In this case, the CT number of the lung parenchyma coincides with that of the diaphragm and the computed ventilation (based on the CT number of the pixels) of the wrong automatic segmentation will be similar to that corresponding to the reference segmentation (figure 5.1 (a)).

By contrast, over segmentation that includes a portion of the airways has an undesired negative effect on the computation of the lung ventilation. In this case, a region of the airways would be considered a hyper-ventilated compartment of the lung although it does not really belong to the lung parenchyma (figure 5.1 (b)). Similarly the vessels that run parallel to the principal bronchi, not segmented in this work, are wrongly included in the lung parenchyma and count as atelectatic tissue (figure 5.1 (c)). As will be shown in section 5.7, they constitute the largest over segmentation error source.

The coefficients of correct segmentation, over segmentation and under segmentation have been defined by the author as follows:

$$C_{corr} = \frac{\mid S_R \cap S_A \mid}{\mid S_R \mid} \qquad (5.2)$$
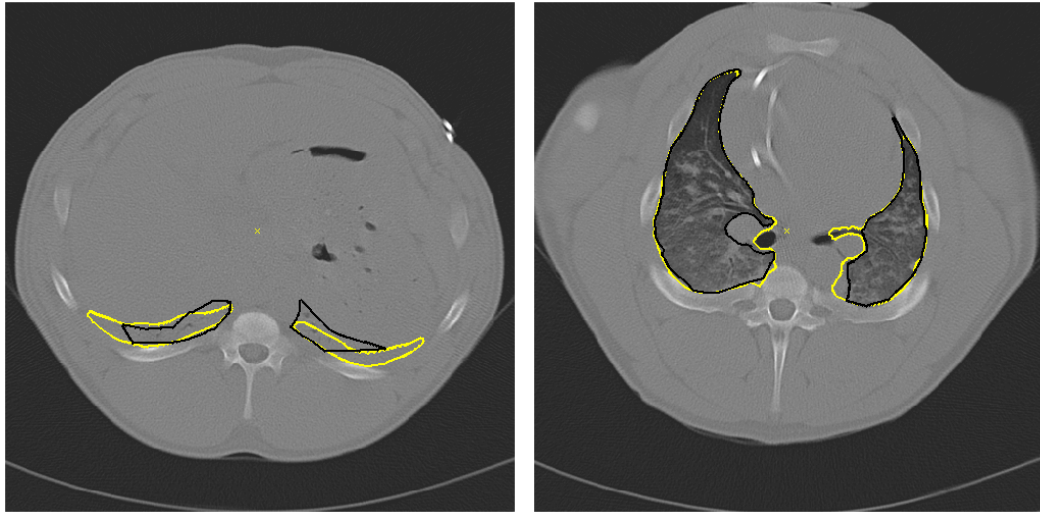
Figure 5.1: Examples of over and under segmentation. The black line corresponds to the reference (manual) segmentation and the yellow contour is the result of the automatic segmentation. (a) The impact of over and under segmentation on the computation of the ventilation in an atelectatic lung is negligible as long as the area of manual and automatic segmentation are similar. (b) Over segmentation of the right lung that includes a portion of the right bronchus. (c) Additional over segmentation errors of the lung are caused by the vessels parallel to the bronchi not segmented in the current approach.

$$C_{over} = \frac{\mid S_A \mid - \mid S_R \cap S_A \mid}{\mid S_R \mid} = \frac{\mid S_A \setminus S_R \mid}{\mid S_R \mid} \qquad (5.3)$$

$$C_{under} = \frac{\mid S_R \mid - \mid S_R \cap S_A \mid}{\mid S_R \mid} = \frac{\mid S_R \setminus S_A \mid}{\mid S_R \mid} \qquad (5.4)$$

where $C_{corr}$ is the correct segmentation coefficient, $C_{over}$ is the over segmentation coefficient and $C_{under}$ is the under segmentation coefficient. It is worth noting that $C_{over}$ may be bigger than 1 if the over segmentation area is larger than the reference segmentation area used for normalization.

Since these coefficients employ an area for normalization, they tend to exaggerate segmentation errors when the reference area is small like in the base of the lung (figure 5.1 (a)). Contrary, segmentation errors are dissimulated when the reference area is large (figure 5.1 (c)).

A similar situation arises when the bias introduced by a segmentation procedure is being qualified by $C$ coefficients. Assuming that the automatic segmentation exceeds the reference segmentation in one pixel along each point of the reference contour, i.e. the automatic segmentation is equal to the reference segmentation dilated by one pixel. In this case, a coefficient that reports "1" meaning "one pixel oversegmentation" is desirable to quantify this kind of error, independently of the area and length of the reference contour.

For this aim, a second set of coefficients $C'_{over}$ and $C'_{under}$ have been introduced which differ from $C_{over}$ and $C_{under}$ in the denominator employed for normalization as shown in equations 5.5 and 5.6.

$$C'_{over} = \frac{\mid S_A \mid - \mid S_R \cap S_A \mid}{\mid S_{R^\star} \mid - \mid S_R \cap S_{R^\star} \mid} = \frac{\mid S_A \setminus S_R \mid}{\mid S_{R^\star} \setminus S_R \mid} \qquad (5.5)$$

$$C'_{under} = \frac{\mid S_R \mid - \mid S_R \cap S_A \mid}{\mid S_{R^\star} \mid - \mid S_R \cap S \mid} = \frac{\mid S_R \setminus S_A \mid}{\mid S_{R^\star} \setminus S_R \mid} \qquad (5.6)$$

With $S_{R*} = S_R \oplus StrEl$ where $StrEl$ is a disc structuring element with 1 pixel radius, i.e. $S_{R*}$ is the reference segmentation dilated by one pixel.

These coefficients allow a twofold interpretation. The denominator of equations 5.5 and 5.6 coincides with the length of the contour of the dilated

92

reference segmentation, therefore $C'_{over}$ and $C'_{under}$ can be regarded as the over and under segmentation areas normalized by the length of such a contour.

For the evaluation of the ribs segmentation, where one portion of the lung contour is described by the curve defined by the ribs, the over and under segmentation coefficients, $C"_{over}$ and $C"_{under}$, have been defined in order to take into account strictly the segmentation errors along this curve. The same holds true for the evaluation of the diaphragm segmentation.

$C"_{over}$ and $C"_{under}$ coefficients are defined as follows:

$$C"_{over} = \frac{\mid S_A \setminus S_R \mid}{L_A} \tag{5.7}$$

$$C"_{under} = \frac{\mid S_R \setminus S_A \mid}{L_A} \tag{5.8}$$

where:

$\mid S_A \setminus S_R \mid$ is the ribs/diaphragm over segmentation (the yellow area in figures 5.2 (b, c)), i.e. the number of pixels that the automatic segmentation exceeds the manual segmentation along the ribs/diaphragm curve. These pixels actually belong to the lung parenchyma, therefore, the ribs/diaphragm over segmentation is a component of the lung under segmentation.

$\mid S_R \setminus S_A \mid$ is the ribs/diaphragm under segmentation (black area in figures 5.2 (b, c)).

$L_A$ is the length of the ribs/diaphragm curve used for the automatic segmentation of the lung.

These coefficients do not consider the errors produced in the region of the vertebrae, which are influenced by the aorta segmentation and other anatomical structures not segmented in this work.
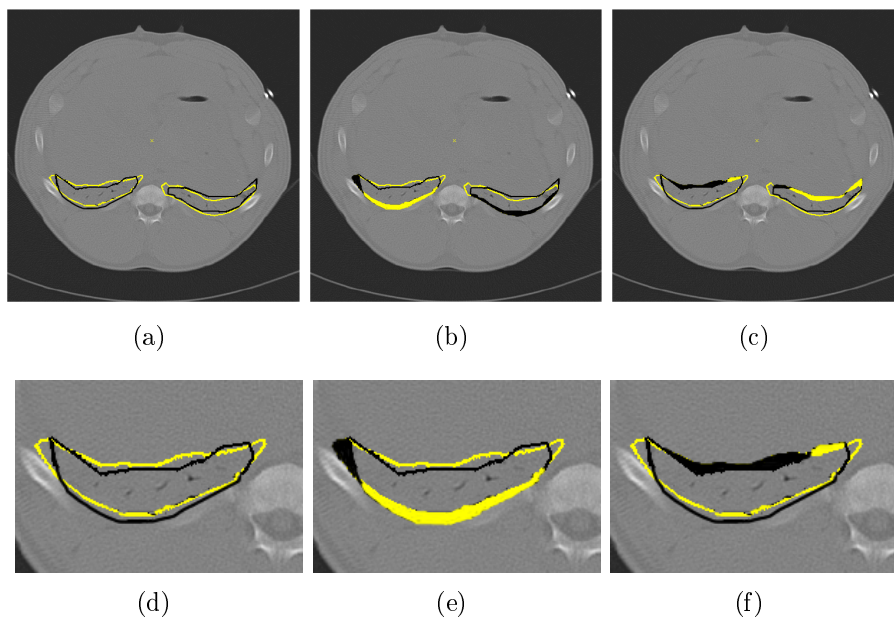
Figure 5.2: Diaphragm and ribs segmentation error examples. (a) Manual (black) vs. automatic (yellow) segmentation. (b) Ribs over segmentation (yellow area) and under segmentation (black area). (c) Diaphragm over segmentation (yellow area) and under segmentation (black area). An enlarged view of the right lung and its segmentation errors is depicted below each picture (images (d), (e) and (f))

## 5.2  Lung segmentation evaluation

A general notion of the quality of the lung segmentation algorithm is given by the correct segmentation, over segmenatation and under segmentation coefficients of the whole lung volume. Table 5.1 shows the values of the mentioned coefficients measured on the test set (appendix B.2).

| $C_{corr}$ | $C_{over}$ | $C_{under}$ |
|---|---|---|
| $97.04 \pm 0.90$ | $11.12 \pm 2.08$ | $2.97 \pm 0.90$ |

Table 5.1: Lung segmentation evaluation coefficients computed on the whole lung expressed as percentage of the mean value $\pm$ standard deviation.

Figure 5.3 illustrates the value of the Dice coefficient obtained for the lung segmentation of each transversal frame. The abscissa is labeled with the four zones distinguished during the segmentation process, i.e. cranial (I), apical superior (II), apical inferior (III) and base of the lung (IV). The black line corresponds to the mean value of the Dice coefficient measured from the test set, while the gray area represents ±1 standard deviation.
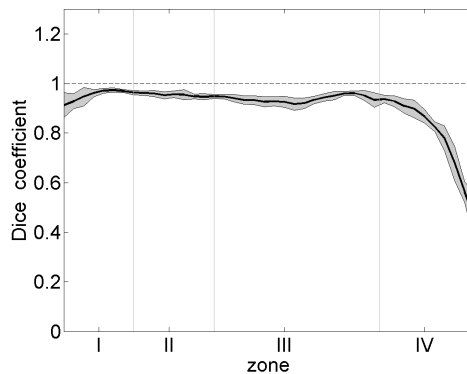


Figure 5.3: Dice coefficient of the lung segmentation computed locally for each transversal frame.

As can be observed, the Dice coefficient indicates that the performance of the segmentation algorithm degrades noticeably in zone IV which corresponds to the diaphragm. In spite of this, it is worth noting that when the slice position approaches the end of zone IV, the area of the lung is reduced up to less than 1 % of the area that can be found in zone III. This implies that segmentation errors that are large when considered at a single frame level, may indeed be very small when related to the total lung volume.

From the medical point of view, a global error description that expresses the percent of lung tissue (volume) that has been wrongly segmented is more relevant than an error coefficient that quantifies the over and under segmentation related to the segment size of a specific slice. This global error analysis is reported in table 5.2 which shows the contribution of the errors produced in each zone to the overall error in the whole lung.

| Zone | I | II | III | IV |
|---|---|---|---|---|
| Correct segm. | 4.73 ± 0.99 | 7.69 ± 0.19 | 68.60 ± 2.15 | 16.03 ± 2.29 |
| Over segm. | 0.24 ± 0.14 | 0.59 ± 0.05 | 7.24 ± 1.65 | 3.05 ± 0.61 |
| Under segm. | 0.06 ± 0.09 | 0.12 ± 0.06 | 1.54 ± 0.52 | 1.23 ± 0.52 |

Table 5.2: Correct, over and under segmenatation in each zone relative to the whole lung volume expressed as percentage of the mean value ± standard deviation.

The values obtained for $C_{corr}$, $C_{over}$ and $C_{under}$ coefficients computed locally to each transversal frame are illustrated in figure 5.4. They confirm the exponential degradation of the automatic segmentation towards the end of zone IV (base of the lung) anticipated by the Dice coefficient. Figure 5.4 (a) indicates a consistent overlapping (clearly above 90 %) between reference and automatic segmentation in zones I, II and III. The poor performance in the lower 2 cm of the lung (left most part of zone IV in figure 5.4) is attributed to inter individual variability. Notably, in this region the lung is usually not visible in the CT images employed in the test set and can only be guessed based on *a-priory* knowledge learned from the training set. The observation of the last frames of zone IV in figures 5.4 (a, b and c) suggest that the area of the wrongly segmented lung does not differ substantially from that of the reference segmentation. More specifically, if the last frame is considered, $C_{corr} \cong 0.4$, $C_{over} \cong 0.6$, $C_{under} \cong 0.6$ meaning that about 60 % of the lung area that was excluded from the automatic segmentation was "compensated" by an equivalent area included from the diaphragm (figure 5.1 (a)). This unacceptable image segmentation error, has, only a moderate impact in the computation of the lung ventilation as mentioned in section 5.1. Nonetheless, the low performance of the algorithm towards the end of zone IV, disqualifies it for use as a diagnostic tool for the base of the lung.
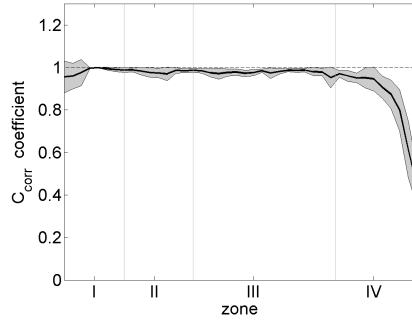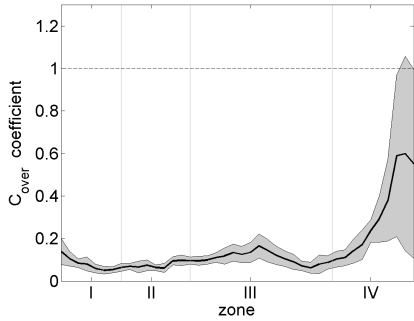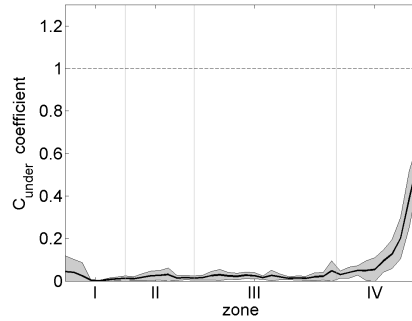
Figure 5.4: Lung segmentation evaluation by means of the $C_{corr}$, $C_{over}$ and $C_{under}$ coefficients computed locally to each transversal plane. (a) Correct segmentation. (b) Over segmentation. (c) Under segmentation.

Figure 5.5 (a) reveals a mean over segmentation error $C'_{over}$ (made by the algorithm) lower than one pixel in zones I and II. In zones III and IV, this error lies between 1.5 and 3 pixels . Figure 5.5 (b) shows that the mean under segmentation error $C'_{under}$ in zones I to III is lower than half a pixel. Even in most of zone IV, this error is smaller than 1 pixel.
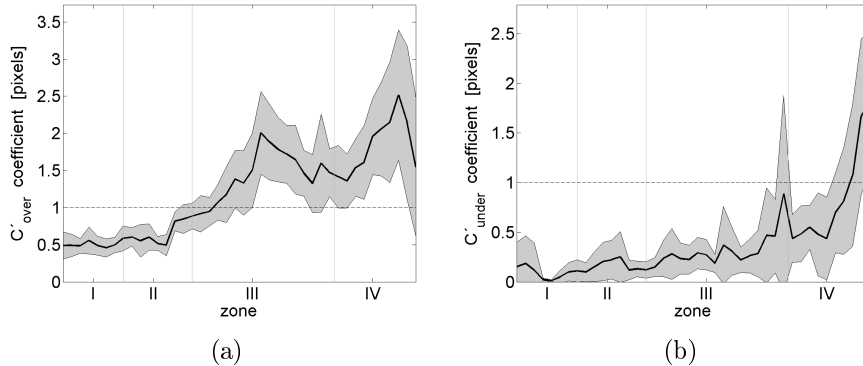
Figure 5.5: Lung segmentation evaluation by means of the $C'_{over}$ and $C'_{under}$ coefficients computed locally to each transversal plane. (a) Over segmentation. (b) Under segmentation.

Although the error analysis presented so far has shown the magnitude of the segmentation errors along the Z axis, this coefficients do not give information about how the error pixels are distributed along the lung contour of a transversal section. Therefore, in the next sections the contribution to the global error of the individual errors introduced by the anatomical structures involved in the lung segmentation will be examined.

## 5.3 Airways segmentation evaluation

Strictly speaking, the airways of the complete bronchial tree are not segmented. As explained in section 4.4, the goal of the airways segmentation algorithm was twofold. Firstly, it should reliably segment the trachea and principal bronchi in 5 mm slice CT images affected by the artifacts introduced by the endotracheal tube which distorted the shape of the trachea. Secondly, it identifies the carina in order to set the origin of the coordinate reference system.

The inter individual variability together with the different positions adopted by the ETT in different experiments result in a wide spectrum of artifacts which alter the shape of the trachea beyond the alternatives covered by the segmentation algorithm. This explains that the carina identification

failed in 2 out of 10 animals of the test set. However, after the carina position has been automatically (or manually) correctly identified, the segmentation algorithm has correctly[1] segmented the trachea and bronchi of all animals of the test set. Nonetheless, this can not be considered a highlight of this approach compared with more sophisticated methods [10, 27, 11][2] capable of segmenting up to the $6^{th}$ generation of the bronchial tree.

## 5.4   Ribs segmentation evaluation

The segmentation of the ribs in the dorsal region is one of the main contributions of this work considering the high accuracy reached by the algorithm. As explained in chapter 2, in zones II, III and IV the ribs define from the practical point of view, the contour of the lung in the dorsal region. The vertebrae are also related to the border of the lung. However, they do not contribute to the lung segmentation with the same quality offered by the ribs. Some examples of the segmentation errors due to the ribs and vertebrae are shown in figure 5.6.

---

[1]Since the algorithm has not been applied to a phantom, the segmentation is assumed to be correct when it coincides with the manual (reference) segmentation considered as a gold standard.

[2]These approaches require high resolution CT images for correct operation and cannot be employed for the airways segmentation of 5 mm slice thickness CT images.
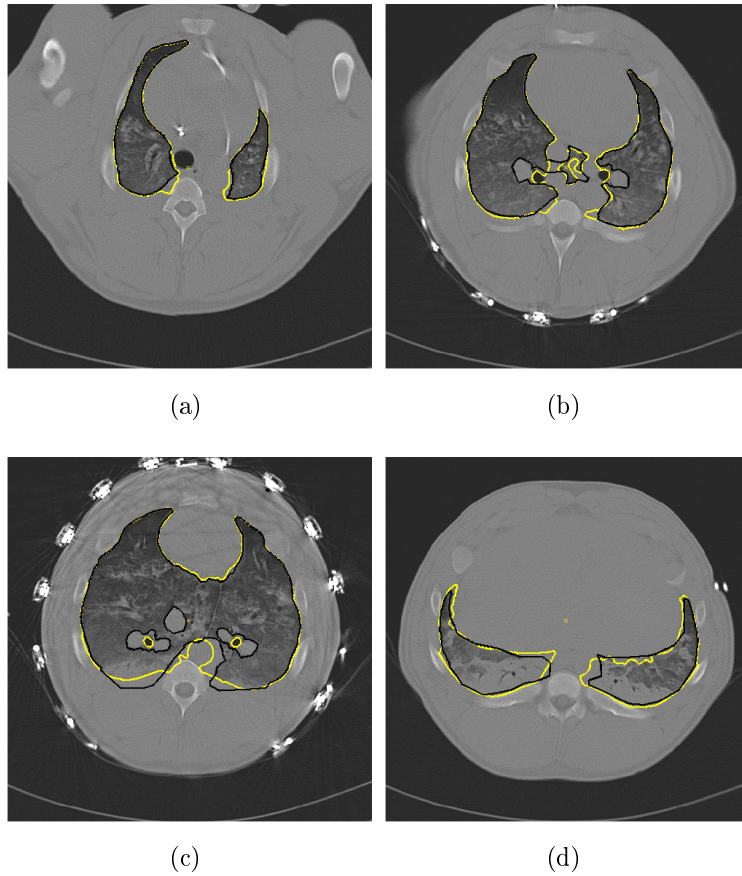
Figure 5.6: Automatic (yellow line) vs. manual (black line) ribs segmentation. (a, b) Lung over segmentation error near the vertebra. (c) Typical errors produced by the operator during the segmentation of the dependent zone of the lung. In this zone the automatic segmentation is usually better than the manual segmentation. (d) Example of diaphragm segmentation near the base of the lung.

The under and over segmentation error have been separately evaluated for the right and left ribs. Figure 5.7 shows the value obtained for $C"_{over}$ and $C"_{under}$ coefficients.

Segmentation errors produced when the lung border does not coincide with the vertebrae (figure 5.6 (a, b)) are not analyzed in this section. They are evaluated together with other error sources in section 5.7 under the heading *Others*.
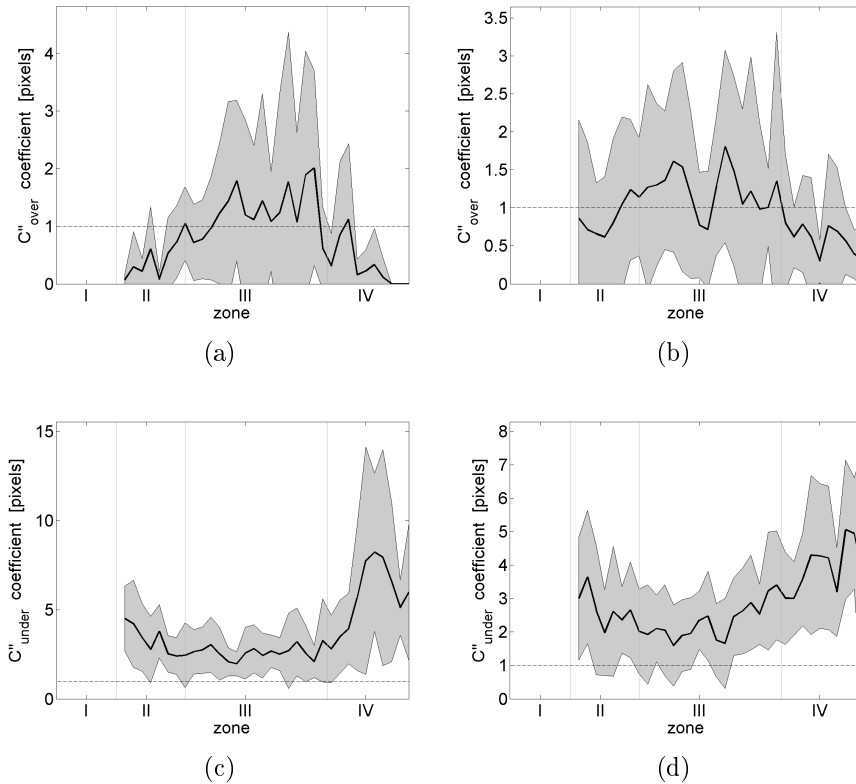
Figure 5.7: Ribs segmentation error. (a, c) Left ribs evaluation. (b, d) Right ribs evaluation.

Due to errors in the reference segmentation, the error evaluation does not reflect the true quality of the ribs segmentation algorithm. The automatic ribs segmentation in the dependent zones obtained with the presented strategy may be better than the manual segmentation done by an operator guided merely by the transversal plane image. This relies on the capability of processing the information available in the 3D data that is not accessible when a single slice is used for the manual segmentation.

## 5.5   Aorta segmentation evaluation

The aorta segmentation evaluation deserves a double analysis. From the medical point of view, it is important to assess the portion of lung parenchyma that has been erroneously identified as a part of the aorta. This aorta over

segmentation contributes to the under segmentation error of the lung. Figure 5.8 (a), (b) shows that the impact of the aorta over and under segmentation error is negligible. When the aorta segmentation is displaced from its actual position, the automatic segmentation of the lung contour, which is composed of a portion of the aorta wall, may include non-lung tissue (figures 5.9 (a), (b)). However, this is not the single error source that increases the lung over segmentation. Additional vessels and anatomical structures contiguous to the aorta that are not segmented in the present study are included in the automatic lung segmentation (figures 5.9 (c), (d)).
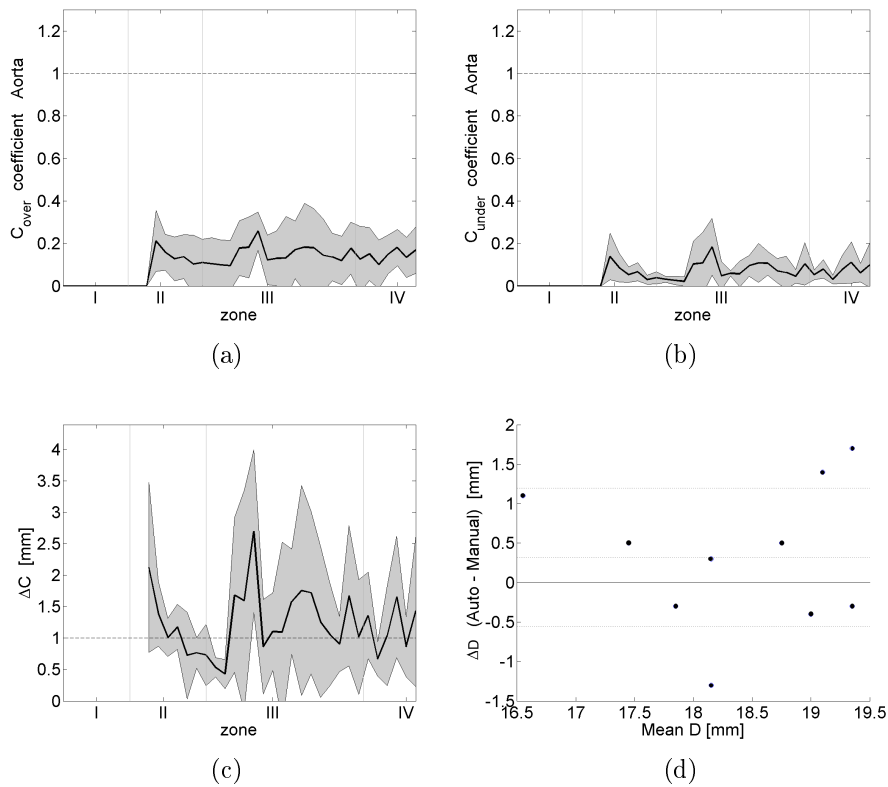


Figure 5.8: Aorta segmentation evaluation. Aorta over (a) and under (b) segmentation error normalized with the area of the aorta in the transversal plane. (c) Distance between the center of the reference and automatic segmentation of the aorta. (d) Bland-Altman plot of the aorta diameter.

|        |        |        |        |
|:------:|:------:|:------:|:------:|
| (a) | (b) | (c) | (d) |
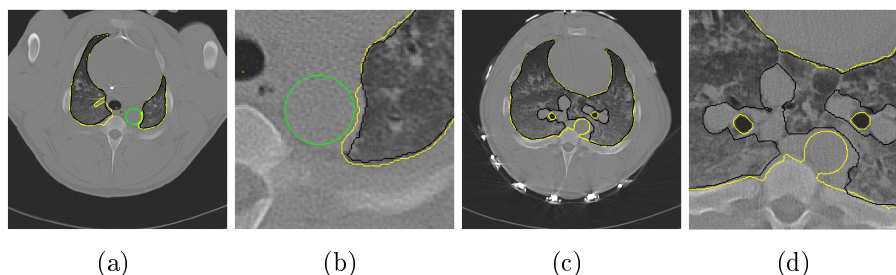
Figure 5.9: Lung under segmentation along the aorta wall. The black line corresponds to the reference segmentation. (a) Top and (c) bottom of zone III. (b) Enlarged region of image (a) around the aorta. (d) Enlarged region of image (c).

The second analysis of the automatic aorta segmentation abstracts from the medical implications and focuses on the evaluation of the segmentation algorithm itself. As explained in section 4.7, the cross-sectional image of the aorta in the transversal frame is approximated with a disk which is defined by its radius and its center. Figure 5.8 (c) shows the distance between the estimated and actual position of the aorta center for each trasnversal frame. As can be observed the misplacement of the center oscillates around a distance of 1.5 mm, less than 8% of the aorta diameter. Figure 5.8 (d) shows the erroneous assessment of the aorta diameter by means of a Bland-Altman plot. It must be taken into account that an exact reference measurement of the aorta position and radius was not possible due to the low contrast observed in the CT images of the atelectatic lungs.

## 5.6   Diaphragm segmentation evaluation

The diaphragm segmentation is extremely prone to inter individual variability. This leads to an inaccurate segmentation which becomes most evident in the lowest transversal frames. The lower the frame to be segmented, the less graphical information is available for the automatic segmentation, and the more information must be provided by the diaphragm model and the lung-diaphragm edge learned from the training set. Figure 5.10 illustrates

(a) (b) (c)
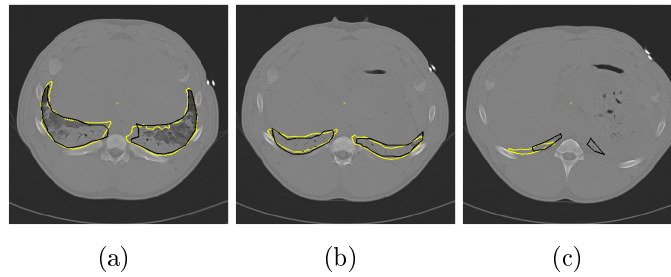
Figure 5.10: Representative example of the diaphragm segmentation. (a) Top, (b) middle, (c) bottom of zone IV. When the transversal slice approaches the bottom of the base of the lung, the area of the lung is smaller and the segmentation error increases.

an example of the lung segmentation on the top (a), middle (b), and bottom (c) of zone IV.

The over and under segmentation errors of the left and right halves of the diaphragm have been evaluated independently with the coefficients $C"_{over}$ and $C"_{under}$ as shown in figure 5.11.

As mentioned in section 5.1, the region of the lung above the vertebra (in the transversal plane) is not included in the diaphragm error evaluation.
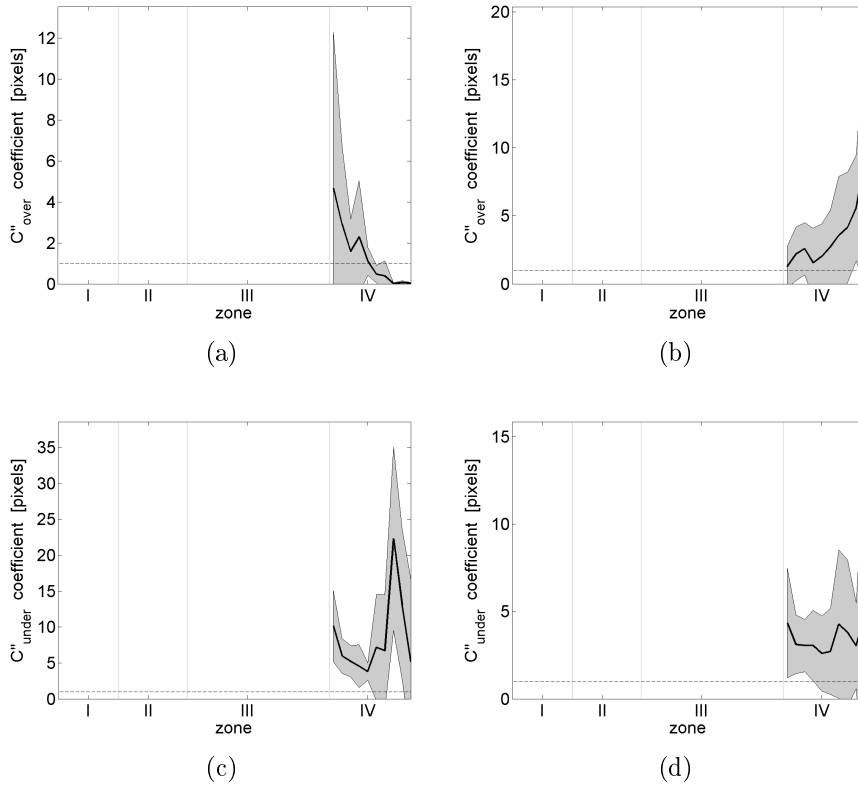
Figure 5.11: Diaphragm segmentation evaluation. (a, c) Left half of the diaphragm. (b, d) Right half of the diaphragm.

## 5.7 Global analysis

The analysis presented in sections 5.3 to 5.6 focuses on the evaluation of the under and over segmentation errors of the anatomical structures segmented by the algorithm computed in each single slice. This implies, as mentioned in section 5.2, that segmentation errors that are large when considered at a frame level where the lung contour is small, may in fact be negligible if compared to the whole lung volume.

In this section, an evaluation of the segmentation error of the previously mentioned anatomical structures normalized by the reference segmentation of the whole lung volume is presented. The differences between the reference and automatic segmentation due to the vessels that descend adjacent to the

bronchi, the vena cava, and other small anatomical structures not segmented by the algorithm result in segmentation errors that are treated separately under the term *others.*

Tables 5.3 and 5.4 show the over and under segmentation errors of the ribs, diaphragm, aorta and *others* in each zone related to the whole lung parenchyma. The last column reports the cumulative error due to each anatomical structure.

| Zone | I | II | III | IV | TOTAL |
|---|---|---|---|---|---|
| Ribs | - | 0.01 | 0.5 | 0.13 | 0.64 |
| Diaphragm | - | - | - | 0.53 | 0.53 |
| Aorta | - | 0.01 | 0.09 | 0.01 | 0.11 |
| Others | 0.06 | 0.11 | 0.95 | 0.57 | 1.69 |
| TOTAL | 0.06 | 0.13 | 1.54 | 1.24 | 2.97 |

Table 5.3: Over segmentation error (percentage) in each zone relative to the whole lung volume.

| Zone | I | II | III | IV | TOTAL |
|---|---|---|---|---|---|
| Ribs | - | 0.06 | 1.12 | 0.9 | 2.08 |
| Diaphragm | - | - | - | 0.88 | 0.88 |
| Aorta | - | 0.01 | 0.05 | 0.01 | 0.07 |
| Others | 0.24 | 0.52 | 6.07 | 1.26 | 8.09 |
| TOTAL | 0.24 | 0.59 | 7.24 | 3.05 | 11.12 |

Table 5.4: Under segmentation error (percentage) in each zone relative to the whole lung volume.

Figure 5.12 shows the proportion of the segmentation error of the anatomical structures related to the whole reference lung volume as indicated in the column labeled TOTAL in tables 5.3 and 5.4. This analysis reflects the fact that large segmentation errors have a moderate impact from the medical point of view.
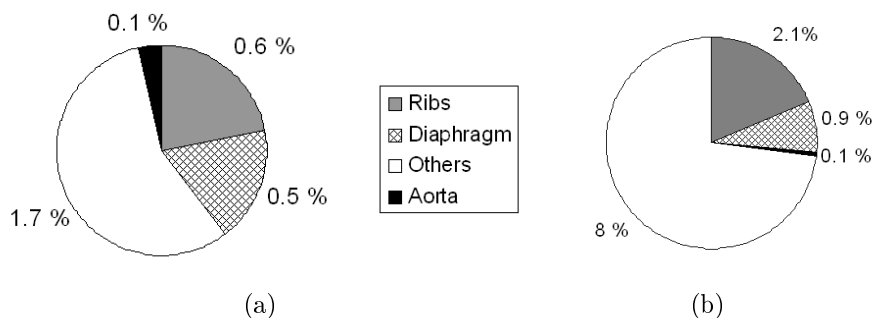
Figure 5.12: Distribution of the segmentation errors of the anatomical structures involved in the lung segmentation. (a) Under and and (b) over segmentation of the lung expressed as percent of the whole lung volume.

Bearing in mind that the largest discrepancies between the automatic and reference segmentation are due to the anatomical structures not analyzed in the current work (labelled *others*), they should not be considered segmentation errors caused by the algorithm. Structures like the vessels adjacent to the airways, the esophagus and the vena cava are hard to distinguish from the atelectatic lung parenchyma and are not correctly segmented even in the reference images. Thus, it is more convenient to trust the automatic segmentation which at least reproduces systematically the same "errors" instead of relying on a subjective manual segmentation characterized by high inter and intra observer variability.

Similarly, the apparent low performance of the automatic ribs segmentation is due to the bad quality of the segmentation considered as gold standard where the border of the lung in the dorsal region has been poorly segmented. An exact manual-segmentation of the rib-lung edge is not possible in the intercostal space (where the rib is not visible in the CT image), consequently it must be guessed by the expert based on his/her previous anatomical information.

# Chapter 6

# Overview and Conclusions

## 6.1 Overview

Throughout the present thesis, a number of algorithms specially designed for the segmentation of thoracic anatomical structures have been presented concluding with the segmentation of the lungs.

Having observed that the atelectatic lung parenchyma shows very similar gray level and texture in a CT image compared to the tissue of the diaphragm, vessels, fat and heart, anatomical knowledge has been employed to overcome the missing graphical information. The strategy followed to achieve a robust segmentation was inspired by the human psycho-perception of images. Those entities that are easily recognized in a CT slice have been identified first and provided information used for the further segmentation steps of the remaining anatomical structures. This approach has guaranteed a robust and accurate estimation of the lung boundary in the dorsal region by interpolating landmarks derived from the ribs which are univocally recognized independently of the degree of atelectasis. The airways, too, remain unaltered by atelectasis allowing their identification up to the lower end of the bronchial tree. The latter has provided valuable information, together with the ribs cage and a diaphragm model, for the assessment of the completely invisible base of the collapsed lung. With the help of reference landmarks derived from the lung, trachea, vertebrae and the carina, the segmentation of the thoracic aorta,

which CT number differs minimally from the surrounding atelectatic tissue, has been possible. Consequently, inter-pulmonary structures (large airways and aorta) could be excluded from the final lung segmentation.

The results obtained are encouraging considering the difficult task faced by the segmentation algorithms due to the lack of information in CT images of the lungs affected by high degrees of atelectasis. Contrary to the trend of current CAD systems which rely on high definition images for an accurate segmentation, the developed algorithms showed good performance both in 5 mm and 1 mm slice thickness CT images strongly affected by artifacts. By taking advantage of 3D information not available when manual segmentation is performed on a CT slice, the automatic estimation of the lung border in the dorsal region have achieved more accuracy than a qualified operator. However, the deviations observed from the expected lung-diaphragm edge, disqualifies the software for use as a diagnostic tool in the region of the base of the lung.

## 6.2 Original contributions of the dissertation

This thesis is focused on the robust segmentation of the atelectatic lung in 1 mm and 5 mm slice thickness CT images intensily affected by artifacts due to probes, tubes and electrodes. Bearing this in mind, well established segmentation methods have been preferred to more modern approaches of academical interest. Nonetheless, the existing algorithms alone were not able to cope with the large variability observed in the shape of the lung due to different degrees of induced atelectasis and PEEP levels. For that reason, new algorithms have been designed specifically to take advantage of anatomical information previously learned, thus allowing a robust lung segmentation. This has only been possible after a meticulous analysis of the thoracic anatomy that resulted in the identification of those structures which are minimally influenced by inter individual variability and different degrees of atelectasis.

The most important original contributions reported in this this thesis are:

- The identification of the anatomical structures, in the thoracic cavity, that are indicated for the derivation of landmarks and features for the lung segmentation to be based on. Such landmarks and features have the important property of remaining unaltered or quasi invariant among different animals, different degrees of atelectasis, and different PEEP levels, hereby allowing a robust and reliable identification.

- The procedures for segmentation of the ribs, aorta, large airways, upper layer of the diaphragm and lungs by selecting the appropriate algorithms according to the characteristics of the image and the anatomical structure to be processed.

- The combination of pre-segmentation and classification in order to enhance the robustness of the final segmentation algorithm.

- The introduction of classification trees for the classification and identification of anatomical structures, which can be both automatically and manually built. This particularity allows the experienced physician to manually adjust the paramenters of the tree in order for the segmentation algorithms to be applied to species other than those studied in the present work. At the same time, the tedious manual task of pre-segmenting a large training set is not required.

- The development of a robust fit algorithm that excludes outliers in the computation of the fitting function, thus leading to better results, for the specific task it has been designed, than using existing fitting methods.

## 6.3   Future work

As shown in chapter 5, the largest discrepancy between automatic and manual segmentation is due to those inter-pulmonary anatomical structures not considered in the present work. Therefore, the identification of the vena cava and vessels adjacent to the bronchi [26, 32] constitute the main item for the further development of this segmentation tool.

The estimation of the base of the lung is another topic that offers a large potential of improvement. Intra-patient elastic registration is an alternative to consider if a CT of the healthy lung is available in addition to the CT of the injured lung. However, handling the non negligible deformations of the thorax due to the breathing and different PEEP levels, possess a challenge.

Since physicians tend to avoid exposing patiens to the high doses of radiation implicated in a CT study, the analysis of atelectasis by this mean will likely remain as a research resource used mainly with animals. Under such assumption, there are no reasons to avoid higher dose of X-rays involved in thin slice CT, thus implying a reduction of partial volume effects. The same concept could be extended, exposing twice the same animal as required by material decomposition with the hope to obtain a better singal to noise ratio. Hereby, the improved quality of the images should help to enhance the accuracy and robustness of the segmentation algorithms.

It is the hope of the author that this thesis has helped to alleviate the tedious work of manually segmenting the lung from volume CT images. As has been mentioned before, there is still much to be done but the basis of a robust segmentation tool has been identified.

## List of abreviations

Aa.         Arteriae (arterys)

AAM         Active Apearance Model

ARDS        Acute Respiratory Distress Syndrome

$C_{corr}$  Correct segmentation coefficient

$C_{Dice}$  Dice coefficient

$C_{over}$  Over segmentation coefficient

$C_{under}$ Under segmentation coefficient

CAD         Computer Aided Diagnostic

Cf          normalized compactness (shape factor)

Co          compactness (shape factor)

CT          Computer Tomography

DICOM       Digital Imaging and Communications in Medicine

EBP         Elastic Body Spline

ETT         Endotracheal Tube

ERS         Edge-Radius-Symetry transform

FSM         Finite State Machine

HU          Hounfield Unit

LE          Lung Edge

Mm.         Musculi (muscles)

MR          Magnetic Resonance

PCA         Principal Component Analysis

| | |
|---|---|
| PDF | Probability Density Functions |
| PEEP | Positive End-Expiratory Pressure |
| RMSE | Root Mean Squared Error |
| ROI | Region of interest |
| Vv. | Venae (veins) |

# Anhang A

# Algorithms setup

## A.1 Contour Overlap settings for the airways segmentation

**Signature**

$$Ovr = ContourOverlap(Seed, Target, ThreshOvr, Mode)$$

**Parameters**

*Seed*      set of contours used as seed for the volume growing

*Target*      is the set of contours to be analyzed

*ThreshOvr*  minimal number of pixels that must overlap between the areas of the seed and target contour

*Mode*      controls if all overlapped contours (*All*) found in the target set are added to the *Ovr* found by the algorithm, or only one contour is selected, namely the one with lower Y coordinate (*Upper*) or the one with the largest area (*Bigger*)

*Ovr*      set of contours that overlap with *Seed.*

Table A.1 shows the values heuristically assigned to the parameters of the Contour Overlap algorithm according to the current state of the auotmaton (figure 4.4).

| FSM State | ThreshOvr [pixels] | Mode |
|---|---|---|
| Grow trachea down. | 50 | All |
| Grow trachea up. | 1 | All |
| Grow left br. | 10 | All |
| Grow right br. | 10 | All |

Tabelle A.1: Contour Overlap settings according to the FSM state

## A.2   Bronchial Tree Tracking settings

**Signature**

$$(Vol, S) = VolumeGrowing(CTdata, StartIdx, ROI, StrEl, Thres)$$

**Parameters**

*CTdata*   original 3D CT data set. Observe that the filtered CT images are not indicated for the identification of small bronchi with diameter below 1 mm (2 pixels)[1] because the 2D median filter ($7 \times 7$ pixels) would "wash them out".

*StartIdx*   index of the first frame selected to begin with the tracking process. Choosing this slice 45 mm below the carina, assures that the descending bronchi are included in the ROI (see below). This position is not critical and may vary in a range of 1 cm.

*ROI*   region of interes that will be analyzed in the first frame. The lower ROI side employed for the left lung is defined by the left ribs profile (figure 4.19 (a)), and the upper side replicates the lower one shifted 100 pixels in ventral direction. The airways segmented inside this area will be tracked downwards. The same applies for

---

[1]considering the pixel size = 0.5 x 0.5 mm of the CT images used in this study.

the segmentation of the right side of the bronchial tree, using in this case the right ribs profile to delineate the ROI.

*StrEl*  structuting element that dilates the segmented airways used as seed (see 4.6.2), a 8 pixels diameter disk.

*Thres*  threshold defined for the segmentation algorithm. Although the airways have a characteristic CT number below HU, a value of -350 has been set. This relies on the assumption that the gray level of the soft tissue[2] is always higher than -300 HU and the small bronchi that descend oblique show in the CT image gray levels near -400 HU. In consequence, the airways are tracked until their size is as small as one pixel without risk to go on downwards and include the diaphragm tissue in the segmentation.

*Vol*  segmented volume (not required)

*S*  position of the bottom end of the bronchial tree

Since the bronchial tree tracking algorithm searches merely the lowest extreme of the bronchial tree detectable in a CT image, the segmented volume *Vol* is discarded.

## A.3   Stomach segmentation settings

**Signature**

$$(Vol, S) = VolumeGrowing(CTdata, StartIdx, ROI, StrEl, Thres)$$

**Parameters**

*CTdata*  is the filtered 3D CT data set

*StartIdx*  is the index of the last frame selected to begin with the tracking process. This corresponds to the lowest transversal frame where the dark regions of the stomach is detected

---

[2]assuming in 1 mm slice thicknes

116

*ROI*      is the region of interes that will be analyzed in order to segment the seed in the first frame involved in the iterative process. The ROI includes the whole transversal frame above the carina

*StrEl*     is the structuting element, a 20 pixels diameter disk

*Thres*     is the threshold defined for the segmentation algorithm, set to -500 HU

*Vol*       segmented volume of the stomach

*S*         position of the upper extreme of the stomach (discarded)

## A.4   Robust Fit settings for the aorta segmentation

**Signature**

$$X^* = RobustFit(X, Niter, Residual, Model)$$

**Parameters**

*X*          x coordinates vector of the aorta center in each transversal frame before outliers removal and smoothing

*Niter*      maximal number of iterations allowed (set to 15)

*Residual*   mean squared fit error allowed (set to 7 [pixels$^2$ ] )

*Model*      is a general $4^{th}$ polynom used as fitting function

*X\**         x coordinates vector of the aorta center in each transversal frame after outliers removal and smoothing

# Appendix B

# Datasets

The tables below illustrate the weight of the animals involved in the mechanical ventilation studies and the voxel size of the corresponding volume CT data used as training and test set for the segmentation algorithms.

Study 1: "Evaluation of different tidal volumes on the estimation of the PEEP of minimal elastance during Volume Controlled Ventilation (PEEP Titration Protocol)". The data used for the training and test sets corresponds to the sessions performed at end expiration by PEEP levels of 0, 4, 8, 12 and 16 cmH$_2$O.

Study 2: "variable pressure support ventilation vs. conventional pressure support and pressure controlled ventilation". The data employed in the training and test sets correponds to the baseline and injury respectively, under whole drive end expiration sessions.

# B.1 Training set

| Weight [Kg] | Voxel size [mm] | Study |
|:---:|:---:|:---:|
| 25.0 | $0.47 \times 0.47 \times 1$ | 1 |
| 27.0 | $0.47 \times 0.47 \times 1$ | 1 |
| 31.7 | $0.47 \times 0.47 \times 1$ | 1 |
| 44.2 | $0.48 \times 0.48 \times 5$ | 2 |
| 36.0 | $0.51 \times 0.51 \times 5$ | 2 |
| 39.1 | $0.51 \times 0.51 \times 5$ | 2 |
| 39.1 | $0.51 \times 0.51 \times 5$ | 2 |
| 36.5 | $0.51 \times 0.51 \times 5$ | 2 |
| 35.8 | $0.49 \times 0.49 \times 5$ | 2 |
| 33.3 | $0.51 \times 0.51 \times 5$ | 2 |

Table B.1: Weight of the animals and voxel size employed as training set for the automatic segmentation of the lung.

# B.2 Test set

| Weight [Kg] | Voxel size [mm] | Study |
|:---:|:---:|:---:|
| 25.0 | $0.47 \times 0.47 \times 1$ | 1 |
| 27.7 | $0.47 \times 0.47 \times 1$ | 1 |
| 33.7 | $0.53 \times 0.53 \times 1$ | 1 |
| 36.5 | $0.47 \times 0.47 \times 1$ | 1 |
| 44.2 | $0.51 \times 0.51 \times 5$ | 2 |
| 35.6 | $0.45 \times 0.45 \times 5$ | 2 |
| 43.6 | $0.47 \times 0.47 \times 5$ | 2 |
| 42.6 | $0.49 \times 0.49 \times 5$ | 2 |
| 40.1 | $0.49 \times 0.49 \times 5$ | 2 |
| 36.8 | $0.49 \times 0.49 \times 5$ | 2 |

Table B.2: Weight of the animals and voxel size employed as test set for the automatic segmentation of the lung.

# Bibliography

[1] M. Remy-Jardin, J. Remy, D. Artaud, M. Fribourg, and J.P. Beregi. Spiral ct of pulmonary embolism: diagnostic approach, interpretive pitfalls and current indications. *European Radiology*, 8(8):1376–1390, 1998.

[2] Y. Masutani, H. MacMahon, and K. Doi. Computerized detection of pulmonary embolism in spiral ct angiography based on volumetric image analysis. *Medical Imaging, IEEE Transactions on*, 21(12):1517–1523, 2002.

[3] K. Marten, T. Seyfarth, F. Auer, E. Wiener, A. Grillhösl, S. Obenauer, E.J. Rummeny, and C. Engelke. Computer-assisted detection of pulmonary nodules: performance evaluation of an expert knowledge-based detection system in consensus reading with experienced and inexperienced chest radiologists. *European Radiology*, 14(10):1930–1938, 2004.

[4] K. Marten, C. Engelke, T. Seyfarth, A. Grillhösl, S. Obenauer, and EJ Rummeny. Computer-aided detection of pulmonary nodules: influence of nodule characteristics on detection performance. *Clinical Radiology*, 60(2):196–206, 2005.

[5] K. Marten, F. Auer, S. Schmidt, G. Kohl, E.J. Rummeny, and C. Engelke. Inadequacy of manual measurements compared to automated ct volumetry in assessment of treatment response of pulmonary metastases using recist criteria. *European Radiology*, 16(4):781–790, 2006.

120

[6] K. Marten and C. Engelke. Computer-aided detection and automated ct volumetry of pulmonary nodules. *European Radiology*, 17(4):888–901, 2007.

[7] S.G. Armato, F. Li, M.L. Giger, H. MacMahon, S. Sone, and K. Doi. Lung cancer: Performance of automated lung nodule detection applied to cancers missed in a ct screening program. *Radiology*, 225(3):685–692, 2002.

[8] R. Uppaluri, E.A. Hoffman, M. Sonka, G.W. Hunninghake, and G. M c LENNAN. Interstitial lung disease a quantitative study using the adaptive multiple feature method. *American Journal of Respiratory and Critical Care Medicine*, 159(2):519–525, 1999.

[9] J.P. Ko and D.P. Naidich. Computer-aided diagnosis and the evaluation of lung disease. *Journal of Thoracic Imaging*, 19(3):136, 2004.

[10] Y. NAkano, S. Muro, H. Sakai, T. Hirai, K. Chin, M. Tsukino, et al. Computed tomographic measurements of airway dimensions and emphysema in smokers correlation with lung function. *American Journal of Respiratory and Critical Care Medicine*, 162(3):1102–1108, 2000.

[11] O. Weinheimer, T. Achenbach, C. Buschsiewke, CP Heussel, T. Uthmann, and HU Kauczor. Quantification and characterization of pulmonary emphysema in multislice-ct. *Medical Data Analysis (ISMDA 2003, Berlin, Germany)*, pages 77–84, 2003.

[12] J. Zaporozhan, S. Ley, R. Eberhardt, O. Weinheimer, S. Iliyushenko, F. Herth, and H.U. Kauczor. Paired inspiratory/expiratory volumetric thin-slice ct scan for emphysema analysis* comparison of different quantitative evaluations and pulmonary function test. *Chest*, 128(5):3212–3220, 2005.

[13] P. Korfiatis, C. Kalogeropoulou, A. Karahaliou, A. Kazantzi, S. Skiadopoulos, and L. Costaridou. Texture classification-based segmentation of lung affected by interstitial pneumonia in high-resolution ct. *Medical Physics*, 35:5290, 2008.

[14] H. Hong, J. Lee, Y. Yim, and Y.G. Shin. Automatic segmentation and registration of lung surfaces in temporal chest ct scans. *Lecture Notes in Computer Science*, 3523:463–470, 2005.

[15] X. Zhou, T. Hara, H. Fujita, R. Yokoyama, T. Kiryu, H. Hoshi, and M. Kanematsu. Preliminary study for automated recognition of anatomical structure from torso ct images. *Engineering in Medicine and Biology Society, 2005. IEEE-EMBS 2005. 27th Annual International Conference of the*, pages 650–653, 2005.

[16] S. Hu, EA Hoffman, and JM Reinhardt. Automatic lung segmentation for accurate quantitation of volumetricx-ray ct images. *Medical Imaging, IEEE Transactions on*, 20(6):490–498, 2001.

[17] L. Zhang, EA Hoffman, and JM Reinhardt. Atlas-driven lung lobe segmentation in volumetric x-ray ct images. *Medical Imaging, IEEE Transactions on*, 25(1):1–16, 2006.

[18] Q. Li. Recent progress in computer-aided diagnosis of lung nodules on thin-section ct. *Computerized Medical Imaging and Graphics*, 31(4-5):248–257, 2007.

[19] J. Dehmeshki, H. Amin, M. Valdivieso, and X. Ye. Segmentation of pulmonary nodules in thoracic ct scans: A region growing approach. *Medical Imaging, IEEE Transactions on*, 27(4):467–480, 2008.

[20] C. Vinhais and A. Campilho. Lung parenchyma segmentation from ct images based on material decomposition. *Lecture Notes in Computer Science*, 4142:624, 2006.

[21] J. Orban de Xivry, G. Janssens, G. Bosmans, M. De Craene, A. Dekker, J. Buijsen, A. van Baardwijk, D. De Ruysscher, B. Macq, and P. Lambin. Tumour delineation and cumulative dose computation in radiotherapy based on deformable registration of respiratory correlated ct images of lung cancer patients. *Radiotherapy and Oncology*, 85(2):232–238, 2007.

[22] S.G. Armato and W.F. Sensakovic. Automated lung segmentation for thoracic ct impact on computer-aided diagnosis1. *Academic Radiology*, 11(9):1011–1021, 2004.

[23] Y. Lee, T. Hara, H. Fujita, S. Itoh, and T. Ishigaki. Automated detection of pulmonary nodules in helical ct images based on an improved template-matching technique. *Medical Imaging, IEEE Transactions on*, 20(7):595–604, 2001.

[24] D. Wormanns and S. Diederich. Characterization of small pulmonary nodules by ct. *European Radiology*, 14(8):1380–1391, 2004.

[25] RA Blechschmidt, R. Werthschutzky, and U. Lorcher. Automated ct image evaluation of the lung: a morphology-basedconcept. *Medical Imaging, IEEE Transactions on*, 20(5):434–442, 2001.

[26] F. Chabat, X.P. Hu, DM Hansell, and G.Z. Yang. Ers transform for the automated detection of bronchialabnormalities on ct of the lungs. *Medical Imaging, IEEE Transactions on*, 20(9):942–952, 2001.

[27] M.T.T. Uthmarn. Analyse von bronchien in der multislice-ct. *Bildverarbeitung für die Medizin 2004: Algorithmen, Systeme, Anwendungen*, 2004.

[28] D. Mayer, S. Ley, S. Brook, S. Thust, Heussel, and HU Kauczor. 3D-Segmentierung des menschlichen Tracheobronchialbaums aus CT-Bilddaten. page 333, 2003.

[29] D. Mayer, D. Bartz, S. Ley, S. Thust, C.P. Heussel, H.U. Kauczor, and W. Straßer. Segmentation and virtual exploration of tracheobronchial trees. In *International Congress Series*, volume 1256, pages 35–40. Elsevier, 2003.

[30] E. Seneterre, F. Paganin, JM Bruel, FB Michel, and J. Bousquet. Measurement of the internal size of bronchi using high resolution computed tomography (hrct). *European Respiratory Journal*, 7(3):596–600, 1994.

[31] M. Sonka, W. Park, and EA Hoffman. Rule-based detection of intratho-racic airway trees. *Medical Imaging, IEEE Transactions on*, 15(3):314–326, 1996.

[32] MN Prasad and A. Sowmya. Detection of bronchovascular pairs on hrct lung images through relational learning. pages 1135–1138, 2004.

[33] I. Matthews and S. Baker. Active appearance models revisited. *International Journal of Computer Vision*, 60(2):135–164, 2004.

[34] R. Beichel, G. Gotschuli, E. Sorantin, F.W. Leberl, and M. Sonka. Diaphragm dome surface segmentation in ct data sets: a 3d active appearance model approach. *Proceedings of SPIE*, 4684:475, 2002.

[35] MS Brown, MF McNitt-Gray, NJ Mankovich, JG Goldin, J. Hiller, LS Wilson, and DR Aberie. Method for segmenting chest ct image data using an anatomical model: preliminary results. *Medical Imaging, IEEE Transactions on*, 16(6):828–839, 1997.

[36] N. Karssemeijer, L.J.T.O. van Erning, and E.G.J. Eijkman. Recognition of organs in ct-image sequences: a model guided approach. *Computers and Biomedical Research*, 21(5):434–448, 1988.

[37] LS Wilson, MS Brown, H. Talhami, RW Gill, C. Sun, and B. Doust. Medical image understanding using anatomical models: application to chest x-rays. pages 239–250, 1995.

[38] MS BROWN, LS WILSON, BD DOUST, RW GILL, and C. SUN. Knowledge-based method for segmentation and analysis of lung boundaries in chest x-ray images. *Computerized medical imaging and graphics*, 22(6):463–477, 1998.

[39] J.M. Kuhnigk, H. Hahn, M. Hindennach, V. Dicken, S. Krass, and H.O. Peitgen. Lung lobe segmentation by anatomy-guided 3 d watershed transform. 5032:1482–1490, 2003.

[40] M. Sonka, G. Sundaramoorthy, and E.A. Hoffman. Knowledge-based segmentation of intrathoracic airways from multidimensional high resolution ct images. *Medical Imaging*, pages 73–85, 1994.

[41] M. Arnold K. Markstaller. Software zur automatischen quantifizierung von belüftungszuständen bei akuten lungenversagen in dynamischen ct-aufnahmen der lunge. *Fortschr Röntgenstr*, pages 830–835, 2001.

[42] P. Mornet. *Das Schwein und seine Krankheiten*. Schober Verlags-GmbH, 1982.

[43] R. Nickel, J. Frewein, A. Schummer, E. Seiferle, K.H. Wille, and H. Wilkens. *Lehrbuch der Anatomie der Haustiere. Band III: Kreislaufsystem Haut und Hautorgane*. Parey im MVS, 2003.

[44] R. Nickel, A. Schummer, and E. Seiferle. *Lehrbuch der Anatomie der Haustiere. Band II: Eingeweide*. 1960.

[45] Ingo Steinbrück. *Intensivkurs Anatomie*. Elsevier, Urban & Fischer, 2008.

[46] J. Freixenet, X. Munoz, D. Raba, J. Marti, and X. Cufi. Yet another survey on image segmentation: Region and boundary information integration. *Lecture Notes in Computer Science*, pages 408–422, 2002.

[47] DL Phan, C. Xu, and J. Price. A survey of current methods in medical image segmentation. *Annual Review of Biomedical Engineering*, 1998.

[48] A. Schmidt-Richberg, B. Flach, U. Hamburg-Eppendorf, and J. Erhardt. Verfahren zur segmentierung von 4d-ct-bilddaten der lunge. Master's thesis, 2006.

[49] PK Sahoo, S. Soltani, AKC Wong, and YC Chen. A survey of thresholding techniques. *Computer Vision, Graphics, and Image Processing*, 41(2):233–260, 1988.

[50] R.C. Gonzalez and R.E. Woods. *Digital Image Processing*. Prentice Hall, 2007.

[51] WM Morrow, RB Paranjape, RM Rangayyan, and JEL Desautels. Region-based contrast enhancement of mammograms. *Medical Imaging, IEEE Transactions on*, 11(3):392–406, 1992.

[52] W.M. Morrow. Region-based image processing with application to mammography. 1990.

[53] J. Fan, G. Zeng, M. Body, and M.S. Hacid. Seeded region growing: an extensive and comparative study. *Pattern Recognition Letters*, 26(8):1139–1156, 2005.

[54] E.H. Adelson, C.H. Anderson, J.R. Bergen, P.J. Burt, and J.M. Ogden. Pyramid methods in image processing. *RCA Engineer*, 29(6):33–41, 1984.

[55] K. Grauman and T. Darrell. The pyramid match kernel: Discriminative classification with sets of image features. 1(2):3, 2005.

[56] H.Y. Kim and S.A. de Araujo. Grayscale template-matching invariant to rotation, scale, translation, brightness and contrast. *Lecture Notes in Computer Science*, 4872:100, 2007.

[57] G.D. Tourassi, R. Vargas-Voracek, D.M. Catarious Jr, and C.E. Floyd Jr. Computer-assisted detection of mammographic masses: A template matching scheme based on mutual information. *Medical Physics*, 30:2123, 2003.

[58] JF Verhey, A. Ludwig, J. Rexilius, S.K. Warfield, C. Mamisch, R. Kikinis, C.F. Westin, R. Seibel, and O. Rienhoff. Mulitmodale nichtrigide registrierung von ultraschall und mr bilddaten unter verwendung eines biomechanischen modells. *Bildverarbeitung für die Medizin 2002– Algorithmen Systeme Anwendungen*, pages 310–313.

[59] H. Delingette. Toward realistic soft-tissue modeling in medical simulation. *Proceedings of the IEEE*, 86(3):512–523, 1998.

[60] Ramon Q. Erkamp. *Nonlinear Elasticity Imaging Using Ultrasound*. PhD thesis, University of Michigan, 2003.

126

[61] P.F. Villard, W. Bourne, and F. Bello. Modelling organ deformation using mass-springs and tensional integrity. *Lecture Notes in Computer Science*, 5104:221–226, 2008.

[62] A.L. Didier, P.F. Villard, J.Y. Bayle, M. Beuve, B. Shariat, H.L. Pradel, and F. Lyon. Breathing thorax simulation based on pleura physiology and rib kinematics. pages 35–42, 2007.

[63] A. Hostettler, S.A. Nicolau, L. Soler, Y. Remond, and J. Marescaux. A real-time predictive simulation of abdominal organ positions induced by free breathing. *Lecture Notes in Computer Science*, 5104:89–97, 2008.

[64] LA Platenik, MI Miga, DW Roberts, KE Lunn, FE Kennedy, A. Hartov, and KD Paulsen. In vivo quantification of retraction deformation modeling for updated image-guidance during neurosurgery. *Biomedical Engineering, IEEE Transactions on*, 49(8):823–835, 2002.

[65] J.M. Schwartz, M. Denninger, D. Rancourt, C. Moisan, and D. Laurendeau. Modelling liver tissue properties using a non-linear visco-elastic model for surgery simulation. *Medical Image Analysis*, 9(2):103–112, 2005.

[66] M.M. Coselmon, J.M. Balter, D.L. McShan, and M.L. Kessler. Mutual information based ct registration of the lung at exhale and inhale breathing states using thin-plate splines. *Medical Physics*, 31:2942, 2004.

[67] J. Kohlrausch, K. Rohr, and S. Stiehl. A new class of elastic body splines for nonrigid registration of medical images. 2001.

[68] P.F. Villard, M. Beuve, B. Shariat, V. Baudet, and F. Jaillet. Lung mesh generation to simulate breathing motion with a finite element method. pages 194–199, 2004.

[69] JA Schnabel, C. Tanner, AD Castellano-Smith, A. Degenhard, MO Leach, DR Hose, DLG Hill, and DJ Hawkes. Validation of nonrigid

image registration using finite-element methods: application to breast mr images. *Medical Imaging, IEEE Transactions on*, 22(2):238–247, 2003.

[70] D.S. Meier and E. Fisher. Atlas-based anatomic labeling in neurode-generative disease via structure-driven atlas warping. *Journal of Neuroimaging*, 15(1):16–26, 2005.

[71] MB Cuadra, C. Pollo, A. Bardera, O. Cuisenaire, J.G. Villemure, and J.P. Thiran. Atlas-based segmentation of pathological mr brain images using a model of lesion growth. *Medical Imaging, IEEE Transactions on*, 23(10):1301–1314, 2004.

[72] W.L. Nowinski and D. Belov. Toward atlas-assisted automatic interpretation of mri morphological brain scans in the presence of tumor1. *Academic Radiology*, 12(8):1049–1057, 2005.

[73] M. Lorenzo-Valdes, G.I. Sanchez-Ortiz, R. Mohiaddin, and D. Rueckert. Atlas-based segmentation and tracking of 3d cardiac mr images using non-rigid registration. *Lecture Notes in Computer Science*, pages 642–650, 2002.

[74] R.M. Rangayyan, N.R. Mudigonda, and J.E.L. Desautels. Boundary modelling and shape analysis methods for classification of mammographic masses. *Medical and Biological Engineering and Computing*, 38(5):487–496, 2000.

[75] M. Styner, G. Gerig, J. Lieberman, D. Jones, and D. Weinberger. Statistical shape analysis of neuroanatomical structures based on medial models. *Medical Image Analysis*, 7(3):207–220, 2003.

[76] H. Freeman. On the encoding of arbitrary geometric configurations. *IRE Trans. Electron. Comput*, 10(2):260–268, 1961.

[77] R.M. Rangayyan. *Biomedical Image Analysis*. CRC Press, 2005.

[78] L. Shen, RM Rangayyan, and JEL Desautels. Application of shape analysis to mammographic calcifications. *Medical Imaging, IEEE Transactions on*, 13(2):263–274, 1994.

[79] K. Kim, J. Kim, and B. Min. Classification of malignant and benign tumors using boundary characteristics in breast ultrasonograms. *Journal of Digital Imaging*, 15:224–227, 2002.

[80] L. Gupta and MD Srinath. Contour sequence moments for the classification of closed planar shapes. *Pattern Recognition*, 20(3):267–272, 1987.

[81] D. Lu and Q. Weng. A survey of image classification methods and techniques for improving classification performance. *International Journal of Remote Sensing*, 28(5):823–870, 2007.

[82] L. Breiman. *Classification and Regression Trees*. Chapman & Hall/CRC, 1998. xxx.

[83] S.C. Lemon, J. Roy, M.A. Clark, P.D. Friedmann, and W. Rakowski. Classification and regression tree analysis in public health: Methodological review and comparison with logistic regression. *Annals of Behavioral Medicine*, 26(3):172–181, 2003.

[84] R.J. Marshall. The use of classification and regression trees in clinical epidemiology. *Journal of Clinical Epidemiology*, 54(6):603–609, 2001.

[85] JA Falconer, BJ Naughton, DD Dunlop, EJ Roth, DC Strasser, and JM Sinacore. Predicting stroke inpatient rehabilitation outcome using a classification tree approach. *Arch Phys Med Rehabil*, 75(6):619–25, 1994.

[86] B.D. Ripley. *Pattern Recognition and Neural Networks*. Cambridge University Press, 1996.

[87] S.F. Chen. Compiling large-context phonetic decision trees into finite-state transducers. 2003.

[88] H.J. Steadman, E. Silver, J. Monahan, P. Appelbaum, P.C. Robbins, E.P. Mulvey, T. Grisso, L.H. Roth, and S. Banks. A classification tree approach to the development of actuarial violence risk assessment tools. *Law and Human Behavior*, 24(1):83–100, 2000.

[89] G. De'ath and K.E. Fabricius. Classification and regression trees: A powerful yet simple technique for ecological data analysis. *Ecology*, 81(11):3178–3192, 2000.

[90] K. Grill-Spector and N. Kanwisher. As soon as you know it is there, you know what it is. *Psychological Science*, 16(2):152–160, 2005.

[91] J.K. Leader, B. Zheng, R.M. Rogers, F.C. Sciurba, A. Perez, B.E. Chapman, S. Patel, C.R. Fuhrman, and D. Gur. Automated lung segmentation in x-ray computed tomography development and evaluation of a heuristic threshold-based scheme1. *Academic Radiology*, 10(11):1224–1236, 2003.

[92] Wladimir Peckar. *Application of Variational Mathods to Elastic Registration of Medical Images*. Logos-Verlag, 1998.

[93] M. Chen, T. Kanade, D. Pomerleau, and J. Schneider. 3-d deformable registration of medical images using a statistical atlas. *Lecture Notes in Computer Science*, pages 621–630, 1999.

[94] MH Davis, A. Khotanzad, DP Flamig, and SE Harms. A physics-based coordinate transformation for 3-d image matching. *Medical Imaging, IEEE Transactions on*, 16(3):317–328, 1997.

[95] J. Kybic. *Elastic Image Registration using Parametric Deformation Models*. 2001.

[96] R. Szeliski and S. Lavalle. Matching 3-d anatomical surfaces with non-rigid deformations using octree-splines. *International Journal of Computer Vision*, 18(2):171–186, 1996.

[97] S. Gouttard, M. Styner, S. Joshi, R.G. Smith, H.C. Hazlett, and G. Gerig. Subcortical structure segmentation using probabilistic atlas priors. 6512:65122J, 2007.

[98] Falk Uhleman. *Wahrscheinlichkeitsbasiertes Modell zur verknüpften Segmentierungs- und elastischen Deformationsanalyse in der medizinischer Bildverarbeitung.* TUDpress, 2006.

[99] J.E. Hopcroft, R. Motwani, and J.D. Ullman. Introduction to automata theory, languages and computability. 2000.

[100] C. De Boor. A practical guide to splines. 2001.

[101] YJ Zhang. A survey on evaluation methods for image segmentation. *Pattern Recognition*, 29(8):1335–1346, 1996.

[102] J.S. Cardoso and L. Corte-Real. Toward a generic evaluation of image segmentation. *IEEE Transactions on Image Processing*, 14(11):1773–1782, 2005.

[103] N.R. Pal and S.K. Pal. A review on image segmentation techniques. *Pattern Recognition*, 26(9):1277–1294, 1993.

[104] J.S. Weszka and A. Rosenfeld. Threshold evaluation techniques. *Systems, Man and Cybernetics, IEEE Transactions on*, 8(8):622–629, 1978.

[105] MD Levine and AM Nazif. Dynamic measurement of computer generated image segmentations. *IEEE transactions on pattern analysis and machine intelligence*, 7(2):155–164, 1985.

[106] MD Levine and AM Nazif. An experimental rule-based system for testing low level segmentation strategies. multicomputers and image processing algorithms and programs. *Academic Press*, 149:160, 1982.

[107] T. Lei and W. Sewchand. Statistical approach to x-ray ct imaging and its applications inimage analysis. ii. a new stochastic model-based im-

age segmentationtechnique for x-ray ct image. *Medical Imaging, IEEE Transactions on*, 11(1):62–69, 1992.

[108] DL Collins, AP Zijdenbos, V. Kollokian, JG Sled, NJ Kabani, CJ Holmes, and AC Evans. Design and construction of a realistic digital brain phantom. *Medical Imaging, IEEE Transactions on*, 17(3):463–468, 1998.

[109] CJ Van Rijsbergen. *Information Retrieval*. Butterworth-Heinemann Newton, MA, USA, 1979.